Mon. Not. R. Astron. Soc. **262,** 545–587 (1993)

The distribution of low-mass stars in the Galactic disc

Pavel Kroupa,[1] Christopher A. Tout[2] and Gerard Gilmore[2]
[1] *Astronomisches Rechen-Institut, Mönchhofstraße 12-14, D-6900 Heidelberg, Germany*
[2] *Institute of Astronomy, Madingley Road, Cambridge CB3 0HA*

Accepted 1992 October 27. Received 1992 July 6; in original form 1992 March 11

ABSTRACT

We quantify the complex interdependence of stellar binarity, the stellar mass–luminosity relation, the mass function, the colour–magnitude relation and Galactic disc structure, all of which must be understood when analysing star-count data and stellar luminosity functions. We derive a mass–M_V relation and a model for the change of stellar luminosity with changes in chemical abundance and age. Combination of this with detailed modelling of all astrophysical and observational contributions to the Malmquist scatter allows us to model star-count data without approximating Malmquist corrections. We show for the first time that a single mass function and normalization explain the stellar distribution towards both Galactic poles, as well as the distribution of stars within a distance of 5.2 pc of the Sun. The initial mass function can be approximated by $\xi(m) \propto m^{-\alpha}$ with $\alpha_3 \approx 2.7$ for stars more massive than 1 $M_\odot$, $\alpha_2 \approx 2.2$ in the mass range $0.5 \leq m \leq 1$ $M_\odot$ and $0.70 < \alpha_1 < 1.85$ in the range $0.08 < m \leq 0.5$ $M_\odot$. If the stars at a distance of about 100 pc from the Galactic mid-plane have a metallicity smaller by about 0.1 dex than do the stars near the plane used to calibrate the mass–M_V and colour–magnitude relations, then both the stars within 5.2 pc of the Sun and the star-count data reaching to a photometric distance of 130 pc lead to a low-mass power-law index of $\alpha_1 \approx 1.5$. The change in the power index at 0.5 $M_\odot$ may indicate a characteristic mass-scale in the star formation process. Our model is most consistent with the data if the proportion of binaries among 'stars' is larger than 50 per cent and if the component masses are uncorrelated. The possible decline of the proportion of binaries with increasing absolute magnitude, observed in the solar neighbourhood, is in agreement with our models. Two features in the luminosity function for low-mass stars are universal, being solely the result of stellar physics. These features are a flattening at $M_V \approx 7$ and a conspicuous maximum at $M_V \approx 12$. Binary stars cause the system luminosity function derived from photographic surveys to decrease uniformly with increasing magnitude relative to the single-star luminosity function, but both show the same general features. The solar neighbourhood mass density in main-sequence stars with masses between 0.08 and 100 $M_\odot$ is $\rho = 0.05 \pm 0.01$ $M_\odot$ pc^{-3}, of which main-sequence stars less massive than the Sun contribute about 80 per cent. These estimates explicitly include the effects of binaries. Unresolved binaries cause the apparent disc scaleheight to decrease with decreasing mass to a value of ≈ 150 pc for star-count data in the colour range $4 < V-I < 4.5$ if all 'stars' are unresolved binaries with uncorrelated component masses. The vertical structure of the Galactic disc is not well described by a single exponential within a few hundred pc of the plane. Neglect of this can lead to a spurious apparent correlation between stellar mass and disc scaleheight.

Key words: methods: data analysis – binaries: general – stars: evolution – Hertzsprung–Russell (HR) diagram – stars: luminosity function, mass function – Galaxy: stellar content.

1 INTRODUCTION

The mass and luminosity functions for stars impose important constraints on star formation theories. Conversion of the single-star luminosity function to a mass function via the mass–luminosity relation tells us how many stars form in a given mass interval and how much mass is stored in stars. By comparing the system luminosity function with the single-star luminosity function, we obtain information on how stellar systems are distributed and thus how important binary stars are in the stellar formation mechanism. Comparison of the Galactic field luminosity functions with those in young open clusters sheds light on how the star formation mechanism depends upon environment.

The number of stars per unit magnitude interval in the Galactic field within a distance of 20 pc, the 'nearby luminosity function', rises steeply in the absolute visual magnitude range $M_V = 0$–5, after which it flattens to a weak local minimum at $M_V \approx 7$ (sometimes referred to as the 'Wielen dip') and then continues to rise to $M_V \approx 12$ (Wielen, Jahreiss & Krüger 1983, hereafter WJK). This nearby luminosity function is the best determination of the single-star luminosity function for stars brighter than $M_V \approx 12$ because most binary star components have been identified. Those systems not resolved will consist mostly of a primary brighter than $M_V \approx 12$ and a secondary much fainter than the primary, so that the luminosity function determined within a distance of 20 pc for stars brighter than $M_V \approx 12$ can be assumed to be a complete census of such stars.

At fainter magnitudes, the behaviour of the luminosity function becomes very uncertain because the data of WJK provide lower limits only. The number counts within 5.2 pc of the Sun and northwards of declination $-20°$, where the data are probably complete to within $M_V \approx 17$ (Dahn, Liebert & Harrington 1986, hereafter DLH; Henry & McCarthy 1990), barely improve the situation because of the small numbers. They are, however, consistent with a flat luminosity function.

Better statistics at the faint end are obtained by two-colour photographic surveys which reach to photometric distances of about 100 pc (Reid & Gilmore 1982; Hawkins & Bessell 1988; Stobie, Ishida & Peacock 1989, hereafter SIP). These surveys, usually in the directions of the North or South Galactic Poles, use the method of photometric parallax to determine distances and lead to luminosity functions which, although in agreement with each other, differ significantly from the nearby luminosity function at magnitudes fainter than $M_V \approx 13$, beyond which they fall off rapidly (DLH). It is possible to explain the difference as a result of binary stars if the component masses are uncorrelated (Kroupa, Tout & Gilmore 1991, hereafter KTG2). Most binaries will not be detected on photographic plates with a resolution of 2 to 3 arcsec, and, even if wide enough to be resolved, faint companions to brighter primaries will be missed at large distances because the distance limits in these surveys decrease rapidly with increasing absolute magnitude of the stars.

In what follows, we shall refer to the luminosity function determined by counting the stars within the immediate solar neighbourhood as the single-star luminosity function, and to the luminosity function derived from photographic surveys as the system luminosity function.

The results of Kroupa, Tout & Gilmore (1990, hereafter KTG1) can be used as the first step in an iterative process. Neglecting unresolved binaries, we derived mass–M_V relations for stars less massive than the Sun. These relations have structure not previously appreciated, and lead to the features seen in the luminosity function determined from the stars within a distance of 20 pc (the dip at $M_V \approx 7$) and in the photographically determined luminosity functions (the peak at $M_V \approx 12$). The work of KTG2 can be considered as the next step, in which we applied a mass–luminosity relation derived in KTG1 to the problem of a comparison of the shapes of the single-star and system luminosity functions. We assumed that stellar masses in a binary system with both components less massive than the Sun are uncorrelated and drawn from the same mass function. The resultant mass function differs significantly from the mass functions found in KTG1. However, we noted a possible normalization discrepancy. The system luminosity function we used was corrected by SIP for a Galactic disc scaleheight of 325 pc, but the normalization of the mass function in the Galactic mid-plane derived from this luminosity function did not agree with the normalization derived from the single-star luminosity function. This discrepancy suggested either that the local number density of faint stars differs from that in the general Galactic field, or that the model KTG2 implemented was not detailed enough in that the effects of cosmic scatter were not modelled, or perhaps that the Galactic disc scaleheight is not 325 pc.

In reply to our study, Reid (1991) considered the same problem. He showed that the photographically determined luminosity functions cannot be reconciled with a model based on the observed luminosity function of single stars and on the observed properties of binary systems within a distance of 10 pc. Reid also took into account Gaussian scatter about the colour–magnitude relation as a model of cosmic scatter.

Given the contradiction between our results and those of Reid (1991), and the problem of the normalization we found, we investigate in the present analysis the stellar distribution in the nearby Galactic disc in much greater detail. Our aim is to constrain, from the data, the mass-function power-law index, the disc scaleheight and the binary fraction among 'stars' (i.e. apparently single stars). We show that statistically significant solutions to both the nearby and photographic star-count data can be found that reproduce the behaviour of both the nearby and photographically determined luminosity functions, as well as the number density of stars with distance from the Galactic mid-plane.

We derive the mass–luminosity relation in Section 2. In Section 3 we develop a model of the age, chemical and binary system distribution in the Galactic disc and show that it leads to a cosmic scatter similar to the observed value. We are then able to model the Malmquist effects and to compare our models with raw data discussed in Section 4. We describe our simulations in Section 5 and in Section 6 we introduce the statistical tests we choose. In Section 7 we study the sensitivity of the solutions for the disc scaleheight and mass-function power-law index to the colour–magnitude relation and to the proportion of unresolved binaries among 'stars'. In Section 8 we deduce a mass function and its overall normalization, which yields the observed stellar densities in the immediate solar neighbourhood and out to a photometric

distance of 130 pc from the Galactic plane. Alternative models are discussed in Section 9. In Section 10 we study the behaviour of the apparent disc scaleheight as a function of spectral type of the tracer population. Our conclusions are presented in Section 11.

2 THE MASS–LUMINOSITY RELATION

In Fig. 1 we show the empirical nearby luminosity function as a histogram obtained by WJK and extended to $M_V \geq 13$ in Section 4. At magnitudes fainter than $M_V \approx 12$, the uncertainties are very large indeed. However, we note the following details. In the interval $M_V = 6$–8 the luminosity function flattens and achieves a local minimum at $M_V \approx 7$. This can be understood in terms of a change in slope in the mass–M_V relation caused by H^- opacity in the outer layers of stars. KTG1 discuss this, and another much more pronounced inflexion in the mass–M_V relation at $M_V \approx 12$, in greater detail. Diatomic hydrogen molecules associate at stellar masses smaller than about 0.5 $M_\odot$, which affects the

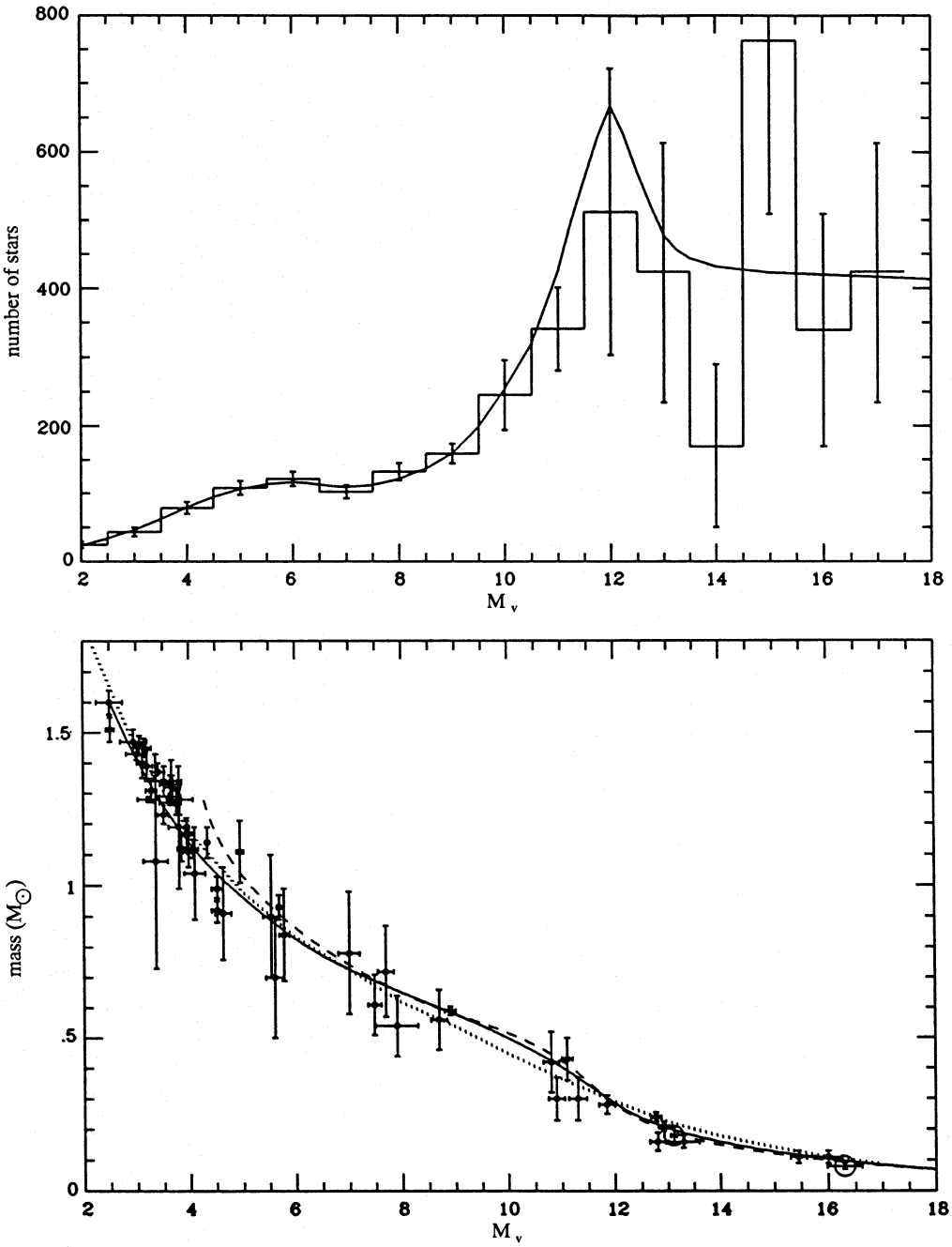

Figure 1. In the upper panel, the observed local luminosity function based on data compiled by Wielen et al. (1983) and extended to $M_V \geq 13$ in Section 4.2 is shown as a histogram. The solid curve depicts our adopted single-star luminosity function. Units are number of stars in a sphere with radius 20 pc. In the lower panel we show the mass–M_V relation for stars (solid curve) derived in Section 2. The dashed curve represents the mass–M_V relation used in KTG2 and derived by KTG1, and the dotted curve the one used by Scalo (1986). Filled circles are the observational data compiled by Popper (1980) and used in Section 2 to constrain the mass–M_V relation. Ross 614 A and B (Liebert & Probst 1987) are shown by open circles.

equation of state of the outer stellar envelope. Also, stars less massive than about 0.3 $M_\odot$ are fully convective. These two effects combine to cause distinct non-linear behaviour in the mass–bolometric-luminosity relation at a mass $m \approx 0.3\ M_\odot$. Theoretical stellar models are in acceptable agreement with observational mass–M_V data, but are not sufficiently refined to allow more quantitative statements on the above effects. However, as pointed out by KTG1, they may be used to identify the relevant physics.

As in KTG1 and KTG2, we continue to use the V band in our study. We do not work with bolometric luminosities because the bolometric corrections are very uncertain for low-mass stars. There are two reasons why we do not work in the near-infrared bands where most of the flux appears for low-mass stars. First, there is no compilation of mass–luminosity data in the near-infrared bands that is superior to that of Popper (1980). Secondly, it does not matter that the flux in the V band is a small proportion of the bolometric flux for M stars, as long as the parameter we choose to characterize the stellar luminosity is a monotonically changing function of stellar mass. Differential line blanketing effects are severe in the V band, so that the mass–M_V relation is expected to show some features associated with the formation and excitation of TiO, H_2O and other molecules in the atmospheres of late-type dwarfs. These molecules lead to a gradual effect with temperature, as opposed to the change in the structure of a star that occurs rapidly due to the simple and very abundant hydrogen. In the magnitude range $5 < M_V < 13$, the mass–M_V relation is mostly affected by the formation of H^- and H_2. In addition, at $M_V \approx 12$ the onset of full convection plays a very significant role. At fainter magnitudes, where line blanketing owing to other molecules becomes severe, $|dm/dM_V|$ is very small so that changes in M_V due to these molecules do not affect the mass estimation significantly. We note that use of the I band instead of the V band does not alleviate this problem with line blanketing. As an example, we refer to fig. A1 of Gilmore, Reid & Hewett (1985), where the I-band spectrum of VB10 is shown. It is not possible to define a continuum. We shall return to the effects of line blanketing and metallicity abundance in Section 3.2.

Before we turn our attention to the mass–M_V relation we need to specify a stellar mass function, for reasons that will become apparent shortly. KTG2 found model luminosity functions consistent with both the single-star and the system luminosity functions using a two-component power-law mass function $\xi(m)$ for masses below 1 $M_\odot$. Above this mass, the mass function derived by Scalo (1986) is well approximated by a third power-law segment, and here we adopt the following three-component power-law mass function:

$$\xi(m) = n \begin{cases} (m/m_0)^{-\alpha_1} & \text{if } m_l \le m < m_0, \\ (m/m_0)^{-\alpha_2} & \text{if } m_0 \le m < m_1, \\ (m_1/m_0)^{-\alpha_2}(m/m_1)^{-\alpha_3} & \text{if } m_1 \le m < \infty, \end{cases} \qquad (1)$$

where m is the stellar mass in solar units and $\xi(m)\,dm$ is the number of stars in the mass interval m to $m+dm$. We extend our mass function to higher masses than in KTG2, because we need to derive a mass–M_V relation which has the correct slope around 1 $M_\odot$.

We now apply the 'inverse method' of KTG1 to find a mass–M_V relation which minimizes χ^2 with respect to empirical mass–M_V data collated by Popper (1980). This method consists of adopting a luminosity function and varying the parameters which specify the stellar mass function until the resulting mass–M_V relation is an acceptable fit to the data. Here we adopt the luminosity function shown in Fig. 1 as the smooth curve. This curve is well constrained in the magnitude range $M_V = 0$ to ≈ 10 and, in the light of the results obtained by KTG1 and KTG2, we know it to have a peak at $M_V \approx 12$. We assume the particular form of this peak shown in Fig. 1 and later confirm the consistency of this assumption. We implement equations (2) and (3) of KTG1 with the two boundary conditions $M_V = 4.75$ when $m = 1.0\ M_\odot$, approximately representing a 5×10^9 yr old solar model, and $M_V = 18$ when $m = m_l$. The minimum-χ^2 solutions for two M_V intervals are listed in Table 1, where k is the number of data points in the listed M_V interval. The uncertainties in the parameters are estimated by changing each in turn from the minimum solution until the change in χ^2 assumes the 95 per cent confidence value $\Delta\chi^2 = 4.0$

It is of interest to note that KTG2 also found $m_0 = 0.5\ M_\odot$ to be the best solution, using a different approach. As already shown by KTG1, a single-power-law mass function is not a solution to the entire mass range between 1 and 0.08 $M_\odot$. The mass function must flatten somewhere between 0.4 and 0.5 $M_\odot$. This structure may be a signature of the star formation process.

Our adoption of the luminosity function shown as a solid curve in Fig. 1 constrains α_2 through both the very accurate WJK luminosity function and Popper's data in the magnitude range $5 < M_V < 10$. We are thus quite confident that $\alpha_2 = 2.2$, and it is not surprising that this value agrees well with the power-law index found by Salpeter (1955). On the other hand, the value of α_1 appears less well founded. It rests upon the assumption that our adopted luminosity function has the form shown in Fig. 1 for $M_V > 10$. In this paper we test for α_1 by requiring it to be a solution to both the photographically determined distribution of stars in (colour, distance) space and the (sparse) data on stars within 5.2 pc. We must be careful in accepting $\alpha_3 = 4.5$, which represents the present-day mass function. The initial mass function at masses $> 1\ M_\odot$ derived by Scalo (1986) is corrected for stellar evolution and can be approximated with $\alpha_3 \approx 2.7$ (see Fig. 22). At smaller masses, evolutionary effects are small and the present-day mass function is a good approximation to the initial mass function.

The mass–M_V relation is shown in Fig. 1, where we compare it to the mass–M_V relation used by KTG2 and by Scalo (1986). The points of inflexion at $M_V \approx 8$ (a maximum in dm/dM_V) and particularly, in our relation, at $M_V \approx 12$ (a minimum in dm/dM_V) should be noted. They are clearly visible in Fig. 2, where we show the slope of the mass–M_V relations of Fig. 1. The displayed curves are also the luminosity functions for a mass function $\xi(m) = 1$. The deviation at $m > 1\ M_\odot$ between the relation derived in this section and that derived in KTG1 is due to our extension to higher masses in this work and our somewhat different boundary condition at 1.0 $M_\odot$. At $M_V > 6$ our relation is very similar to the one used by KTG2. It had been derived by KTG1 without taking into account the effects of unresolved binary stars. We tabulate the mass–M_V relation in Appendix

Table 1. The minimum-χ^2 solution.

χ^2	k	M_V	α_1	α_2	α_3	m_1	m_0	m_1
18.3	23	5–16	$1.2^{+0.09}_{-0.07}$	$2.2^{+0.23}_{-0.26}$	—	$0.07^{+0.006}_{-0.008}$	$0.5^{+0.06}_{-0.05}$	—
187	63	2.6–16			$4.5^{+0.07}_{-0.15}$			$1.0^{+0.006}_{-0.007}$

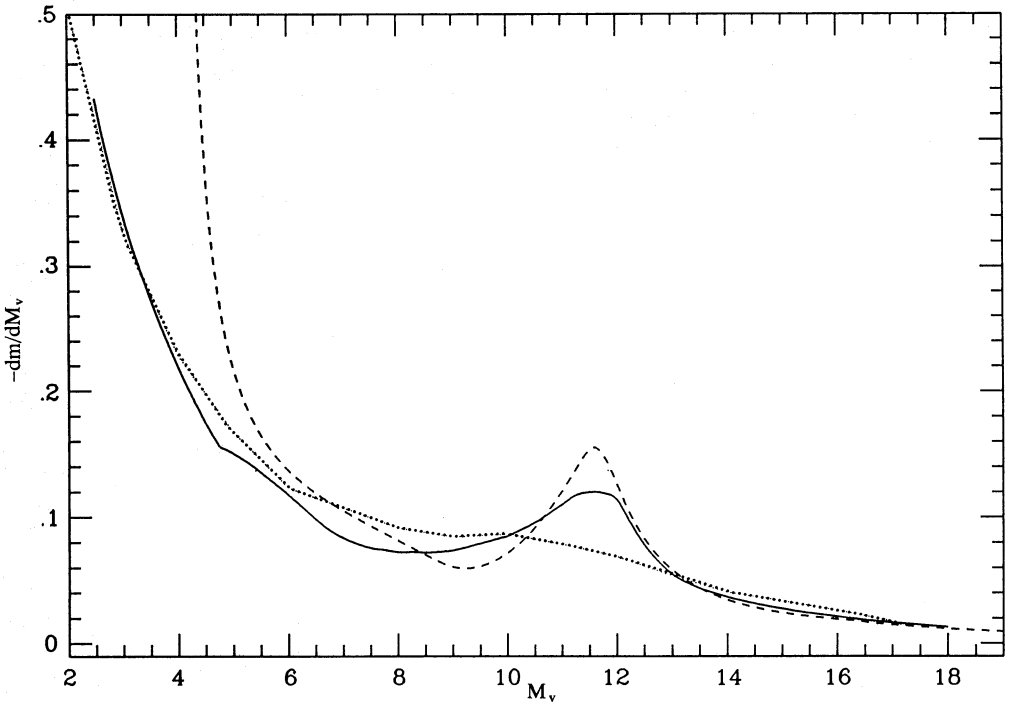

Figure 2. The absolute value of the slope, dm/dM_V, of the mass–M_V relations shown in Fig. 1.

A. Current models show that hydrogen burning stops around 0.08 $M_\odot$ (see, for example, Liebert & Probst 1987). This corresponds to $M_V = 17.3$ from our mass–M_V relation. It is, however, worth remembering that four apparently normal stars with $M_V > 18$ are known (Monet et al. 1992), and that the lower limit for hydrogen-burning stars remains uncertain. The sparse mass–M_V data cause concern that the true mass–M_V relation may have a different slope for $M_V > 14$ than that of our mass–M_V relation. In a later paper, different mass–M_V relations will be investigated using the methods developed here. As we show in the following section, the contributions to cosmic scatter that we model lead quite naturally to the presence of stars with $M_V > 17.3$.

3 COSMIC SCATTER

Photographic surveys used for the determination of stellar space densities rely on an absolute-magnitude–colour relation to derive the absolute magnitude of a star of a certain colour, and hence its distance. Stars used to define such a relation are usually well-studied standards with trigonometric parallax known to within 10 per cent. Nevertheless, from plotting the absolute magnitudes against colour we find that such a sample of stars shows an appreciable scatter in absolute magnitude. SIP determine this scatter to be $\sigma(M_V) = 0.51$ mag. They also show that a magnitude-limited sample of stars suffers not only from the classic Malmquist bias – a magnitude-limited sample appears brighter than the volume-limited sample it is supposed to represent – but also from an apparent increase in number density. Both of these effects arise because more of the intrinsically brighter stars are scattered into the sampling space than intrinsically fainter stars are scattered outward, since the number of stars increases with the square of the distance. If we are to study the number and mass density of low-mass stars in the Galactic disc, we need an understanding of cosmic scatter.

The luminosity of a star of mass m depends on its age and metallicity. We assume that variable mass loss, rotation and magnetic fields have only small effects which, in any case, would be hard to quantify. The absolute luminosity of a star also depends on the measured trigonometric distance and whether there are any unresolved companions which contribute to the light.

In this section we isolate all effects which lead to a displacement of a star from the empirical colour–magnitude relation. We develop models describing stellar evolution, chemical abundance variation, trigonometric parallax errors and binarity. Finally, we combine these effects into a model of cosmic scatter and compare this model with observations. We can then correct the empirical colour–magnitude relation for systematic effects.

3.1 Age

Both pre-main-sequence stars and those evolving across the main sequence are brighter than their zero-age luminosity. We quantify both these effects by using simple empirical expressions for $\delta M_{V,\mathrm{age}}$, the increase in absolute visual magnitude above the adopted mass–M_V relation. In the first 10^7 yr, evolution is rapid and uncertain and such stars are unlikely to enter our sample because they will appear as protostellar objects, probably in star-forming regions. We assume a constant star formation rate and generate an age, t, for a star of mass m from a uniform distribution between 10^7 yr and 1.2×10^{10} yr (which is approximately the age of the Galactic disc). If t is smaller than the time, t_0, at which the star reaches the main sequence, then we evolve it along a pre-main-sequence track. Otherwise, we evolve it across the main sequence.

3.1.1 *Pre-main-sequence evolution*

Using the stellar evolution code of Eggleton (1971, 1972), we have constructed pre-main-sequence models of 0.1, 0.15, 0.2, 0.25, 0.3 and 0.4 $M_\odot$, beginning with a highly inflated star of about 60 $R_\odot$. Initial contraction and deuterium burning are very rapid, and by 10^7 yr the star will have joined the same Hayashi track whatever the formation mechanism in the early stages. Beyond this, the evolution in bolometric luminosity of a low-mass star is well represented by an exponential law as shown in Fig. 3. Fitting from the above masses and assuming the same evolution in the V band, we find

$$\delta M_{V,\mathrm{age}} = -2.5(\alpha \log_{10} t + \beta), \qquad (2)$$

where α and β are functions of mass, and age t is measured in years:

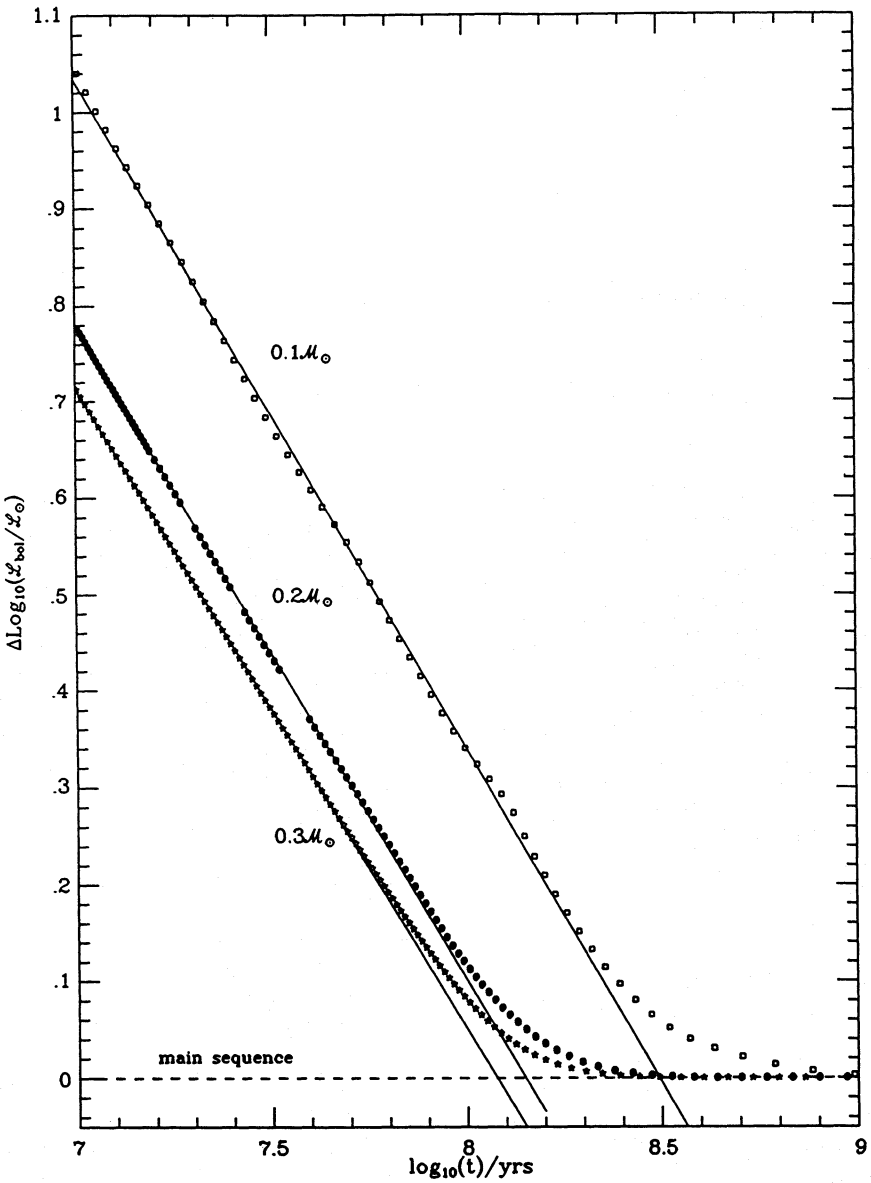

Figure 3. The evolution of the bolometric luminosity of a 0.1-, 0.2- and 0.3-$M_\odot$ star. The exponential fits (equation 2) are shown as straight lines (see Section 3.1.1).

$$\alpha = 0.1338\,m - 0.7045$$

and

$$\beta = 4.823\,m^{-0.0848}.$$

The star arrives on the main sequence at age t_0, which is given approximately by

$$\log_{10} t_0 = \begin{cases} -5.380m + 9.0322 & \text{if } m \le 0.15\ \mathrm{M}_\odot, \\ -0.9398m + 8.3543 & \text{if } m > 0.15\ \mathrm{M}_\odot. \end{cases} \quad (3)$$

Our assumption that the evolution in the V band is similar to that of bolometric luminosity is an oversimplification, as it assumes that stars less massive than 0.5 $\mathrm{M}_\odot$ follow vertical paths in the Hertzsprung–Russell (HR) diagram as they contract on to the main sequence. Pre-main-sequence evolution for higher mass stars is not important for our purpose, because $t_0 < 8 \times 10^7$ yr, which is much less than the age of the Galactic disc ($\approx 10^{10}$ yr), so that the chance of observing a pre-main-sequence star with $m > 0.5\ \mathrm{M}_\odot$ is very small. Effects of discs and stellar rotation on the luminosities of pre-main-sequence stars can be very large, and we need to bear this in mind when intepreting any results based on pre-main-sequence computations. However, such effects are likely to be most important for ages of less than about 10^7 yr.

3.1.2 *Evolution on the main sequence*

The evolution on the main sequence can again be represented by simple analytic formulae (Eggleton, Fitchett & Tout 1989) fitted to models evolved with Eggleton's code:

$$\delta M_{V,\mathrm{age}} = -2.5(\alpha'\tau + \beta'\tau^2), \quad (4)$$

where α', β' and τ are functions of mass:

$$\alpha' = 0.1594 + 0.1348 \log_{10} m,$$

$$\beta' = 0.144 - 0.833 \log_{10} m$$

and

$$\tau = t/t_{\mathrm{ms}},$$

and the main-sequence lifetime is given by

$$t_{\mathrm{ms}} = 10^6 \left(\frac{2550 + 669m^{2.5} + m^{4.5}}{0.0327m^{1.5} + 0.346m^{4.5}} \right) \mathrm{yr}. \quad (5)$$

We have assumed that evolution in the V band is the same as that of bolometric luminosity. Stars become bluer as they evolve across the main sequence, but we need not devise a more detailed model because we show below that the effects of main-sequence evolution are small, affecting mainly stars bluer than $V-I \approx 1.5$.

3.1.3 *Contribution to cosmic scatter*

To estimate the contribution to the dispersion in absolute magnitudes, we generate 5000 stars with masses in the range $1 \ge m \ge 0.08\ \mathrm{M}_\odot$. The lower mass cut-off is taken to be the minimum mass for hydrogen burning, and an upper mass cut-off is used so as not to generate stars with masses outside our regime of interest. Masses are chosen at random from the distribution given in equation (1) with the parameters found in Section 2. The mass generating function is derived in KTG2. For each stellar mass we obtain the corresponding absolute visual magnitude, M_V, from our adopted mass – M_V relation, and the absolute I-band magnitude, M_I, from

$$M_V = 3.34(V-I) + 2.89, \quad (6)$$

found by SIP. Given the age, t, for each system, we then determine the changed magnitude $M'_V = M_V + \delta M_{V,\mathrm{age}}$, and we assume that the effective temperature remains approximately constant so that $V-I$, which is a good temperature indicator (see for example Leggett & Hawkins 1988), also remains constant. This is not correct over the whole range but, as we shall show, the age contributions to cosmic scatter are small and it is not necessary to devise a more detailed model. Fig. 4 shows a plot of the residuals $\delta M_V = M'_V - M_V$ against $V-I$, and we see that evolution on the main sequence is only noticeable at the high-mass end, whereas pre-main-sequence evolution causes some scatter over much of the mass range but mostly towards the low-mass end. The overall contribution to $\sigma(M_V)$ is 0.11 mag.

It is instructive to evaluate the proportion of stars 0.1 mag brighter than the main sequence. For this purpose we consult Table 2, where we list the number of stars in colour and magnitude bins.

From Table 2 it can be seen that 6 per cent of all stars with $0.5 < V-I < 4.5$ are brighter by 0.1 mag than the main sequence; 52 per cent of all stars with $0.5 < V-I < 1.8$ have brightened ≥ 0.1 mag in the course of their main-sequence evolution; and 3.3 per cent of all stars with $1.8 < V-I < 4.5$ are pre-main-sequence stars brighter by ≥ 0.1 mag than the main sequence, of which 91 per cent are redder than $V-I = 3.05$. The resultant systematic effects in each colour interval are summarized by computing linear regression fits as listed in Table 2. We see that the effects of evolution on the main sequence are noticeable in the interval $0.5 < V-I < 1.8$.

3.2 Metallicity

For a given star of mass m, we need to convert the deviation in abundance, δ[Fe/H], to changes in absolute V- and I-band magnitudes. There exists no empirical determination of functional relationships between the changes in magnitude, $\delta M_{V,\mathrm{met}}$ and $\delta M_{I,\mathrm{met}}$, and δ[Fe/H] for low-mass stars. We consult the theoretical models of VandenBerg (1985), who calculates M_V and $V-I$ for five values of metallicity in the range $-1.0 \le$ [Fe/H] ≤ 0.0 for stars with masses between 0.7 and 3.0 $\mathrm{M}_\odot$. These models are based on synthetic stellar spectra computed with flux-constant, blanketed model atmospheres (VandenBerg & Bell 1985). In Table 3 we list the numbers relevant for our purpose. We adopt the notation δ[Fe/H] instead of [Fe/H] to signify the changes in M_V and $V-I$ for a given change in metal abundance.

We find the following formulae to be a good representation of the data in Table 3:

$$\delta M_{V,\mathrm{met}} = \delta_V = \beta(m)\,\delta[\mathrm{Fe/H}] + \gamma(m)\,\delta[\mathrm{Fe/H}]^2, \quad \delta[\mathrm{Fe/H}] < 0; \quad (7)$$

$$\delta M_{I,\mathrm{met}} = \delta_I = \delta_V - \{\eta(m)\,\delta[\mathrm{Fe/H}] + \nu(m)\,\delta[\mathrm{Fe/H}]^2\}, \quad \delta[\mathrm{Fe/H}] < 0;$$

where $0.7 \le m \le 1.1\ \mathrm{M}_\odot$ is the stellar mass, and

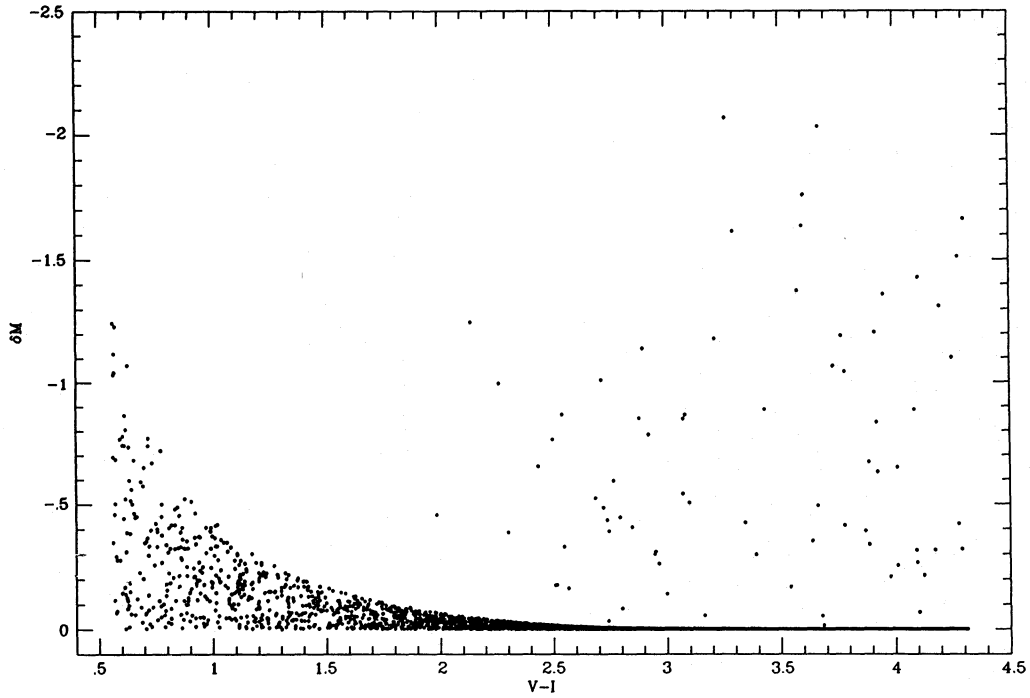

Figure 4. The scatter in the absolute-magnitude–colour relation owing to a spread of ages (see Section 3.1.3). The residuals, $\delta M_V = M'_V - M_V$, are plotted, where M'_V is the simulated absolute magnitude of the star with simulated colour $V-I$, and M_V is obtained from equation (6).

Table 2. Distribution of stars, due to evolution, in colour and magnitude bins.

$-\delta M_V$	0.5–1.8	1.8–3.05	3.05–4.5	1.0–4.5
0.0–0.1	287	2189	2148	4580
0.1–0.5	273	15	16	194
0.5–0.9	26	7	10	17
0.9–1.3	6	4	6	10
1.3–1.7	0	0	8	8
>1.7	0	0	3	3
a	2.37	2.81	2.90	2.81
b	3.63	3.37	3.33	3.36
σ	0.15	0.07	0.14	0.11
σ_{SIP}	0.24	0.07	0.14	0.11

Notes: $M_V = a + b(V-I)$; a, b and the dispersions are estimated by linear regression on the equations given in the table $[\sigma(M_V)]$ or on equation (6) $[\sigma(M_V)_{SIP}]$ (SIP: $a = 2.89$, $b = 3.34$).

$$\beta(m) = -2.16 + 16.57m - 16.02m^2 - 0.55m^3 + 3.72m^4,$$

$$\gamma(m) = -5.36 + 17.67m - 10.79m^2 - 6.04m^3 + 5.16m^4,$$

$$\eta(m) = -1.62 + 9.48m - 8.94m^2 - 1.06m^3 + 2.57m^4,$$

$$\nu(m) = -3.00 + 10.16m - 8.05m^2 - 0.68m^3 + 1.73m^4.$$

In the absence of data for $\delta[\mathrm{Fe/H}] > 0$, we assume that $\delta M_{V,\mathrm{met}}$ and $\delta M_{I,\mathrm{met}}$ are symmetric about $\delta[\mathrm{Fe/H}] = 0$. For masses below 0.7 $M_\odot$, we note that the locus of extreme subdwarfs appears to lie at approximately constant distance below the lower Population I main sequence, irrespective of colour to $V-I \approx 2.5$, redder than which no subdwarfs are apparent (Monet et al. 1992). This suggests that $\delta M_V(m)$ and $\delta(V-I)(m)$ are approximately constant and only dependent on metallicity on the lower main sequence. On the other hand, molecular bands originating in the stellar atmosphere become dominant absorption agents for stars less massive than $\approx 0.5\ M_\odot$, and these saturate very quickly with increasing metal abundance. The net result may be an insensitivity of the V and I bands to metal abundance variations for the faintest main-sequence stars.

Table 3. δM_V and $\delta(V-I)$ as functions of δ[Fe/H] and stellar mass for stars on the zero-age main sequence (VandenBerg 1985).

m ($M_\odot$)	δ[Fe/H]	$\delta M_{V,\mathrm{met}}$ (mag)	$\delta(V-I)$ (mag)
0.7	−0.23	−0.479	−0.183
	−0.46	−0.865	−0.334
	−0.76	−1.220	−0.471
	−1.00	−1.397	−0.537
0.8	−0.23	−0.451	−0.163
	−0.46	−0.775	−0.277
	−0.76	−1.057	−0.373
	−1.00	−1.201	−0.421
0.9	−0.23	−0.383	−0.121
	−0.46	−0.658	−0.207
	−0.76	−0.901	−0.278
	−1.00	−1.022	−0.316
1.0	−0.23	−0.348	−0.100
	−0.46	−0.582	−0.163
	−0.76	−0.804	−0.228
	−1.00	−0.927	−0.273
1.1	−0.23	−0.296	−0.075
	−0.46	−0.523	−0.138
	−0.76	−0.746	−0.219
	−1.00	−0.853	−0.272

Note: $\delta(V-I) = \delta M_{V,\mathrm{met}} - \delta M_{I,\mathrm{met}}$.

Consequently, we test two somewhat ad hoc models which limit the range of likely behaviour. One model, which we shall refer to as model 'c', assumes that the parameters β, γ, η and ν are constant below some mass m_c. The second model, which we shall refer to as model 'l', assumes that the above four parameters remain constant in the mass interval $m_c \geq m \geq m_l$ and decrease linearly to zero with decreasing mass in the range $m_l \geq m \geq 0.07$ $M_\odot$. We adopt $m_c = 0.61$ $M_\odot$ which, very roughly, yields a displacement of the δ[Fe/H] $= -1.6$ lower main sequence from the δ[Fe/H] $= 0$ main sequence by ≈ 1.5 mag in the V band. This is about correct when compared to the theoretical mass–M_V relation for the globular cluster M13 (Drukier et al. 1988). Concerning m_l, we simply assume that molecular absorption saturates rapidly below the 'H_2 peak', and we set $m_l = 0.3$ $M_\odot$.

In Fig. 5 we demonstrate both models by showing the displacement of different δ[Fe/H] loci, and we also demonstrate the displacement from the main sequence in V and $V-I$ of a particular stellar mass as its metallicity is changed. We note that the position of a star is displaced essentially

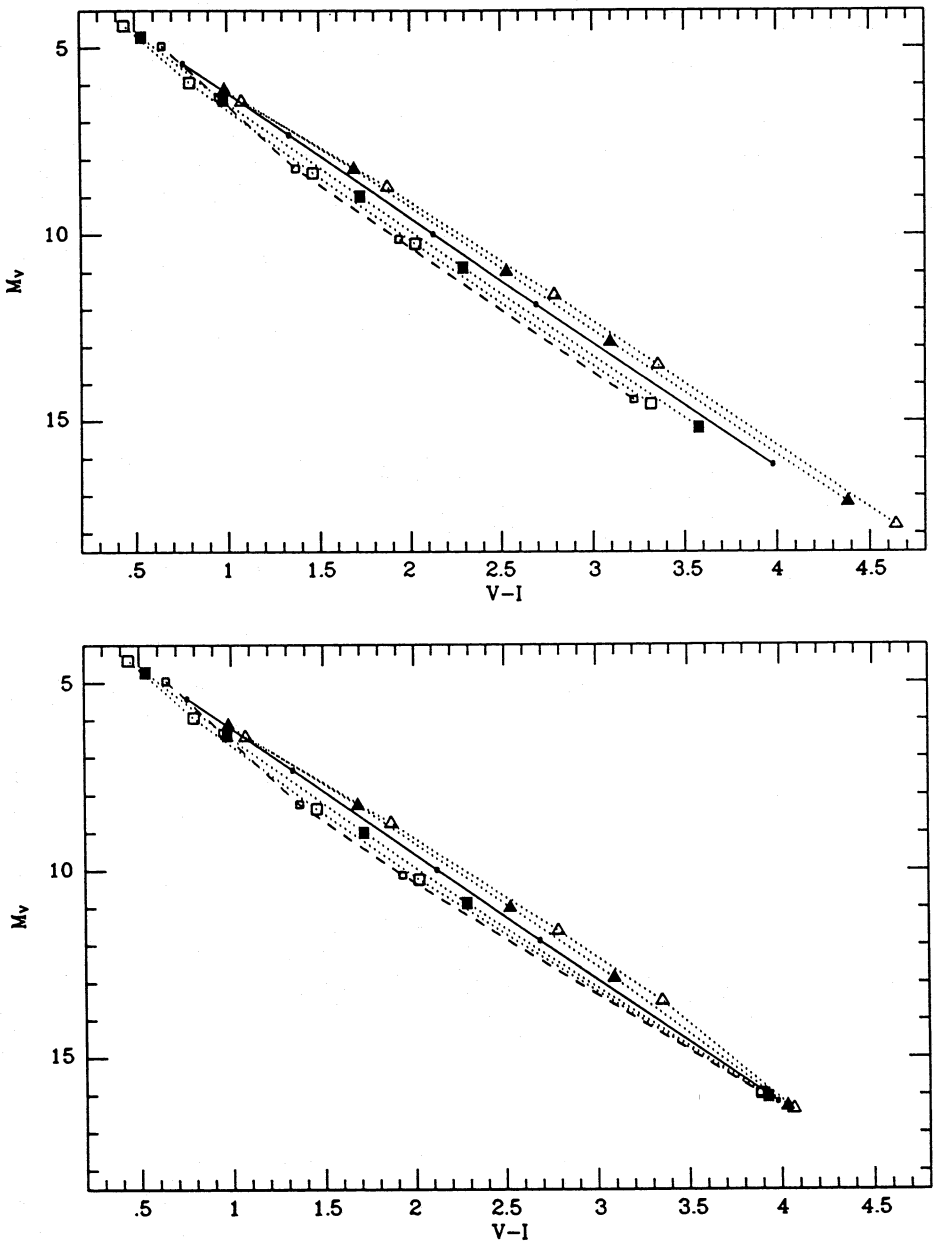

Figure 5. The top panel demonstrates model 'c' and the lower panel model 'l' (see Section 3.2). In both, the solid line denotes the main sequence given by equation (6). The main sequences for various abundance offsets are shown by the dashed line (δ[Fe/H] $= -2$) and the dotted lines (from bottom to top) for the following values: δ[Fe/H] $= -1$, -0.5, $+0.5$ and $+1$. The positions of masses $m = 0.9$, 0.7, 0.5, 0.3 and 0.1 $M_\odot$ are shown by solid dots, and their displacement away from the δ[Fe/H] $= 0$ main sequence (solid line) is given by squares for δ[Fe/H] < 0 and triangles for δ[Fe/H] > 0.

parallel to the main sequence at the blue end and leads to a very small scatter of points about the main sequence at $V-I \approx 0.5$–1.

We model the δ[Fe/H] distribution by a Gaussian with mean at 0 dex and a standard deviation of 0.2 dex. We exclude δ[Fe/H] > +0.5, because we assume that both the mass–M_V data compiled by Popper (1989) and the data used by SIP to derive the colour–magnitude relation given by equation (6) have the metallicity distribution determined by Gilmore & Wyse (1985). That is, we assume that these relations are valid for a population of stars with mean [Fe/H] = −0.3, and we are interested in deviations as a function of δ[Fe/H] and stellar mass m away from these relations. Adoption of a mean of −0.3 dex instead of the solar value used in the derivation of equation (7) slightly overestimates the spread in M_V for a given spread in abundance but, in view of the uncertainties inherent to the theoretical work caused by the effects of line blanketing, we adopt this simpler model. We generate $N = 5000$ stars as in Section 3.1.3 and perturb the M_V and M_I values by adding $\delta M_{V,\mathrm{met}}$ and $\delta M_{I,\mathrm{met}}$, respectively. In Fig. 6 we plot the residuals of the colour–magnitude data if all contributions to cosmic scatter apart from the metallicity dispersion are excluded. Two features are apparent in the figure. First, stars lying on the faint side of the solid line ($\delta M_V > 0$) are metal-deficient, whereas stars on the bright side are metal-rich. Secondly, in model 'c', metal-rich stars appear redder and fainter than the $M_V = 17.3$ limit imposed by the model.

By fitting a linear regression line to the model data points in the $V-I$ range 1.0–4.7, we obtain $M_V = 3.31(V-I) + 2.99$ with a contribution to cosmic scatter of $\sigma(M_V) = 0.14$ for model 'c', and $M_V = 3.32(V-I) + 2.94$ with $\sigma(M_V) = 0.10$ for model 'l'. These relations are represented by dotted lines in Fig. 6, and for comparison we also represent equation (6) by a solid line.

In Table 4 we tabulate the systematic effects over the colour ranges used in Table 2.

3.3 Parallax

The stars selected to define the absolute-magnitude–colour relation have well-determined parallaxes with uncertainties no larger than 10 per cent. Even this uncertainty will introduce some scatter, but the systematic effects can be corrected by applying the L–K correction (Lutz & Kelker 1973). To investigate the contribution of such a corrected sample to the

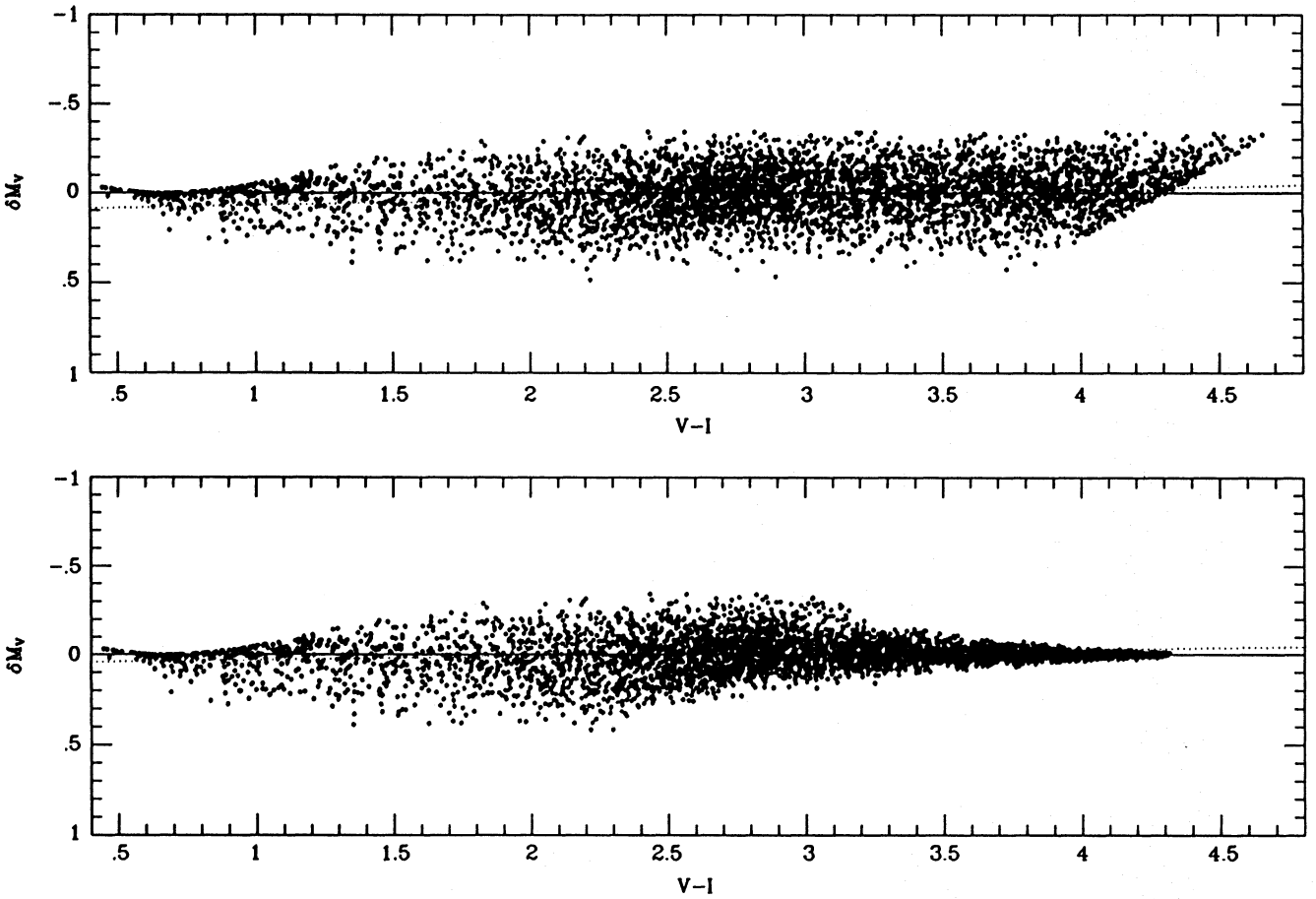

Figure 6. The scatter in the absolute-magnitude–colour relation owing to a spread of metallicities (see Section 3.2). The residuals, $\delta M_V = M'_V - M_V$, are plotted, where M'_V is the simulated absolute magnitude of the star with simulated colour $V-I$, and M_V is obtained from equation (6). The top panel illustrates model 'c' and the lower panel model 'l'. The former model assumes that the variation of M_V with δ[Fe/H] is constant below $\approx 0.6\ \mathrm{M}_\odot$, whereas the latter assumes that the scatter due to the chemical abundance dispersion reduces to negligible values at the hydrogen-burning mass limit. In both cases, the solid line is equation (6) and the dotted line is the relation obtained by linear regression on data given here.

cosmic scatter, we fit the corrections listed by Lutz & Kelker to the absolute visual magnitudes as a function of σ/π:

$$\log_{10}(\delta M_{V,\mathrm{LK}}) = 14.41\sigma/\pi - 2.370, \quad (8)$$

where σ is the uncertainty associated with the parallax π.

We generate absolute V- and I-band magnitudes from the stellar masses, the mass–M_V relation and equation (6). We take an isotropic and homogeneous distribution and for each star generate a distance, d, within 20 pc (KTG2). Using this distance, we calculate the apparent magnitudes and the colours, $V-I$. For each parallax we calculate an error from $\sigma = 0.0072 + 0.0037\mathcal{G}$, where $\mathcal{G}$ is a Gaussian random variate with zero mean and unit variance. This distribution of errors was derived from the parallaxes and their uncertainties listed by Gliese (1982) for stars within 5.25 pc. For each star we calculate an actual error $\delta\pi = \sigma\mathcal{G}'$, where $\mathcal{G}'$ is a Gaussian random variate, and add this to the parallax, π, which becomes $1/d + \delta\pi$. From these and the apparent magnitudes, we obtain the absolute magnitudes of all 5000 systems. We accept only those stars for which $\sigma/\pi \leq 0.1$ (as do SIP), losing about 2600 stars. We plot the residuals in Fig. 7. The scatter about the linear regression line, $M_V = 3.34(V-I) + 2.91$, is $\sigma(M_V) = 0.140$ mag.

We also correct each absolute visual magnitude by the L–K correction, equation (8), to find that, as expected, the resulting data show just as much scatter: $\sigma(M_V) = 0.141$ mag, with a linear regression line $M_V = 3.34(V-I) + 2.87$. The average L–K correction we obtain for our model data amounts to -0.041 mag, which is in fair agreement with the value obtained by SIP (-0.03 mag). The plot of these data is indistinguishable from Fig. 7, apart from the 0.04-mag change in the zero-point.

Table 4. Systematic effects owing to the spread of metallicities (see also Table 2).

	$V-I$			
model 'c'	0.5–1.8	1.8–3.05	3.05–4.5	1.0–4.5
a	2.89	3.12	3.11	2.99
b	3.36	3.26	3.27	3.31
σ	0.10	0.14	0.14	0.14
σ_{SIP}	0.11	0.14	0.14	0.14
model 'l'				
a	2.89	3.18	2.82	2.94
b	3.36	3.23	3.36	3.32
σ	0.10	0.12	0.05	0.10
σ_{SIP}	0.11	0.13	0.05	0.10

3.4 Binary stars

We now combine the stars into systems such that a fraction f consist of two hydrogen-burning stars of equal age and the remaining $1-f$ systems are single hydrogen-burning stars.

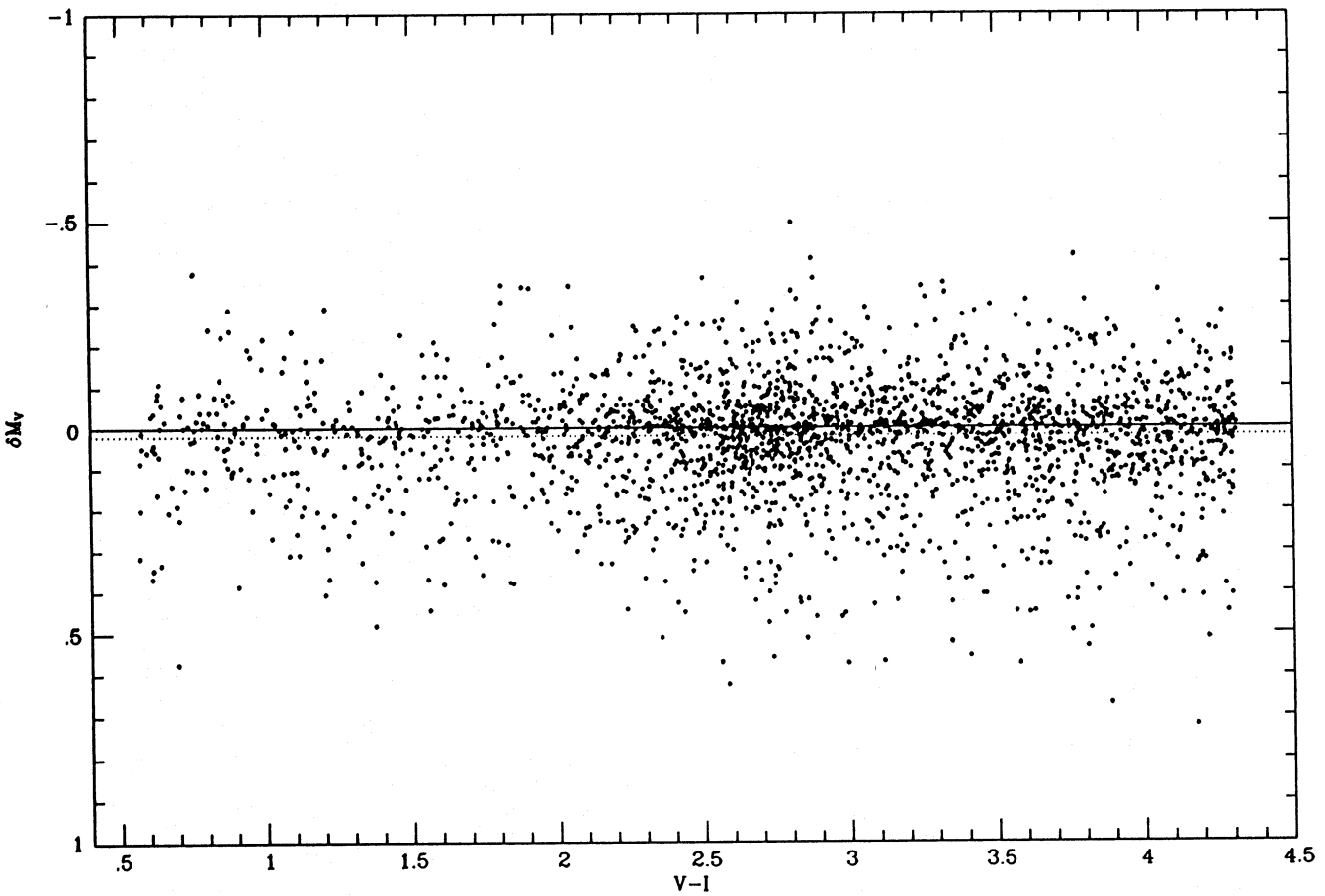

Figure 7. The scatter in the absolute-magnitude–colour relation owing to parallax errors (see Section 3.3). The residuals, $\delta M_V = M'_V - M_V$, are plotted, where M'_V is the simulated absolute magnitude of the system with simulated colour $V-I$ and M_V is obtained from equation (6).

The masses of the components of a binary system are uncorrelated and chosen from the same mass function (equation 1), with the parameters found in Section 2.

Known binary stars are omitted from stellar samples used in the calibration of the absolute-magnitude–colour relation. Nevertheless, we expect some contamination by unresolved binaries, since binarity appears to be very common. We emphasize that unresolved binaries contribute a lesser amount to the cosmic scatter estimated from standard trigonometric parallax samples than to the cosmic scatter in stellar samples obtained from photographic plates. In KTG2 we estimate the scatter owing to binaries alone to be $\sigma(M_V)=0.27$ mag, with a linear regression fit of $M_V=3.23(V-I)+2.84$, if a fraction $f=0.8$ of all stars are unresolved binary systems. In what follows, we shall denote as $f_{\rm trig}$ the effective fraction of residual binaries in the trigonometric sample used by SIP to derive equation (6). We refer to $f_{\rm trig}$ as the effective fraction rather than the actual fraction of residual binaries, because those systems removed by SIP will be biased towards systems with equal-mass components and wide separations. The actual residual fraction is likely to be larger than $f_{\rm trig}$, consisting predominantly of close systems with a large mass ratio.

In Table 5 we tabulate the systematic effects in the colour ranges used in Table 2 for different values of $f_{\rm trig}$. Fig. 8 shows the distribution in the colour–magnitude diagram of the residuals for $f_{\rm trig}=0.4$ and 0.8.

Table 5. Systematic effects owing to binaries (see also Table 2).

	$V-I$			
	0.5–1.8	1.8–3.05	3.05–4.5	1.0–4.5
$f_{\rm trig}=0.2$				
a	2.89	2.88	2.61	2.79
b	3.31	3.31	3.40	3.35
σ	0.10	0.21	0.18	0.19
$\sigma_{\rm SIP}$	0.11	0.23	0.20	0.21
$f_{\rm trig}=0.4$				
a	2.90	2.86	2.32	2.78
b	3.27	3.28	3.46	3.32
σ	0.14	0.26	0.26	0.25
$\sigma_{\rm SIP}$	0.16	0.31	0.30	0.29
$f_{\rm trig}=0.6$				
a	2.94	2.90	2.25	2.75
b	3.22	3.23	3.45	3.30
σ	0.15	0.27	0.30	0.28
$\sigma_{\rm SIP}$	0.18	0.38	0.39	0.37
$f_{\rm trig}=0.8$				
a	2.93	2.99	2.26	2.84
b	3.21	3.17	3.41	3.24
σ	0.16	0.26	0.30	0.27
$\sigma_{\rm SIP}$	0.20	0.43	0.49	0.43
$f_{\rm trig}=1.0$				
a	2.93	3.07	3.11	3.03
b	3.20	3.11	3.11	3.13
σ	0.16	0.23	0.14	0.20
$\sigma_{\rm SIP}$	0.21	0.46	0.61	0.48

3.5 Resultant cosmic scatter

Figs 4, 6, 7 and 8 contrast the differences between the contributions to cosmic scatter. The overall cosmic scatter can be estimated if all the above contributions are combined.

We proceed as above, finding the absolute V- and I-band magnitudes for each star. Each of these absolute magnitudes is then adjusted to the appropriate age (equal age for both components in a system) and to the appropriate metallicity (equal composition for both stars in a system). The resulting absolute magnitudes are combined to give the system absolute magnitudes. For each system we also generate a distance, d, within 20 pc, as above. A Gaussian error term of standard deviation $\sigma_{\rm phot}$ is added to each apparent magnitude independently for both photometric bands, and the $V-I$ colour is obtained. As above, an error in measurement is added to the parallax to yield the absolute visual magnitude of the system which is corrected by the L–K correction. Only stars with a trigonometric parallax uncertainty of better than 10 per cent are included.

Our aim is to model cosmic scatter such that $\sigma(M_V)\approx 0.5$, which is the value measured by SIP. We need to derive a colour–magnitude relation corrected for systematic effects, but based on equation (6) so that our analysis of the SIP star-count data is consistent with their work. Using $\sigma_{\rm phot}=0.02$ mag (Leggett & Hawkins 1988) and generating $N=5000$ systems, and for the moment assuming $f_{\rm trig}=0.4$, we obtain $\sigma(M_V)=0.33$ for both models 'c' and 'l' in the magnitude range $1.0<V-I<4.7$. We note that Leggett & Hawkins collated trigonometric parallax standards from eight different sources, and we might expect $\sigma_{\rm phot}>0.02$ mag. Indeed, using a high-quality homogeneous sample of trigonometric parallax stars, Reid (1982) finds $\sigma(M_V)=0.35$, which is essentially identical to our model above. Our model for cosmic scatter thus appears to be successful and suggests strongly that external errors form an important contribution to the scatter in the standard sample analysed by SIP. Monet et al. (1992) discuss differences in the photometry of different workers. In some cases, the differences amount to ≈ 0.1 mag in V and I. Hence we vary $\sigma_{\rm phot}$ until $\sigma(M_V)\approx 0.5$ mag and obtain $\sigma_{\rm phot}=0.09$ mag. We adopt this value as the standard deviation of the single Gaussian measurement error distribution in the photometry of the parallax standards used by SIP to derive equation (6). The resulting residual magnitude–colour diagrams are shown in Fig. 9 where, for illustrative purposes, we only generate $N=1000$ systems, of which about 500 appear in the plots. The linear regression line (model 'c') in the interval $V-I=1.0$–4.7 (the range used by SIP) for 5000 stellar systems, $M_V=3.28(V-I)+2.86$, has a dispersion of $\sigma(M_V)=0.49$ mag. Similarly, for model 'l' we obtain $M_V=3.29(V-I)+2.83$, again with $\sigma(M_V)=0.49$. Both these relations are shown in Fig. 9.

3.6 Corrected colour–magnitude relations

The relation taken from SIP and given by equation (6) should correspond to the final fit, so we adjust the colour–magnitude relation to compensate (assuming for the moment that $f_{\rm trig}=0.4$) and find, for model 'c', $M_V=3.42(\pm 0.01)(V-I)+2.89(\pm 0.04)$. A similar simulation with $N=5000$, using this relation instead of (6), yields a linear regression line that is the SIP relation (equation 6) for model 'c'. Similarly, we correct the colour–magnitude relation assuming model 'l' and find $M_V=3.40(V-I)=2.93$. For

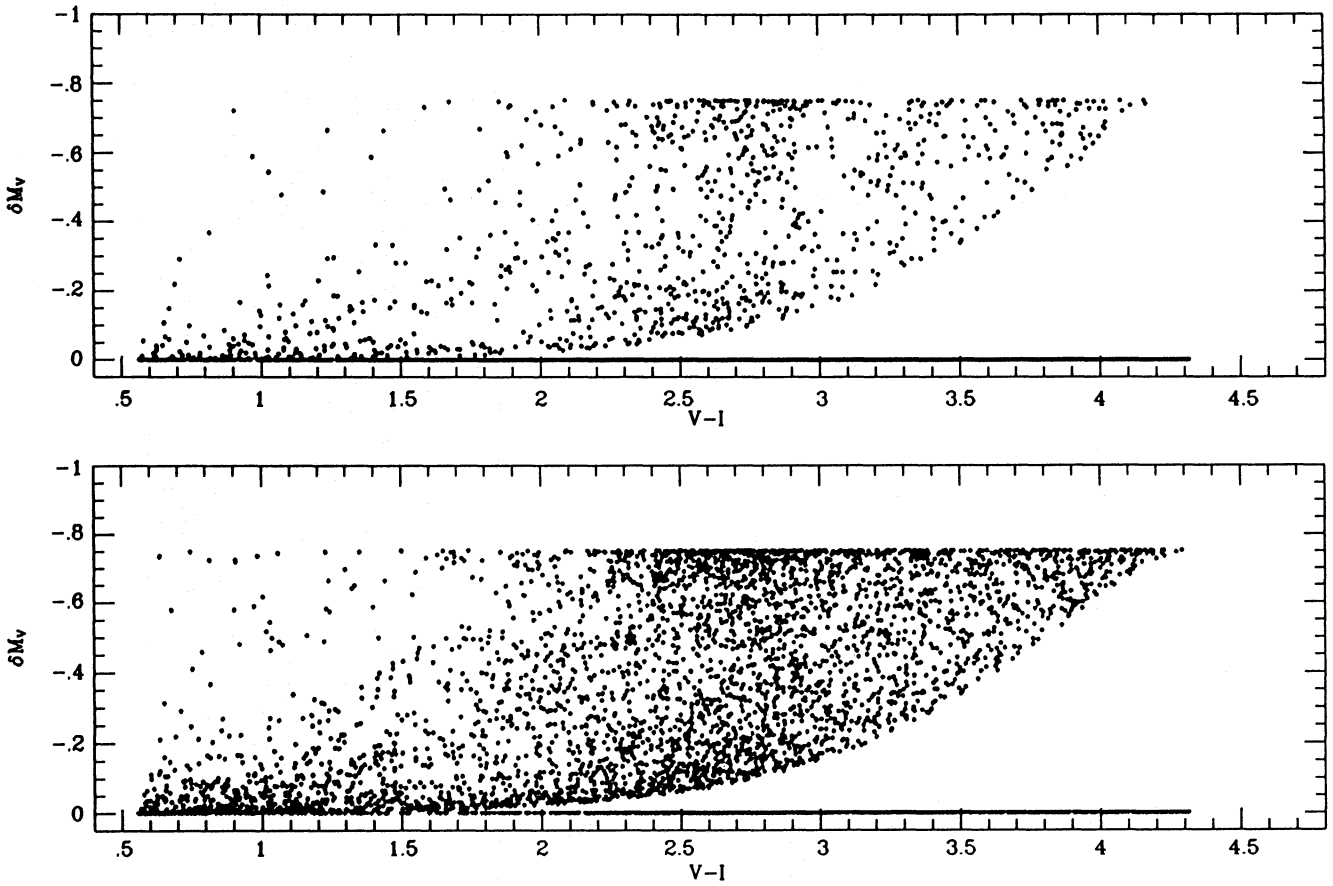

Figure 8. The scatter in the absolute-magnitude–colour relation owing to binaries (see Section 3.4). Upper panel: $f_{\rm trig}=0.4$; lower panel: $f_{\rm trig}=0.8$. The residuals, $\delta M_V = M'_V - M_V$, are plotted, where M'_V is the simulated absolute magnitude of the system with simulated colour $V-I$ and M_V is obtained from equation (6).

later use, we derive relations corrected for other values of $f_{\rm trig}$, which we tabulate in Table 6. We compare these simulations with the cosmic scatter measured by SIP, which is $\sigma(M_V)=0.51$ mag, and deduce that the above model gives, for our purpose, a good description of the stellar population.

It is instructive to evaluate $\sigma(M_V)$ in different $V-I$ ranges. We do this by generating $N=5000$ systems assuming $f_{\rm trig}=0.4$, and using the relations corrected for this $f_{\rm trig}$ in Table 6 to transform M_V to M_I for each star, as above. We fit linear regression lines to each $V-I$ subrange. The dispersion of data about these lines with slope b is $\sigma(M_V)$, and $\sigma_{\rm SIP}$ about equation (6). We also tabulate the mean residual, $\overline{\delta M_V}$, with respect to equation (6). The number of data points entering these estimates is typically 120 at the blue and red ends, and 450 in the middle of the $V-I$ range. In Table 7 we list the results for $\sigma_{\rm phot}=0.09$ and 0.01 mag.

The values in Table 7 demonstrate the systematics prevalent in a colour–magnitude diagram. The scatter, $\sigma(M_V)$, is smaller in the $V-I$ interval 1.0–1.5 than in the $V-I=0.5$–1.0 interval, because evolution across the main sequence contributes less for the less massive stars. All the other effects have not become important yet. Their influence increases at redder $V-I$. Although the scatter remains approximately constant, we note that the mean residuals change systematically. Thus at the blue end the data are brighter and at the red end they are fainter than equation (6), even though we have used a corrected colour–magnitude relation. This comes about because our fits leading to the entries in Table 6 are sensitive primarily to the colour range $V-I=2.5$–3.0, where the peak in the luminosity function lies, which demonstrates that a linear M_V, $V-I$ relation is only a first-order approximation.

On the basis of Gliese catalogue data with $\sigma_\pi/\pi<0.13$, and with photometry from Bessell (1990), Reid (private communication) points out that the scatter about equation (6), $\sigma_{\rm SIP}$, increases from $\sigma_{\rm SIP}=0.33$ for $6<M_V<8$ to $\sigma_{\rm SIP}=0.52$ for $11<M_V<14$. This is larger than the increase we simulate in Table 7, unless the photometry has an uncertainty of $\sigma_{\rm ph}=0.01$ mag in the former magnitude range and $\sigma_{\rm ph}=0.09$ mag in the latter range. Although it is perfectly possible that our model does not account fully for differential line blanketing effects for $M_V>7.5$, we do not, at this stage, devise a more detailed metallicity model. In view of the discussion by Monet et al. (1992), we attribute the increase in $\sigma_{\rm ph}$ noticed by Reid to deteriorating photometric quality with increasing M_V.

We have now to decide which of the corrected M_V, $V-I$ relations is to be used in the subsequent analysis. It is very difficult to establish to what degree the trigonometric parallax sample of SIP is contaminated by unresolved binaries. By the nature of the sample, we expect contamination to be small. An independent derivation of the relation

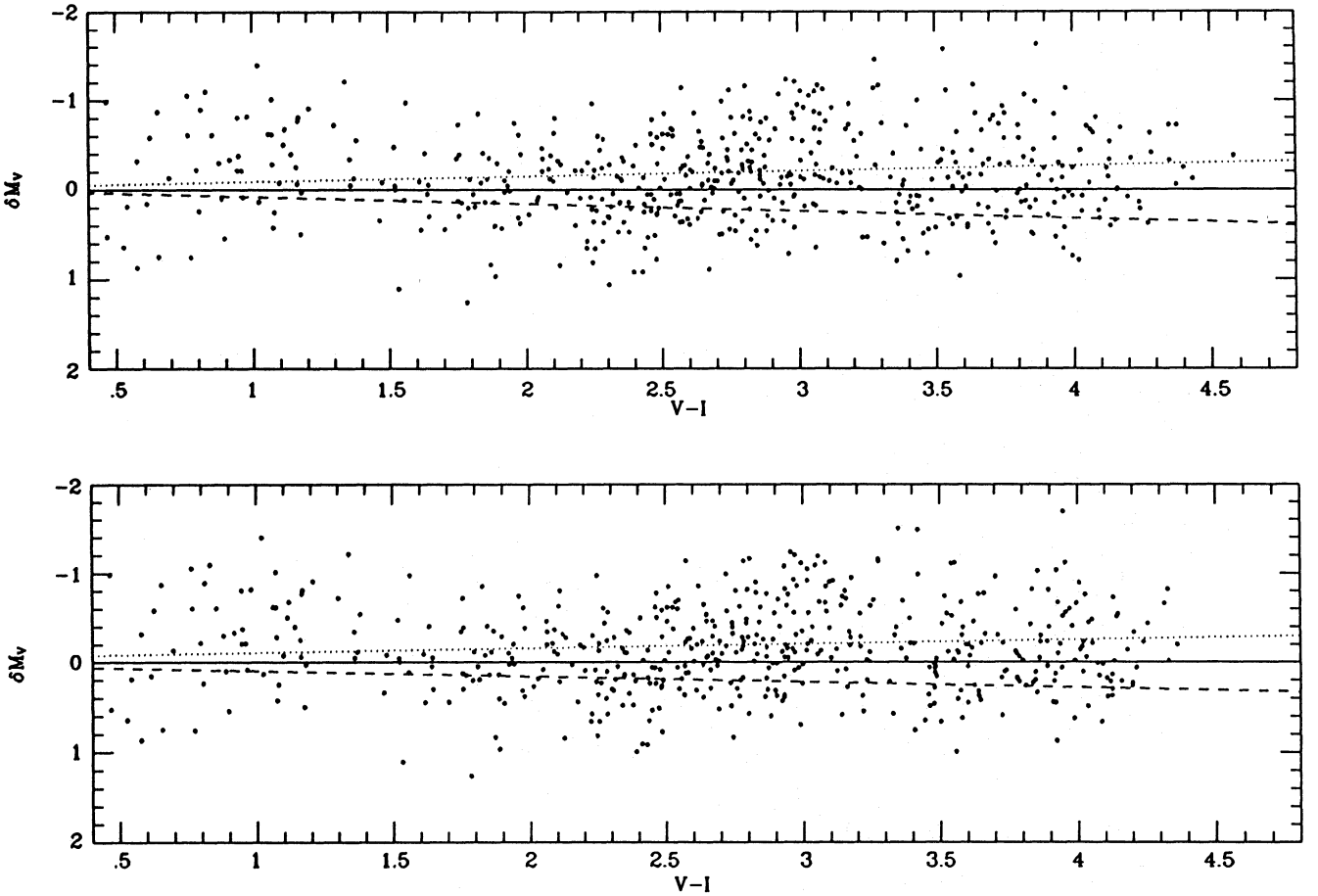

Figure 9. The scatter in the absolute-magnitude–colour relation owing to a combination of an age spread, a metallicity dispersion, binarity (assuming $f_{\rm trig}=0.4$) and trigonometric parallax errors. The top panel illustrates model 'c', and the lower panel model 'l' (see Section 3.2 and Fig. 6). In both cases, the solid line is equation (6) and the dotted line is the relation obtained by linear regression on data generated using equation (6). The dashed line represents the corrected relation. The residuals, $\delta M_V = M'_V - M_V$, are plotted, where M'_V is the simulated absolute magnitude of the system with simulated colour $V-I$ and M_V is obtained from equation (6).

between M_V and $V-I$, although based on a sample which overlaps to some extent the sample used by SIP, is provided by Bessell (1991) and Monet et al. (1992). In Fig. 10 we plot some of our corrected relations from Table 6 (model 'c'), and compare these with the mean values obtained from the photometric and spectroscopic observing programme by Bessell and listed in his table 2. On the basis of this comparison with Bessell's data, which we expect to suffer very little from contamination by unresolved binaries, we prefer the colour–magnitude relations corrected for $f_{\rm trig}<0.4$. A comparison with the trigonometric parallax data published by Monet et al. allows the same conclusion. We return to this problem in Section 7.2.

4 THE DATA

4.1 An apparent-magnitude-limited sample towards the North Galactic Pole

A complete sample of low-mass stars within a photometric distance of about 130 pc, used to derive a luminosity function, is published by SIP. They obtained this sample from North Galactic Pole (NGP) star-count data within a solid angle of 18.88 deg^2 from Schmidt telescope plates measured with the COSMOS machine. In order to include the reddest stars, they applied an I-band limit $I\leq 16$, but stars fainter than $V=19$ were not calibrated. Giant star contamination is reduced to an insignificant level by selecting $V-I>1.5$ and $V>13$. Stars in the range $1.5<V-I<3.258$ are included in the sample only if their photometric distance, $d_{\rm p}$, from their apparent magnitude and equation (6), is less than 130 pc. For redder stars the sample remains complete to smaller distances, and we approximate the distance completeness limit in parsecs as a function of colour, using the data in table 1 of SIP, by

$$d_{\rm limit} = 1.445\times 10^4 (V-I)^{-4}. \qquad (9)$$

In their appendix A, SIP list the V and I magnitudes of 179 stars satisfying the above conditions. This sample forms the basis for our study of the stellar distribution to a distance of about 300 pc towards the NGP.

4.2 The immediate solar neighbourhood

The sample of stars within the immediate solar neighbourhood is considered complete to a distance of 5.2 pc. DLH

Table 6. Corrected colour–magnitude relations for different f_{trig}.

	Model 'c'		
f_{trig}	a (mag)	b	$\sigma(M_V)$ (mag)
0.0	2.64	3.44	0.45
0.1	2.74	3.42	0.47
0.2	2.85	3.40	0.49
0.3	2.88	3.41	0.50
0.4	2.89	3.42	0.50
0.6	2.89	3.45	0.52
0.8	2.77	3.54	0.53
1.0	2.62	3.65	0.48
	Model 'l'		
f_{trig}	a (mag)	b	$\sigma(M_V)$ (mag)
0.0	2.70	3.42	0.44
0.1	2.80	3.40	0.46
0.2	2.89	3.39	0.48
0.3	2.93	3.39	0.49
0.4	2.93	3.40	0.49
0.6	2.92	3.44	0.51
0.8	2.82	3.52	0.52
1.0	2.66	3.64	0.48

Notes: $M_V = a + b(V-I)$; a, b and $\sigma(M_V)$ are estimated by linear regression in the interval $V-I = 1.0$–4.7 by generating $N = 5000$ systems from these equations [SIP: $a = 2.89$, $b = 3.34$ (equation 6)].

have listed all such stars fainter than absolute visual magnitude $M_V = 9.5$ with declination $\delta > -10°$. We extend this sample using the catalogue compiled by Gliese (1982) to find four stars in the magnitude range $7.5 < M_V \leq 9.5$. Henry & McCarthy (1990) found Gl 866 to consist of two stars, and we replace this star in the list of DLH by the two components Gl 866A and 866B. Henry & McCarthy measured absolute K-band magnitudes $M_{K,A} = 8.41$ and $M_{K,B} = 8.81$, which we convert to $M_{V,A} = 14.6$ and $M_{V,B} = 15.4$ using the relation $M_K = (0.45 \pm 0.2) + (0.544 \pm 0.018) M_V$ based on 40 Gliese stars listed in table 1 of Leggett & Hawkins (1988). We use parallaxes from the Gliese catalogue (Gliese 1969) and its supplement (Gliese & Jahreiss 1979). This relation, akin to equation (6), is also surprisingly linear, with a linear correlation coefficient of $r = 0.98$. Furthermore, we exclude 40 Eri C ($M_V = 12.81$) because it is the third component of a triple system with a degenerate companion, and we do not model multiple systems with evolved members. We list the sample of stars within 5.2 pc with $\delta > -20°$ and $M_V > 7.5$ in Appendix B. Additional information can be found in Henry & McCarthy (1990) and Reid (1991).

4.3 Binaries

Many 'stars' (i.e. apparently single stars) on the sky are in reality multiple systems, the most frequent of which are binaries. Estimates of the proportion of binaries among 'stars' vary between 25 and 100 per cent, but more quantifiable statements are difficult because of the complicated

Table 7. Cosmic scatter as a function of colour.

$\sigma_{phot} = 0.09$ mag

	Model 'c'				Model 'l'			
$V-I$ (mag)	$\sigma(M_V)$ (mag)	σ_{SIP} (mag)	$\overline{\delta M_V}$ (mag)	b (mag)	$\sigma(M_V)$ (mag)	σ_{SIP} (mag)	$\overline{\delta M_V}$ (mag)	b
0.5–1.0	0.52	0.54	−0.13	2.8	0.52	0.53	−0.11	2.9
1.0–1.5	0.48	0.48	−0.02	3.6	0.48	0.48	−0.01	3.7
1.5–2.0	0.50	0.51	+0.08	3.0	0.50	0.51	+0.08	3.0
2.0–2.5	0.50	0.51	+0.10	3.2	0.49	0.50	+0.08	3.1
2.5–3.0	0.50	0.50	+0.00	3.2	0.49	0.49	−0.04	3.1
3.0–3.5	0.48	0.49	+0.04	3.6	0.47	0.47	+0.01	3.5
3.5–4.0	0.53	0.54	+0.10	3.5	0.50	0.52	+0.11	3.7
4.0–4.5	0.45	0.47	+0.04	2.5	0.46	0.48	+0.01	2.1

$\sigma_{phot} = 0.01$ mag

	Model 'c'				Model 'l'			
$V-I$ (mag)	$\sigma(M_V)$ (mag)	σ_{SIP} (mag)	$\overline{\delta M_V}$ (mag)	b (mag)	$\sigma(M_V)$ (mag)	σ_{SIP} (mag)	$\overline{\delta M_V}$ (mag)	b
0.5–1.0	0.33	0.40	−0.22	3.8	0.33	0.39	−0.19	3.8
1.0–1.5	0.25	0.25	−0.02	3.5	0.25	0.25	−0.01	3.5
1.5–2.0	0.29	0.30	+0.05	3.5	0.29	0.30	+0.05	3.5
2.0–2.5	0.34	0.34	+0.04	3.3	0.33	0.34	+0.04	3.3
2.5–3.0	0.33	0.33	+0.03	3.4	0.32	0.32	+0.00	3.4
3.0–3.5	0.35	0.36	+0.08	3.3	0.31	0.32	+0.05	3.3
3.5–4.0	0.36	0.40	+0.16	3.6	0.34	0.37	+0.14	3.6
4.0–4.5	0.31	0.36	+0.19	2.8	0.31	0.39	+0.22	4.1

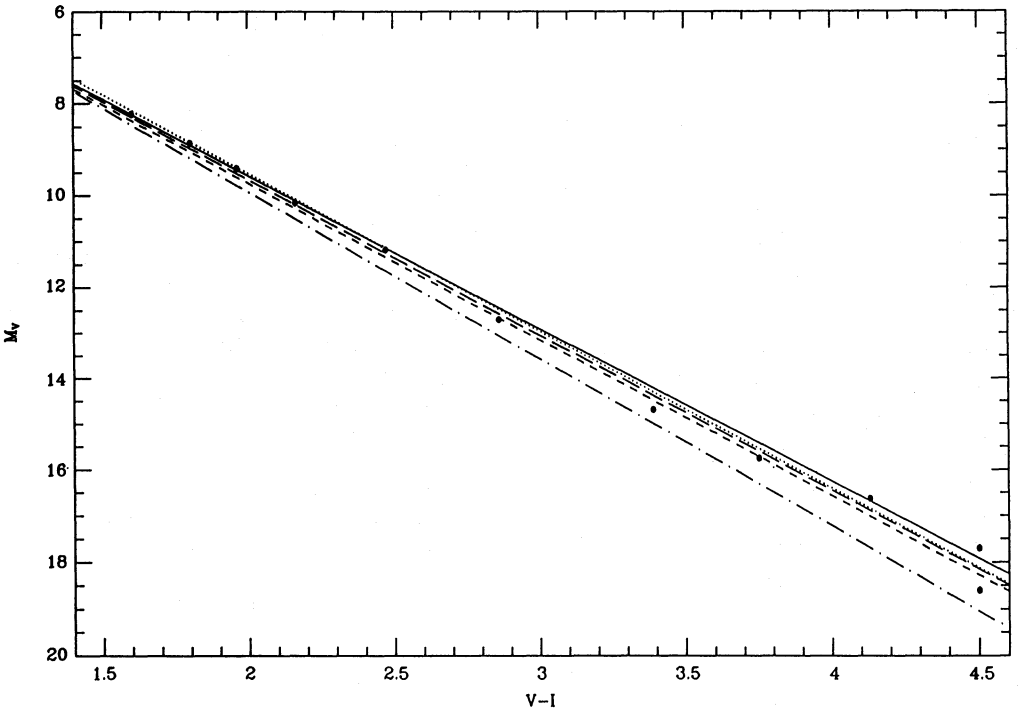

Figure 10. The colour–magnitude relations corrected for various values of the binary fraction $f_{\rm trig}$ are compared with the SIP relation (solid line) and the data listed in table 2 of Bessell (1991) (filled circles). The following corrected relations from our Table 6 (model 'c') are plotted: $f_{\rm trig}=0$ (dotted line), $f_{\rm trig}=0.2$ (long-dashed line), $f_{\rm trig}=0.4$ (short-dashed line) and $f_{\rm trig}=1$ (dash–dotted line). A similar plot of the corrected relations for model 'l' is indistinguishable from this one.

nature of the selection effects plaguing binary star studies and searches employing techniques such as direct imaging, astrometry and spectroscopic observations. It is important for our work here that we develop some idea of the size of the binary star population.

4.3.1 The binary fraction

At large distances, binary systems cannot be resolved visually, and the apparent frequency of binaries, $f_{\rm app}$, decreases quite rapidly with increasing distance. Using the data in the Gliese Catalogue of nearby stars, Brosche (1964) studied the decrease of $f_{\rm app}$ with distance. He used a simple model for the resolution criterion, the distribution of separations of the components and their magnitude differences, and found that the best-fitting model required a true binary frequency $f=1$. However, the large Poisson uncertainties precluded tight constraints, and he found that $f=0.4$ is also consistent with the data.

On considering the local (i.e. within a distance of 10 pc) binary fraction, Reid (1991) concluded that the proportion of binaries among 'stars' is consistent with a value in the range 30–50 per cent. Unfortunately, the binary star census becomes incomplete at much smaller distances than 10 pc (Brosche 1964). However, we can hope that the sample of stars within 5.2 pc is reasonably complete, and in Appendix B (Table B4) we show that this sample yields a multiplicity proportion between about 50 and about 70 per cent. On considering the different shapes of the nearby and photographically determined luminosity functions, KTG2 found that a single mass function provides the best representation of both luminosity functions if $f=1$. However, a smaller value cannot be discarded with high confidence.

Halbwachs (1986), using all available data on binary systems, concluded that the proportion of single stars among all stellar systems is at most 23 per cent when spectroscopic binaries are taken into account. An extensive long-term radial velocity study of the Hyades cluster stars reveals that at least 30 per cent of these are spectroscopic binaries and that essentially all 'stars' brighter than the Hyades main sequence are binary systems (Griffin et al. 1988). Duquennoy & Mayor (1991) made a high-precision radial velocity study of G-type stars and found at most 57 per cent of all stars in their sample to be binary, in agreement with the study of Abt (1978). The corrections applied by Mazeh et al. (1992) may, however, revise this number.

The distribution of 'stars' in the colour–magnitude diagrams of Galactic clusters is useful in studying global properties of the binary star population, because the main sequence is usually extremely well defined owing to the lack of a metallicity, age and distance dispersion. Most studies imply a photometric binary fraction of about 25 per cent, but a recent analysis of Praesepe (Kroupa & Tout 1992) suggests results consistent with a much larger proportion.

4.3.2 The mass-ratio distribution

Contradictory claims are common as to whether the components in multiple systems have correlated masses. Measurement of the mass-ratio distribution is very difficult

because the observations usually suffer from selection effects that bias towards equal-mass systems.

The results of the majority of various attempts to determine the mass-ratio distribution are found to be consistent with no correlation between the component masses in a system (Tout 1991). However, a recent study using complete samples does indicate some correlation among bright systems, i.e. stars usually more massive than the Sun (Eggleton et al. 1989). Halbwachs (1987) found that close binaries follow a similar distribution of mass ratios to binaries with wide separations, supporting the notion that component masses are uncorrelated. Duquennoy & Mayor (1991) found that systems with a solar-type primary have a distribution of secondary masses that turns over below about 0.2 $M_\odot$ and does not follow the mass function for field stars (Kroupa & Tout 1992). However, even the very carefully selected and corrected sample of Duquennoy & Mayor suffers from observational bias (Mazeh & Goldberg 1992), so that the close binaries have a different mass-ratio distribution from the wide systems. The former distribution prefers equal masses. Correlation of component masses for close systems is also found for stars within a distance of 10 pc (Reid 1991), although unequal-mass systems may remain to be discovered in this sample. Wide binaries are found to show no correlation of component masses (Close, Richer & Crabtree 1990; Reid 1991). A study of the nearby and photographically determined luminosity functions shows that both luminosity functions can be represented by one mass function if binaries are very common and if the component masses below ≈ 1 $M_\odot$ are uncorrelated (KTG2). The study of the colour–magnitude data for Praesepe (Kroupa & Tout 1992) suggests that systems bluer than $B-V \approx 0.8$ have some correlation of component masses, whereas redder systems prefer no correlation. This inference may, however, suffer from a bias towards systems with equal-mass components, because mass segregation leads to an accumulation of heavy systems near the cluster centre.

4.3.3 *Variation with system mass*

The properties of multiple systems are likely to vary with system mass. Even if the formation mechanism does not lead to a variation with system mass, variation is still expected through the statistics of pairing two stars into one system, because the mass range from which a secondary can be picked decreases with decreasing mass of the primary (Tokovinin 1992; Fisher & Marcy 1992).

In line with the findings of KTG2 and Kroupa & Tout (1992), we assume that the component masses in systems with a primary less massive than 1 $M_\odot$ are picked at random from the same mass function. We evaluate the binary proportion among all systems as a function of system absolute magnitude, f_{M_V}, and primary mass, $f_{\rm mass}$, in Fig. 11 for three choices of α_1 in equation (1), assuming that the overall binary proportion is $f=0.6$. Both f_{M_V} and $f_{\rm mass}$ decay with decreasing mass. The change in f_{M_V} is enhanced owing to Malmquist bias. For comparison, we plot the data for systems within 5.2 pc (Table B4) and the data point obtained by Duquennoy & Mayor (1991) in the top panel of Fig. 11. The decrease in f_{M_V} with M_V observed for these data agrees with the simulations of $\alpha_1 \approx 1.2$, although the Poisson uncertainties are large. However, a decrease in the observed spectroscopic

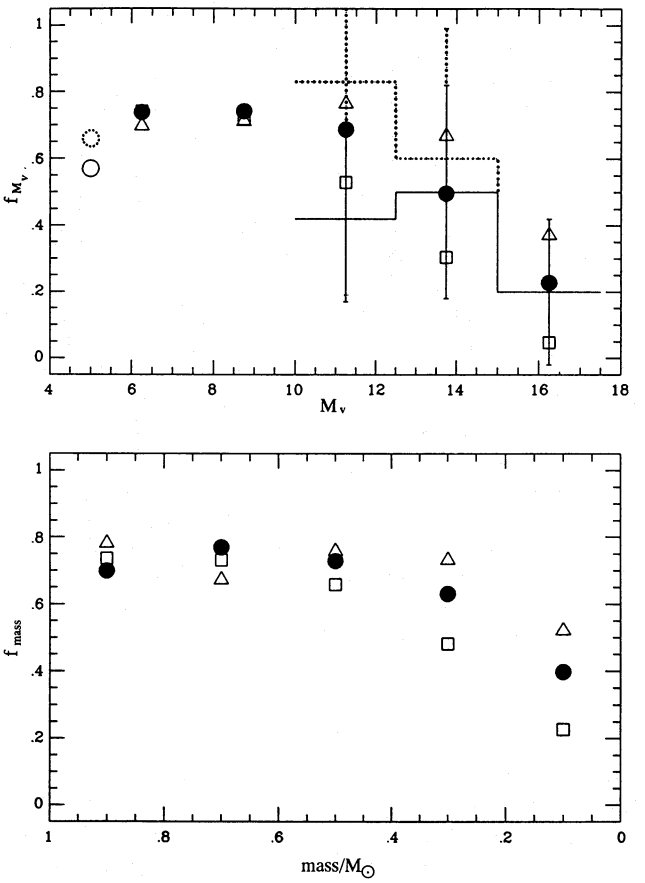

Figure 11. Top panel: the fraction of multiple stellar systems among all systems (including single and multiple stellar systems), f_{M_V}, is shown as a function of the combined absolute visual magnitude for the stars within 5.2-pc distance (Table B4). Including only the confirmed components, i.e. excluding all unseen companions, we obtain the solid histogram which shows a slight decline. Including all components, we obtain the dotted histogram. The decline in f_{M_V} with decreasing system brightness is probably partly an observational selection effect, because bright systems are easier to observe in detail than faint ones. In fact, there are no unseen companions in the last bin. The error bars represent Poisson uncertainties. Duquennoy & Mayor (1991) estimate that 57 per cent of all G dwarf stars within a distance of 20 pc are multiple systems with a mass ratio larger than 0.1. We show their result by the open circle. The dotted circle represents their result if companion masses as small as 0.01 $M_\odot$ are included in their analysis. The behaviour of f_{M_V} resulting from our simulations, assuming an overall binary proportion of $f=0.6$ and uncorrelated masses, is shown for three mass functions: $\alpha_1=0$ (open squares), $\alpha_1=1.2$ (solid circles) and $\alpha_1=2.4$ (open triangles). Lower panel: simulations of the behaviour of $f_{\rm mass}$ as a function of the mass of the primary. Symbols are as in top panel.

binary proportion among K and M stars has been found by Tokovinin (1992), who made radial velocity measurements of 200 Gliese stars. From a survey of M dwarfs within 20 pc, Fisher & Marcy (1992) have argued that their sample has a smaller incidence of stars with companions (42 ± 9 per cent) than do the G dwarfs (57 per cent).

4.3.4 *Summary and discussion*

From the above considerations, it becomes apparent that $f \approx 0.6$–0.7 is reasonable. Some correlation among com-

ponent masses in systems with a primary more massive than 0.8–1.0 $M_\odot$ is suggested (Eggleton et al. 1989; Kroupa & Tout 1992). At lower masses, the data are consistent with random pairing of component masses from the same mass function (KTG2; Kroupa & Tout 1992). In view of the uncertainties plaguing this field of study, we adopt as our working hypothesis that systems with primaries less massive than the Sun have uncorrelated component masses. We allow the overall binary fraction f to vary to identify which values are most consistent with the star-count data. Although some of the 179 SIP stars are probably triple systems, the proportion will be small, and we do not think the likely contribution is large enough to warrant the introduction of additional parameters to model triple systems. For example, the extensive study of G dwarfs by Duquennoy & Mayor (1991) suggests the ratio 6:1 for double:triple systems. In any case, our definition of f as $(1+f)N$ stars in N systems allows, albeit crudely, for systems with more than one component in that the f we attempt to derive is likely to be larger than the actual number of multiple systems. We emphasize that our hypothesis implies that f_{M_V} varies with absolute magnitude of the system, as demonstrated in Section 4.3.3.

5 THE SIMULATED DATA

The Monte Carlo method we apply is similar to that used by KTG2. Here we model a more complicated situation, because we include all the effects which move a star from the single-metallicity, single-star, single-age main sequence and affect the measured space densities of stars. The effects are different for the apparent magnitude sample observed towards the NGP and the immediate solar neighbourhood sample.

From equation (1) with $\alpha_2 = 2.2$, $m_0 = 0.5\ M_\odot$ and some α_1 which we allow to vary, we obtain $(1+f)N$ mass values in the mass range 0.08–1.0 $M_\odot$, as in Section 3. The masses are converted to absolute visual magnitude values using our mass–M_V relation. The stellar population generated represents that with mean metallicity and age characteristic of stars in the solar neighbourhood. For each star, we obtain an absolute I-band magnitude from a colour–magnitude relation corrected for some fraction, $f_{\rm trig}$, of unresolved binaries. Table 6 lists such relations, and we shall consider which to use in greater detail below. The absolute magnitudes are then changed by adding the amount $\delta M_V = \delta M_{V,\rm met} + \delta M_{V,\rm age}$ and $\delta M_I = \delta M_{I,\rm met} + \delta M_{I,\rm age}$. From here onwards, we treat the solar neighbourhood and SIP samples separately. We exclude pre-main-sequence stars from our NGP model sample, because young stars are restricted to distances from the Galactic mid-plane that are much smaller than 100 pc.

5.1 The apparent magnitude sample

We combine the first $2fN$ stars into pairs. The stars in a binary have equal ages and metallicities. We have N systems, $(1-f)N$ of which are single stars, the remainder being unresolved binaries.

For each system we generate a distance, z, above the Galactic plane such that the resulting number distribution follows a law given by

$$dN(z) = N_0 \Omega z^2 e^{-z/h} dz, \qquad (10)$$

where $dN(z)$ is the number of stars in the distance interval z to $z+dz$ and h is the scaleheight of the Galactic disc. This is equivalent to an exponential disc observed at constant solid angle Ω. We generate distances out to 300 pc and within a solid angle of 18.88 deg^2. The generating function is discussed in Appendix C, and a maximum distance of 300 pc is used because more distant stars do not affect a 130-pc distance-limited sample, as demonstrated in Section 7.2.2. An exponential distribution of stars perpendicular to the Galactic mid-plane is probably a crude approximation within ≈ 40 pc of the mid-plane, but the data are mostly too poor to warrant more elaborate models. The determination of the position of the Sun with respect to the Galactic mid-plane is a difficult problem. Star counts towards the Galactic poles rely on calibration of photographic magnitudes, which are likely to suffer systematic uncertainties at $V \approx 15$–18. The determination of the distance of the Sun from the Galactic mid-plane, $Z_\odot$, by Stobie & Ishida (1987) and Yamagate & Yoshii (1992) yields $Z_\odot \approx 40$ pc northward of the plane. Both rely on the same star-count data towards the SGP (Reid & Gilmore 1982). These data show an excess by 15 per cent in the range $15.5 < V < 18$ above equivalent NGP star-count data. Gilmore & Wyse (1987), on the other hand, find, on comparing star-count data in the direction of both poles, the stellar distribution to be symmetric to within about 10 per cent. Measurements of the distribution of CO indicate that the Sun lies only about 10 pc northward of the mid-plane (fig. 12 of Combes 1991). The measurements of the surface brightness distribution of the Galaxy by *Pioneer 10* place the Sun 12 pc from the mid-plane (van der Kruit 1989). Given the uncertainty apparent in the value of $Z_\odot$, we assume that the Sun's distance above the Galactic mid-plane is sufficiently small safely to assume symmetry of star-count data about the mid-plane. That is, we assume that the SIP data are representative of the distribution of systems perpendicular to the Galactic mid-plane within a photometric distance of 130 pc. This assumption is borne out by comparison of the NGP and SGP luminosity functions (Fig. 20, but see Section 10.4).

In some models we allow for a linear effective gradient in mean abundance, $\overline{[{\rm Fe/H}]}(z)$ with z (writing $\delta[{\rm Fe/H}] = \overline{[{\rm Fe/H}]}$ in equation 7), because the calibration of our mass–M_V and colour–magnitude relations is based on stars close to the Galactic mid-plane which may, on average, be somewhat more metal-rich than the stars at a distance of 100–200 pc.

From the combined absolute magnitudes we obtain the apparent V- and I-band magnitudes for the N systems, perturb these independently by a Gaussian photometric measurement error of dispersion 0.06 mag, which is the photometric accuracy quoted by Stobie & Ishida (1987), and obtain the $V-I$ colour. We also compute the absolute visual magnitude, $M_{V,\rm p}$, from equation (6) for each system, and from this magnitude and the apparent V-band magnitude derive the photometric distance, $d_{\rm p}$, as in KTG2. We use equation (6) here rather than the adopted corrected relation (Table 6) because we need to compare our model with the data of SIP, who based their photometric parallaxes on their own relation. It is straightforward to apply the selection criteria for V, I and $d_{\rm p}$ presented in Section 4.1 to generate a simulated SIP data set. By sorting the $M_{V,\rm p}$ values for systems

within a photometric distance of 130 pc into 1 mag wide bins, we find the raw system luminosity function, $\psi(M_{V,\mathrm{p}})$, which is not corrected for Malmquist effects, nor for an exponential Galactic disc.

5.2 The immediate solar neighbourhood

We use the absolute V-band magnitudes of all individual stars generated above to simulate the stellar sample found within 5.2 pc of the Sun. We generate distances, $d_{\mathrm{trig}} \leq 6$ pc, to allow for selection effects, but consider only those stars which have an apparent parallax less than or equal to 0.1923 arcsec, which corresponds to 5.2 pc. We allow for the effects discussed in Section 3, including the parallax uncertainties, and obtain the absolute V-band magnitude, M_V^*, for each star from the apparent magnitude and the perturbed parallax value. We sort the M_V^* for those stars which have associated true distances within 130 pc, remembering that each star has also associated with it a distance as generated in Section 5.1, into 1 mag wide bins to find the single-star luminosity function $\psi(M_V^*)$.

5.3 The expected number of stars within the immediate solar neighbourhood and the normalization of the mass function

Counting all known stars within 5.2 pc and with declination $\delta > -20°$ (a volume of 395.2 pc^3), we obtain $N_{5.2} = 33$ stars in the magnitude range $7.5 < M_V \leq 15.5$ (Table B2 in Appendix B). To compare this number with that calculated from our model, we consider all single stars generated out to the maximum distance of 300 pc, remembering that each star has associated with it one distance as generated in Section 5.1 as well as another generated as in Section 5.2. We count only those which satisfy $7.5 < M_V^* \leq 15.5$, and refer to this number as n^*. The expected number of stars in 395.2 pc^3 is

$$N_{\mathrm{exp}} = \frac{N_{\mathrm{emp}}}{N_{\mathrm{mo}}} \frac{395.2}{\epsilon(300\ \mathrm{pc})\, V_{\mathrm{cone}}(300\ \mathrm{pc})} n^* = N_{\mathrm{emp}} k, \qquad (11)$$

where we define k for later use,

$$V_{\mathrm{cone}}(H) = (1/3)\Omega H^3$$

is the volume of a cone with height $H = 300$ pc and subtending a solid angle $\Omega = 18.88\ \mathrm{deg}^2 = 5.752 \times 10^{-3}$ sr, and

$$\epsilon(H) = (3/H^3) \int_0^H z^2\, \mathrm{e}^{-z/h}\, \mathrm{d}z \leq 1$$

is the correction factor for the assumed exponential disc. Within the colour range $2.1 < V-I \leq 3.258$, the SIP data are complete to a photometric distance of 130 pc, the number of systems within this (colour, photometric distance) space is $N_{\mathrm{emp}} = 143$, and N_{mo} is the equivalent number obtained from our model. We use $V-I = 2.1$ as a bound instead of the observational bound of $V-I = 1.5$, because initial simulations demonstrated that our model does not lead to the observed bump in the cumulative $V-I$ distribution between $V-I = 1.5$ and 2.1 (Section 7.5 and Fig. 19). This bump is not consistent with standard models of the Galaxy. It occurs in the colour–magnitude range in which disc giants may contribute, but its nature remains uncertain. The ratio $N_{\mathrm{emp}}/N_{\mathrm{mo}}$ thus 'scales down' our model density $(n^*/\varepsilon V_{\mathrm{cone}})$ to the densities prevalent in the Galactic disc.

The normalization, n', for the system luminosity function, $\psi(M_{V,\mathrm{p}})$, is obtained from

$$n' = \frac{N_{\mathrm{emp}}}{N_{\mathrm{mo}}} \frac{1}{V_{\mathrm{cone}}(130\ \mathrm{pc})}, \qquad (12)$$

where we do not include $\epsilon(H)$ because the luminosity function with which we want to compare our models is not corrected for the exponential Galactic disc. We emphasize here that we implement a *photometric* distance limit of 130 pc and use the volume of a cone with height 130 pc to derive the normalization constant n' because we compare our models with luminosity functions that are not corrected for Malmquist effects. Multiplying the number of systems in each magnitude bin by n', we derive the apparent system space densities, $\psi(M_{V,\mathrm{p}})$. The number $n'/\epsilon(130\ \mathrm{pc})$ is the correct normalization for the single-star luminosity function, $\psi(M_V^*)$, in the Galactic mid-plane if $N_{\mathrm{exp}} = 33$. The normalization constant, n, for the stellar mass function in equation (1) in the Galactic mid-plane is given by $\int_{0.45\ \mathrm{M}_\odot}^{0.89\ \mathrm{M}_\odot} \xi(m)\, \mathrm{d}m = 759$, which is the number of stars within a complete sphere with radius 20 pc in the solar neighbourhood in the magnitude range $5.5 < M_V < 10.5$ (WJK).

6 STATISTICAL TESTS

It is never easy to devise the perfect test of whether observations agree with the theory. Unlike in KTG2, where we performed χ^2 tests to compare models with the luminosity functions corrected for cosmic scatter by SIP, we prefer to use the Kolmogorov–Smirnov (KS) test (see, for example, Press et al. 1986) to compare our models with the unbinned observational data which are not corrected for Malmquist effects. By using the raw data, as much information as possible is retained, and we can model all the effects we discuss in Section 3. We emphasize this point because SIP have shown that Malmquist corrections applied in the past to star-count data were not complete, and especially in view of the fact that the systematic effects of binaries, which can be the dominant contribution to cosmic scatter (Section 3.4), have never been taken into account. Furthermore, it is important to keep in mind, when studying the shape of the luminosity function at the faint end, that the photometric calibration becomes uncertain and that the distance completeness limits decrease rapidly with increasing magnitude (equation 9). Together with the changing density distribution with distance which we discuss in Section 10.4 below, this latter problem may lead to wrong estimates of stellar space densities at the faintest magnitudes.

We perform a KS test on the $V-I$ colours, which is equivalent to a KS test on absolute magnitudes and therefore constrains the mass function for the SIP stars. To perform the KS test we generate a model following the procedure outlined in Section 5.1, yielding a cumulative $V-I$ colour

distribution satisfying $V-I \geq 2.1$ (see Section 7.5) which is then compared with the SIP colour distribution. The significance value, P_{V-I}, of the KS test is the probability of obtaining a D as large as or larger than observed if the data are assumed to be drawn from the model distribution, where D is defined as the maximum value of the absolute difference between two cumulative distribution functions. We also construct a cumulative model distribution from the data within a distance of 5.2 pc as a function of absolute visual magnitude satisfying $7.54 \leq M_V^* \leq 16.0$. The bright limit of this interval is defined by the empirical sample (Table B2 in Appendix B), but both limits are convenient, although somewhat arbitrary. The model is compared with the empirical cumulative distribution constructed in the same interval using a KS test. We refer to the significance value of this KS test as P_{M_V}.

With these two KS tests, we have no means of testing the overall normalization and are again just comparing shapes, as was done by KTG2. To test the normalization, we normalize the theoretical colour sample to the SIP data and then predict the total number of stars, $N_{\rm exp}$, that should be in our nearby sample, as described in Section 5.3. The significance of the difference between this and the actual observed number, $N_{5.2} = 33$, can easily be assessed and is equivalent to a χ^2 test with only one data bin,

$$\chi^2 = (N_{5.2} - N_{\rm exp})^2 / (k^2 N_{\rm emp} + N_{5.2}),$$

where the Poisson uncertainties, $k\sqrt{N_{\rm emp}}$ and $\sqrt{N_{5.2}}$, are added in quadrature. The significance value, $P_\#$, of the χ^2 test is simply the probability of obtaining a χ^2 value as large as or larger than the observed value if the data are assumed to be drawn from the model distribution.

Summarizing, we have the three criteria P_{V-I}, P_{M_V} and $P_\#$ to decide with what confidence the SIP and 5.2-pc data are drawn from our model which is specified by the three parameters α_1, h and f. The criteria $P_\#$ and P_{M_V} are not correlated with P_{V-I} because the data sets are independent. We expect P_{M_V} and P_{V-I} show little or no dependence on h because these two criteria test primarily for the distribution of stars by mass. By comparing their behaviour as a function of f, we can test for the binary fraction. The criterion $P_\#$, on the other hand, is expected to be sensitive to all three parameters, as it tests for the relative number of stars in both samples. Our simulations show that $P_\#$ varies with α_1 and h for $f < 0.4$, and we would need to use the joint probability $P_{V-I} \times P_\#$ to constrain α_1 and h simultaneously. For larger values of the binary fraction f, $P_\#$ becomes insensitive to α_1 because a large proportion of the generated low-mass stars are hidden in bright systems, and we can consider P_{V-I} and $P_\#$ separately.

The simulations which we discuss in greater detail in the following section lead to a grid of $P_{V-I,ijk}$, $P_{M_V,ijk}$ and $P_{\#,ijk}$ values at each point in (α_{1i}, h_j, f_k)-space for which a model is generated. Given the insensitivity of P_{V-I} and P_{M_V} to h, we compute the mean probabilities, from here on denoted by P_{V-I} and P_{M_V}, by projecting the grid on to the h-axis for any given f_k. Similarly, we compute the mean probability, $P_\#$, by summing $P_{\#,ijk}$ over all i for $f_k \geq 0.4$. By collapsing the grid on to the irrelevant parameter, we are better able to demonstrate the solutions than by plotting probability contours.

7 SENSITIVITY OF THE SOLUTIONS TO CHANGES OF THE COLOUR–MAGNITUDE RELATION AND TO THE PROPORTION OF BINARIES

7.1 The colour–magnitude relation

In Section 3.6 we have shown that the colour–magnitude relation used by SIP to derive photometric distances should be corrected for systematic effects. Table 6 lists relations corrected for various values of the effective fraction, $f_{\rm trig}$, of contaminating binaries among the trigonometric parallax data used by SIP to derive equation (6). We now investigate the dependence of our solutions for the mass-function power-law index α_1 and the Galactic disc scaleheight h on the adopted colour–magnitude relation.

We proceed with the Monte Carlo simulation discussed in Section 5. We scan α_1, h space in steps of 0.1 in α_1 and 20 pc in h for various colour–magnitude relations assuming, for the time being, that $f = 0.75$. At each point, we generate a model apparent magnitude sample and a model solar neighbourhood sample, computing the significance values $P_{V-I,ij}$, $P_{M_V,ij}$ and $P_{\#,ij}$ (see Section 6).

From the $N = 100\,000$ systems (i.e. 175 000 single stars) we generate at each point, we retain $\approx 10^5$ single stars in the cumulative M_V^* distribution and $\approx 10^{4.1}$–$10^{3.8}$ systems in the cumulative $V-I$ distribution, corresponding to $h = 140$–720 pc. This change in sample size with h comes about because for small h most of the systems are generated with small distances and will consequently be retained in a 130-pc distance-limited sample.

In Fig. 12 we show P_{V-I} as a function of α_1 and $P_\#$ as a function of h for two different colour–magnitude relations taken from Table 6 (model 'c'; the results for model 'l' are very similar). Panels A and D demonstrate the case where the colour–magnitude relation is not contaminated by binaries, i.e. $f_{\rm trig} = 0$, whereas panels B and E assume $f_{\rm trig} = 0.4$. Panel C shows, for comparison to panels A and B, P_{M_V} as a function of α_1. From Fig. 12 it becomes apparent that the solution for maxima in P_{V-I} and $P_\#$ is very sensitive to the adopted colour–magnitude relation, and in Table 8 we list the solutions for additional values of $f_{\rm trig}$. Using the SIP relation instead of a corrected colour–magnitude relation, we obtain a solution virtually identical to the case $f_{\rm trig} = 0$ in Table 8. However, as $f_{\rm trig}$ increases we obtain solutions with increasing α_1 and increasing h. We note that even for small $f_{\rm trig}$ the disagreement between $P_{V-I}(\alpha_1)$ and $P_{M_V}(\alpha_1)$ is not significant enough to pose major concern that the mass function relevant for the solar neighbourhood is different from the mass function relevant for the SIP data, and we will return to this question in Section 7.5.

7.2 The Galactic disc scaleheight

We cannot decide which of the models in Table 8 represents the best description of the SIP and solar neighbourhood data, because we have no direct way of constraining the colour–magnitude relation. However, we note that our solutions for the scaleheight show a strong dependence on the colour–magnitude relation and we can use this to constrain $f_{\rm trig}$ by considering the results of independent star-count work aimed at deriving h. Surveys made in order to

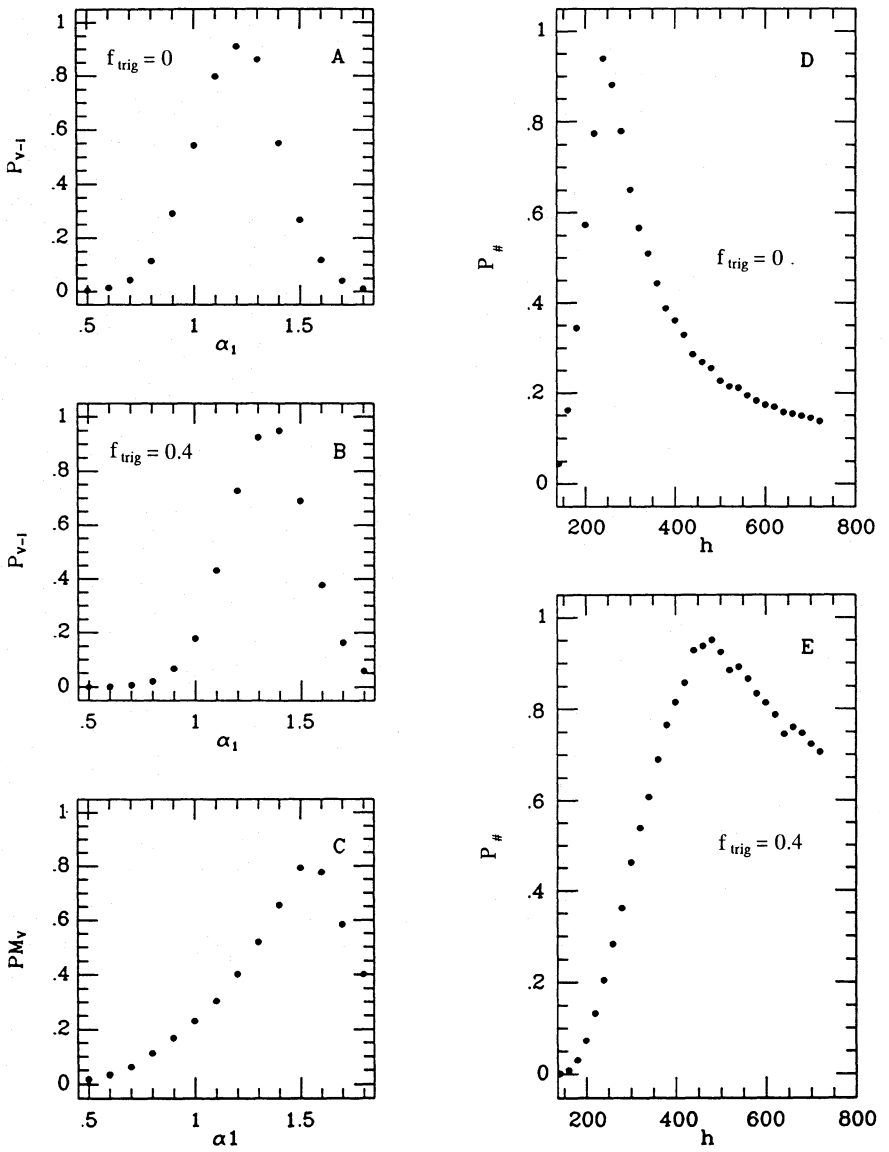

Figure 12. The sensitivity of the solutions to the adopted colour–magnitude relation (Section 7.1). The results for two cases are shown: $f_{\rm trig}=0$ (panels A and D) and $f_{\rm trig}=0.4$ (panels B and E). Panels A and B show the confidence, $P_{V-I}(\alpha_1)$, that a particular model represented by α_1 is a valid description of the NGP star-count data (SIP). For comparison we show in panel C the confidence, $P_{M_V}(\alpha_1)$, that a particular model is a valid representation of the data from the immediate solar neighbourhood. Panels D and E show the confidence, $P_\#(h)$, that a particular model represented by h is a valid description of the NGP data given the constraint of the number of stars in the immediate solar neighbourhood.

Table 8. The dependence of the solution for maxima in $P_{V-I}(\alpha_1)$ and $P_\#(h)$ on the corrected colour–magnitude relations listed in Table 6 (model 'c').

$f_{\rm trig}$	α_1	P_{V-I}	h(pc)	$P_\#$
0.0	1.22	0.92	240	0.94
0.1	1.25	0.96	270	0.95
0.2	1.30	0.96	320	0.96
0.4	1.35	0.97	460	0.95
0.6	1.45	0.93	760	0.96
1.0	1.80	0.97	>1080	>0.2

study Galactic disc structure usually use bright tracer stars (e.g. K dwarfs) for which the colour–magnitude relation is not affected to such a large extent by unresolved binaries (Fig. 10). We can hope to use the results of such surveys to identify a 'most plausible' colour–magnitude relation, as we show below.

Although not gravitationally self-consistent, an exponential distribution of stars with distance from the Galactic mid-plane proves to be a very useful and accurate approximation (for example, consult fig. 5 of Kuijken & Gilmore 1989b). The scaleheight of such an exponential distribution is roughly constant at ≈ 90 pc for stars with $M_V<2$, and increases to a value of ≈ 300 pc in the magnitude interval $2<M_V<5$. The disc scaleheight for fainter main-sequence stars appears to be constant, and we shall return to this point in Section 10. The behaviour of the thickness of the Galactic disc with stellar spectral type is understood in terms of kinematic heating of a stellar population coupled with a strong dependence of stellar lifetime on M_V. Stars are born with a small disc scaleheight, and by encounters with large

complexes (molecular clouds, clusters etc.) diffuse outwards from the mid-plane until relative velocities are too large for further significant gravitational interactions. This scenario is important for the interpretation of the data discussed in Section 10.

Recent investigations of the structure of the Galaxy (e.g. Kuijken & Gilmore 1989a; Fenkart & del Rio 1991) show that the distribution of lower main-sequence stars perpendicular to the galactic mid-plane within a distance range of 200–600 pc can be represented by a single exponential with scaleheight $h = 276$–301 pc. For smaller distances, the derived scaleheight becomes uncertain because the star-count data are sparse. We note that the solutions presented in Table 8 and based on the NGP star-count data (SIP) within a photometric distance of 130 pc agree with these values if we use a colour–magnitude relation corrected for $f_{\rm trig} < 0.1$. This is also consistent with the constraints posed by the data of Bessell (1991), as shown in Fig. 10. Before we reach firm conclusions about which colour–magnitude relation gives most consistent results, we should remember that the above scaleheights were derived from number counts corrected for Malmquist bias. SIP have shown that substantial disagreement exists between various authors as to how this correction is to be applied. We therefore carefully reconsider the derivation of a distance distribution from photometric data.

In accordance with the philosophy presented in Section 6, we prefer to study the raw distribution of stars with distance perpendicular to the Galactic mid-plane, and calculate the disc scaleheight which is deduced from these data without applying Malmquist corrections. We refer to this apparent scaleheight as $h_{\rm app}$ and, if $h_{\rm true}$ denotes the true scaleheight, then we expect $h_{\rm app} < h_{\rm true}$ because of the on-average 'one-sided' effect of the cosmic scatter on number counts ('stars', on the average, appear closer) and on the truly 'one-sided' bias of binaries, since every system appears closer, thus enhancing the effect due to an age and metallicity dispersion. We expect $h_{\rm app}$ to be a function of the absolute magnitude, or colour, of the tracer stars, because stellar evolution and the metallicity dispersion have unequal effects at different colours (Figs 4 and 6) and because binaries will lead to a progressively larger effect as we go to fainter systems (Fig. 8). We conclude that different corrections need to be applied to the observed number counts of 'stars' depending on which spectral type of 'star' is being dealt with (Table 7). Alternatively, we model the raw data. We shall return to our contemplation of $h_{\rm app}$ being a function of $V-I$ in Section 10.

7.2.1 The apparent disc scaleheight from raw star-count data

In this section we study the raw star-count data in the direction of the SGP and derive the apparent scaleheight.

The star-count data we use here are discussed fully by Kuijken & Gilmore (1989a, hereafter KG). The data were obtained from a photographic survey towards the SGP in the B, V and I bands, with an internal and external error in each magnitude of ≈ 0.04 mag. In Fig. 13 we show the two-colour diagram for these data and note that $B-V = 0.85$ and 1.2 correspond to $V-I \approx 0.93$ and ≈ 1.22, respectively. A follow-up spectroscopic observing programme carried out by KG served to identify the fraction of stars in the colour range $B-V = 0.85$–1.20 which are giants. The data are presented in condensed form in table 2 of KG.

We bin the star-count data with $0.845 \leq B-V \leq 1.195$ in the V bins as given in table 2 of KG, and correct the counts in each V bin for the number of giant contaminators. For example, in the $15.0 \leq V < 15.5$ bin we have 107 stars, of

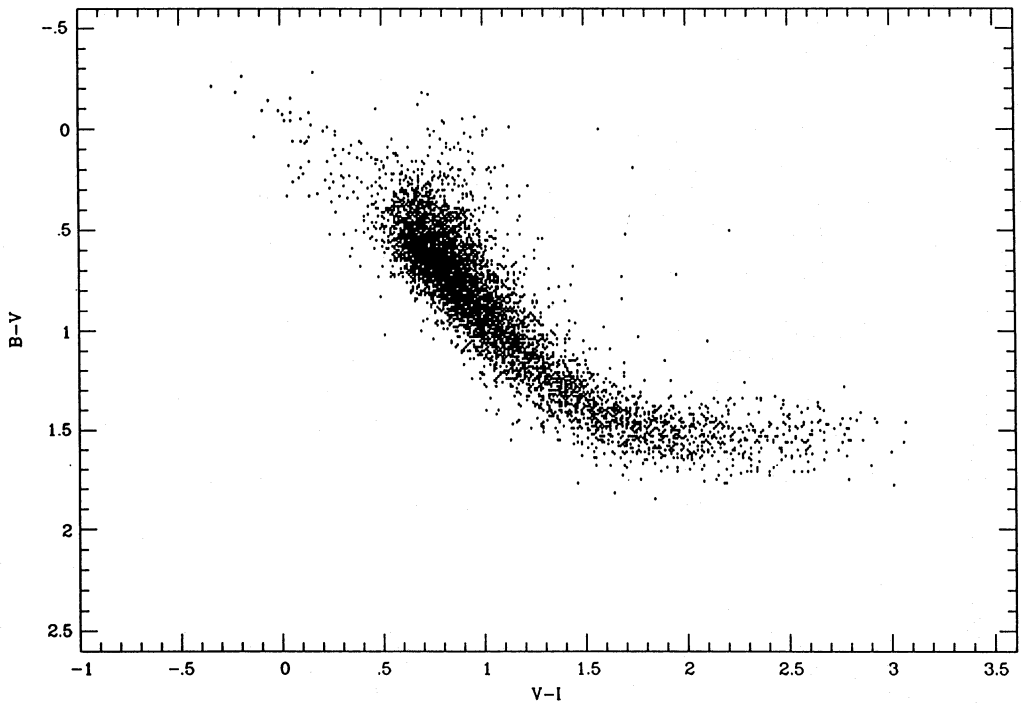

Figure 13. Two-colour diagram of the South Galactic Pole data used in Section 7.2.1 to derive the apparent scaleheight $h^{(1)}_{\rm app}$. The data are discussed fully by Kuijken & Gilmore (1989a).

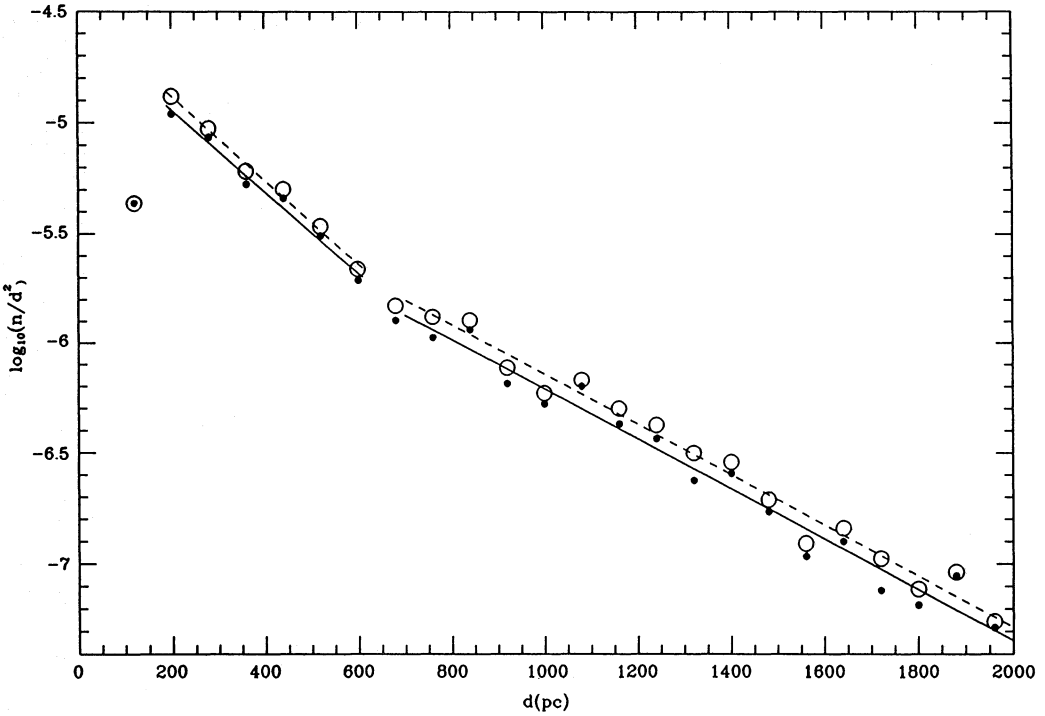

Figure 14. Distribution of stars with $0.93 \leq V-I \leq 1.22$ with distance from the Galactic mid-plane in the direction of the South Galactic Pole, constructed from the data shown in Fig. 13. The distribution is incomplete for distances smaller than ≈ 150 pc. Open circles denote the distribution not corrected for the giant contamination, whereas solid dots represent the corrected distribution. The dashed and solid lines correspond to single exponential laws with apparent scaleheights of 230 and 237 pc, respectively, over the distance range 200 to 600 pc. For distances between 700 and 2000 pc, the respective scaleheights are 381 and 384 pc.

which ≈ 22 per cent are giants. We reduce the number of stars in that bin by 24. We proceed in this way for all the bins in table 2 of KG, and derive a photometric parallax value for every remaining star using an adopted colour–magnitude relation. The photometric distances are binned into 80 pc wide bins and these counts, divided by the square of the centre of each bin, are used to fit an exponential function with scaleheight $h^{(1)}_{\rm app}$. In Fig. 14 we compare the distance distribution obtained by correcting for giants (solid dots) with the distribution obtained if the giant contamination is ignored (open circles), adopting for present purposes the colour–magnitude relation in Table 6 (model 'c') corrected for $f_{\rm trig}=0.1$ to derive space densities. For the two cases shown, we obtain by linear regression in the distance interval 200–600 pc a scaleheight $h^{(1)}_{\rm app}=237\pm14$ pc for the corrected distribution, and $h^{(1)}_{\rm app}=230\pm11$ pc for the uncorrected distribution. The quoted uncertainties are probable errors. The corrected and uncorrected distributions do not show a significant difference.

7.2.2 *Simulations of star-count data*

In this section we show that the traditional Malmquist corrections applied to star-count data for stars with $0.9<V-I<1.2$ remove the biases sufficiently that the disc scaleheight estimates discussed in Section 7.2 can be taken to be good approximations to the true distribution of stars.

We generate $N=4\times10^6$ systems within a distance of 300 pc exactly as in Section 5.1, with the one difference that we use the colour–magnitude relation corrected for $f_{\rm trig}=0.1$ (Table 6, model 'c') both for transformation from the V to the I band and for photometric parallax, and we adopt 0.04 mag as our Gaussian measurement uncertainty. We assume $\alpha_1=1.2$ and $f=0.6$. We bin the true distances, z, generated from equation (10) with an assumed scaleheight $h_{\rm ass}=275$ pc for all data into 10 pc wide bins, and refer to this as our true distribution. We also bin the photometric distance, $d_{\rm p}$, for 'stars' with $0.93\leq V-I\leq1.22$.

In Fig. 15 we plot the distance distributions. We note that the apparent distribution decays beyond a photometric distance of about 200 pc, and this is the reason we choose 300 pc as the maximum distance in our simulations. Over the distance range 30–170 pc, we find an apparent scaleheight $h^{(2)}_{\rm app}=230\pm8$ pc.

The apparent scaleheight, $h^{(1)}_{\rm app}\approx237$ pc, which we deduce from the SGP star-count data (KG) in Section 7.2.1 is in good agreement with $h^{(2)}_{\rm app}$. Our assumed value for $h_{\rm ass}$ agrees with the single scaleheight of 276 pc representing the double-exponential fit by KG to the SGP data, and we conclude that the Malmquist corrections applied by KG correctly allow for cosmic scatter.

7.2.3 *Summary and discussion*

In Section 7.2 we have seen that traditional star-count analysis towards the SGP (KG) yields, as approximations to the distribution of stars perpendicular to the Galactic disc, single-exponential density distributions. These have a scaleheight of $h\approx280$ between 200 and 600 pc from the mid-plane. In Section 7.2.1 we showed that the same high-quality

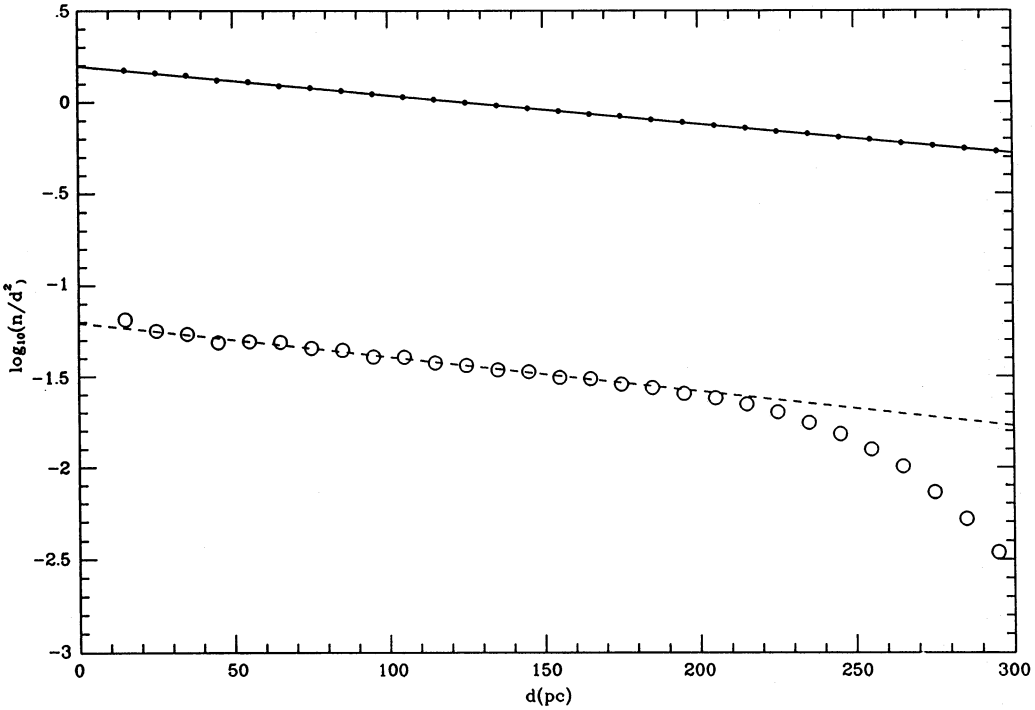

Figure 15. Simulated distance distribution assuming that 60 per cent of all 'stars' are unresolved binaries. The adopted density law is given by equation (10) with scaleheight $h_{ass} = 275$ pc. Binning the distances z of all individual stars into 10 pc wide bins, we obtain the true distance distribution shown by solid dots. Linear regression on this distribution recovers the scaleheight ($h = 274.4 \pm 0.8$ pc), and is shown by the solid line. Binning the apparent distances d_p for 'stars' with $0.93 \le V-I \le 1.22$, we obtain the distribution shown by open circles. Linear regression over the distance interval $30 \le d_p \le 170$ pc on that distribution (dashed line) yields $h^{(2)}_{app} = 230 \pm 8$ pc. The apparent distance distribution decays at $d_p > 200$ pc because we do not generate stars at distances larger than 300 pc.

star-count data for stars with $M_V \approx 6.4$ yield an apparent distribution towards the SGP which can be represented by an exponential with an apparent scaleheight $h_{app} \approx 237 \pm 14$ pc. Our simulations in Section 7.2.2 demonstrate that a model assuming an underlying true exponential scaleheight of 275 pc yields $h_{app} \approx 230$ pc, thus demonstrating that the Malmquist corrections applied by KG yield approximately correct results.

Our simulations of star-count data within a photometric distance of 130 pc towards the NGP yield solutions for the scaleheight that are larger than 240 pc, depending on which colour–magnitude relation is used (Section 7.1). This analysis of the density distribution of stars perpendicular to the disc of the Galaxy is much more sensitive to the colour–magnitude relation and to the Malmquist corrections than are the results derived using stars with $M_V \approx 6.4$, because our analysis is mostly sensitive to stars with $M_V \approx 12$ where the peak in the luminosity function lies. At this absolute magnitude, the systematic biases in the cosmic scatter are quite large. We find that a colour–magnitude relation corrected for an effective fraction of binaries of $f_{trig} = 0.1$ (Section 3.6) yields a solution for the scaleheight of $h \approx 270$ pc (Section 7.1), in agreement with the SGP data over a distance range $z = 200$–600 pc.

However, we point out that the stellar number density within a distance range of 0–200 pc may be characterizable by smaller scaleheights (Section 10.4). A future paper will report the sensitivity of the results presented in Table 8 to the adopted mass–M_V relation. Preliminary results indicate that 'fine tuning' of the mass–M_V relation leads to solutions for h that are consistent with $h_{app} \approx 180$ pc, given the NGP star-count data used here and the colour–magnitude relation corrected for $f_{trig} < 0.2$ (Table 6). This may solve the apparent discrepancy between the SGP and NGP star-count data, identified in Section 10.4.

7.3 The proportion of binaries

In this section we study the sensitivity of the solutions to changes in the global proportion of binaries among 'stars'.

We simulate model samples as in Section 7.1, adopting the colour–magnitude relation corrected for $f_{trig} = 0.1$ for the corresponding metallicity model (Table 6). However, here we scan α_1 in steps of 0.05 and h in steps of 10 pc for better resolution. In Fig. 16 we show $P_{V-I}(\alpha_1)$ for four cases of the binary proportion, namely $f = 0.2$, 0.4, 0.7 and 1.0. Table 9 lists the adopted solutions that maximize P_{V-I}. The case $f = 0$ has been included for interest only. It is in contradiction with our adopted colour–magnitude relation, as well as our knowledge that a significant proportion of 'stars' are unresolved systems. The effects of unresolved binary stars become most prominent at the hydrogen-burning mass limit (Fig. 8), and our simulations here imply that the solutions are not very sensitive to variations in f. Unfortunately, the SIP NGP sample contains few 'stars' with $V-I > 3.3$. From Fig. 16 and the numbers in Table 9, we infer that we obtain marginally better agreement between P_{V-I} and P_{M_V} if $f = 1$, which is the same as the conclusion drawn by KTG2. However, as we show in Section 7.4, introduction of an effec-

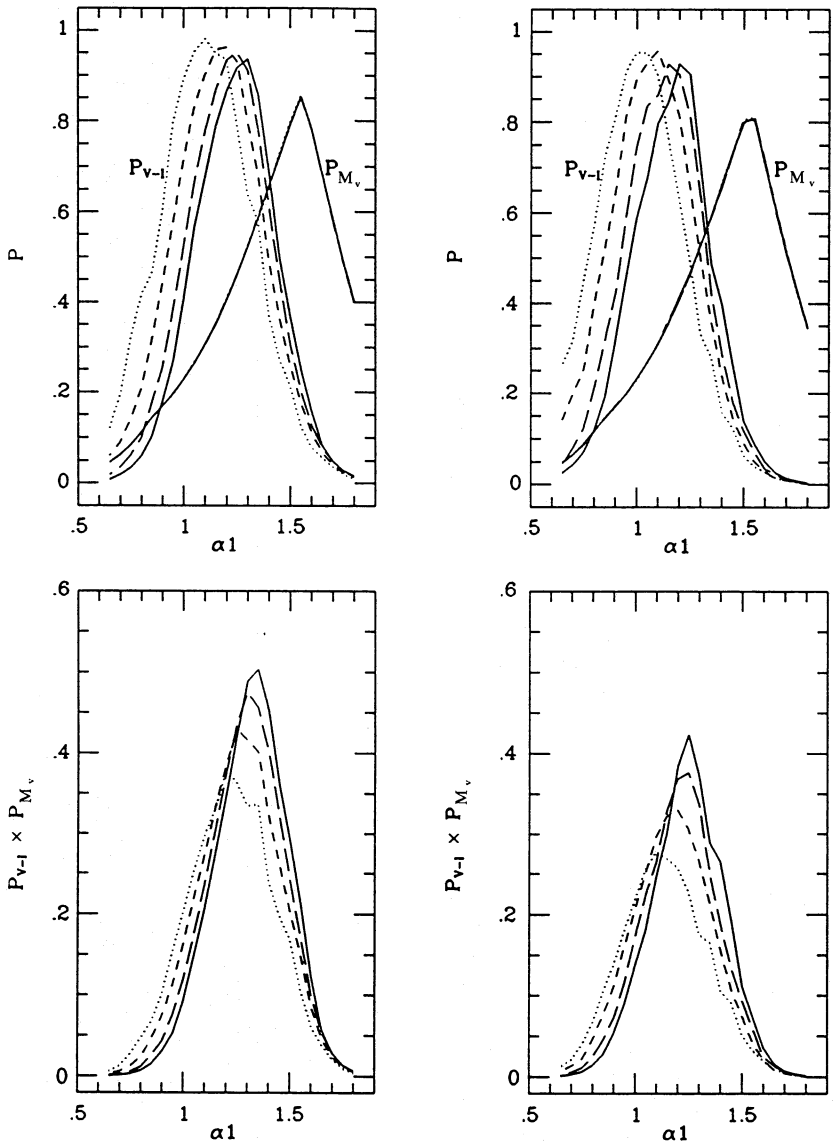

Figure 16. The sensitivity of the solutions to changes in the global proportion of binaries among 'stars' (Section 7.3). The top panels show the confidence that our model, represented by the mass-function power-law index α_1, is a valid description of the star-count data towards the NGP $[P_{V-I}(\alpha_1)]$ and of the distribution of stars within the immediate solar neighbourhood $[P_{M_V}(\alpha_1)]$. The results for four different values of the proportion, f, among apparently single stars of unresolved binaries consisting of two hydrogen-burning stars are shown for both metallicity models (left panels: model 'c'; right panels: model 'l'): $f=0.2$ (dotted curve), $f=0.4$ (short-dashed curve), $f=0.7$ (long-dashed curve) and $f=1$ (solid curve). The bottom panels show the joint confidence $P_{V-I}+P_{M_V}(\alpha_1)$. The joint solutions improve as the fraction of binaries increases.

tive metallicity gradient has an effect very similar to that of an increase in f, and we cannot ascertain that $f=1$ is a preferred value.

Variation of f has little effect on $P_{\#}$, and we find for $0.2<f\leq 1$ that $h\approx 270$ pc. As an example we show, in Fig. 17, $P_{\#}(h)$ for $f=0.7$. The values at which $P_{\#}(h)$ is maximized are given in Table 9. We remember that the $P_{\#}$ contours are not parallel to the α_1-axis for $f<0.4$ (Section 6), and for $f=0$ and 0.2 we need to consider the joint probability $P_{V-I}\times P_{\#}$ to identify the most likely model.

7.4 Metallicity gradient

In our simulations we have so far assumed no change of metallicity with distance from the Galactic mid-plane. However, we may expect stars at a distance of about 100 pc to have a somewhat lower average metal abundance than the stars used to calibrate our mass–M_V and colour–magnitude relations, which are likely to include thin-disc stars. We assume a linear change of metallicity with distance (Section 5.1), and proceed as in Section 7.3 for three values of the effective gradient: 0, −0.05 and −0.1 dex per 100 pc, assuming $f=0.7$. We emphasize that, although the data on the distribution of metallicity with z (see fig. 5 of Gilmore & Wyse 1985) do not show a significant change of metal abundance within a distance of about 800 pc from the mid-plane, a change of approximately −0.1 dex within about 100 pc cannot be excluded.

The results are summarized in Fig. 18, and we see that as the gradient steepens the maxima in P_{V-I} and $P_{\#}$ shift to

Table 9. Adopted solutions for P_{V-I} and $P_{\#}$ as a function of f. In all cases P_{M_V} is maximized at $\alpha_1 = 1.55$ with $P_{M_V} \approx 0.85$.

Model 'c'

f	α_1	P_{V-I}	h(pc)	P^*
0.0	1.00	0.98	250	0.92
0.2	1.10	0.98	280	0.93
0.4	1.19	0.96	275	0.91
0.7	1.24	0.95	270	0.94
1.0	1.30	0.94	270	0.95

Model 'l'

f	α_1	P_{V-I}	h(pc)	P^*
0.2	1.03	0.96	270	0.92
0.4	1.09	0.96	270	0.91
0.7	1.16	0.94	270	0.96
1.0	1.21	0.93	270	0.96

Note: $P^* = P_{V-I} \times P_{\#}$ for $f \leq 0.2$; and $P^* = P_{\#}$ for $f \geq 0.4$.

larger values of α_1 and h, respectively. By increasing the metallicity difference between the stars near the mid-plane and those at a distance of about 100 pc, we can thus improve the joint confidence that our model is a valid representation of both the immediate solar neighbourhood stars and the NGP star-count data (SIP).

7.5 Discussion

Our simulations in Section 7.3 of only the NGP star-count data (SIP) demonstrate that the solution for α_1 (≈ 1.2) is in good agreement with the value we derived in Section 2 for no metallicity gradient. We have also found that confidence is maximized for models with a disc scaleheight of ≈ 270 pc. Values less than ≈ 150 pc can be excluded with 95 per cent confidence, but the constraint on large h is much weaker because the star-count data are restricted to a photometric distance of 130 pc only. These results are essentially based on stars with $M_V \approx 12$, where the peak in the luminosity function lies.

In the left-hand panel of Fig. 19 we plot the system cumulative distribution function for the solution with $f = 0.7$ and $\alpha_1 = 1.24$, and in the right-hand panel we plot the corresponding cumulative single-star distribution function. Assuming the model to be true then the KS test yields a probability of observing a distribution such as that given by the SIP $V-I$ data of 95 per cent, and a probability of observing a distribution in M_V such as given by the stars within 5.2 pc of 44 per cent. The model cumulative distribution for the immediate solar neighbourhood is thus not in very good agreement with the data, but the agreement is not sufficiently bad to discard the model. The excess of systems with $1.5 < V-I < 2$ in the observed apparent magnitude sample visible in the left-hand panel may indicate giant star contamination, and is the reason why, in Sections 5.3 and 6, we restrict the KS test to $V-I \geq 2.1$. Standard models of the Galaxy, however, provide no explanation for this bump.

In Fig. 20 we show the raw luminosity functions determined towards both Galactic poles. The agreement between the two independent studies and the growing discrepancy with the nearby luminosity function with increasing magnitude are apparent (see also DLH). Our solutions (Table 9) are

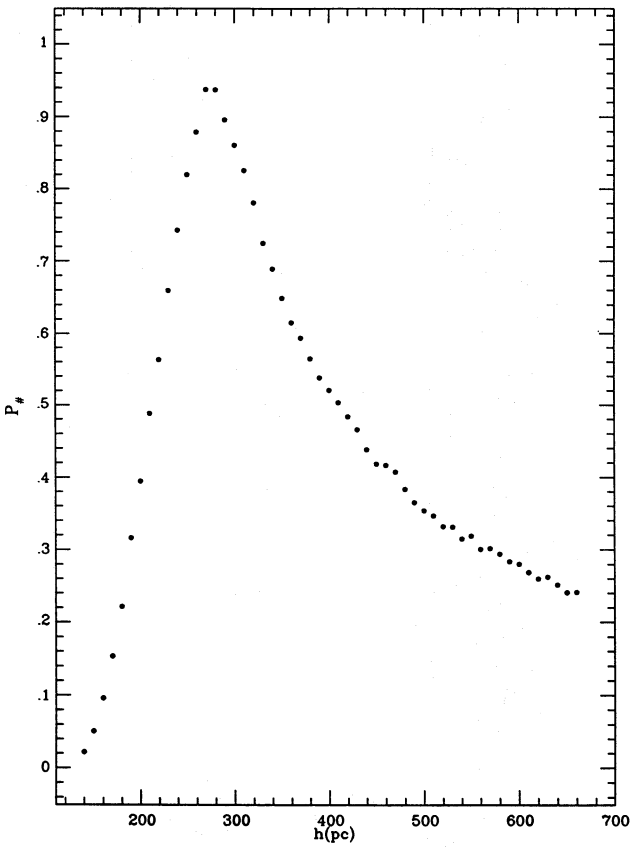

Figure 17. The variation with model disc scaleheight h of the confidence value $P_{\#}$ that any particular model is a valid representation of the NGP data, given the number of stars seen in the immediate neighbourhood of the Sun. We assume $f = 0.7$, but the results for other values of $f > 0.4$ are very similar. The maximum in $P_{\#}$ of 0.94 lies at $h = 270$ pc. Values for h smaller than 150 pc can be excluded with 95 per cent confidence, but the data do not cover a large enough range in photometric distance to allow a tight constraint on large values of h.

in good agreement with the data, apart from the range $M_V > 13$, where our models of the system luminosity function predict stellar number densities that are somewhat too large. This may be due to systematic bias in the observed luminosity function, because we expect photometric calibration to become increasingly uncertain towards the fainter magnitudes, and we remind the reader that we have used a single Gaussian error distribution to model photometric precision in Section 3.5 when calibrating the colour–magnitude relation. Furthermore, the distance limits of the photographic surveys decrease rapidly with decreasing luminosity (equation 9), and the density distribution of stars towards the NGP may be steeper within small distances from the mid-plane than at larger distances (Section 10.4). It is also possible that we are not using the correct mass–M_V relation at $M_V > 13$ (see also Section 7.2.3). We stress again that the single-star and the system luminosity functions show similar and well-understood structure (a dip at $M_V \approx 7$ and a peak at $M_V \approx 12$), but that the main difference between the two consists of a reduced number of faint 'stars' relative to the number of bright ones in the system luminosity function. We illustrate this by plotting the ratio $\psi(M_{V,\mathrm{p}})/\psi(M_V^*)$ in Fig. 21,

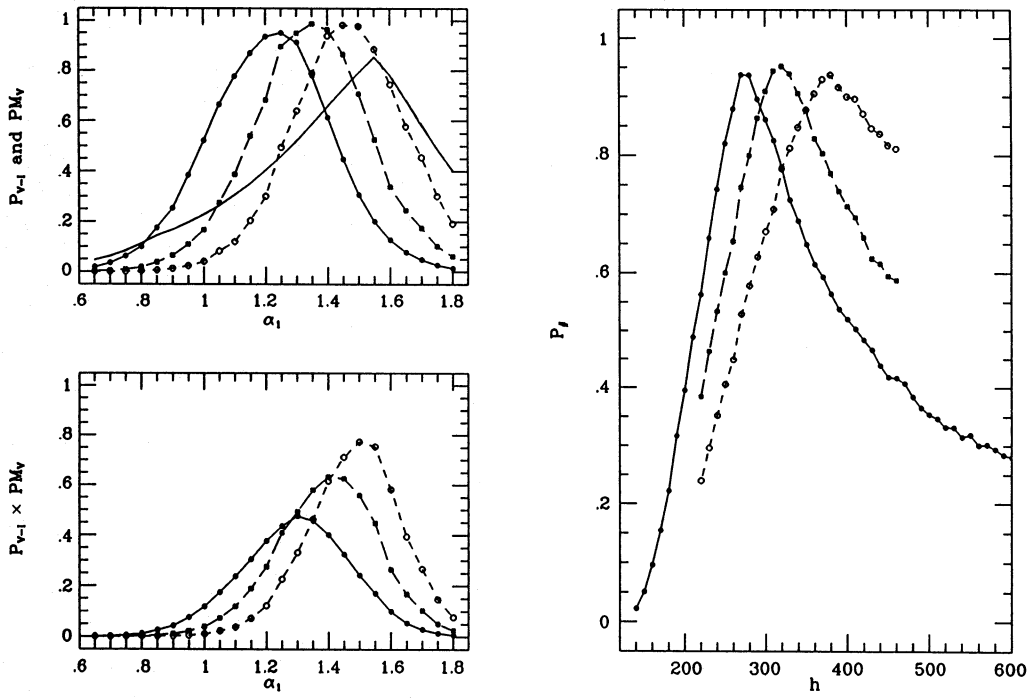

Figure 18. The sensitivity of our simulations to the metallicity gradient (Section 7.4). In the top left-hand panel the symbols connected by lines show the variation of the confidence $P_{V-I}(\alpha_1)$ for different values of the effective gradient: 0 (solid dots connected by solid line), −0.05 (solid dots connected by dashed line) and −0.1 (open circles connected by dashed line) dex in 100 pc. As a comparison, the confidence $P_{M_V}(\alpha_1)$ is shown by the solid line with no symbols superposed. As the metallicity gradient decreases, the maximum in P_{V-I} approaches the maximum in P_{M_V} and the joint probability $P_{V-I} \times P_{M_V}$ shown in the lower left-hand panel increases and shifts to larger values of α_1. The right-hand panel shows the effect of the metallicity gradient on the confidence $P_\#(h)$. As the gradient steepens, the maximum in $P_\#$ shifts to larger values of the disc scaleheight h.

which shows the fairly uniform decline of the system luminosity function, $\psi(M_{V,\mathrm{p}})$, with increasing magnitude until, in the case of $f=1$, it decays to somewhat less than one-third of the number of stars in the single-star luminosity function at $M_V=16$. The structure at $M_V \approx 13$ is a result of the peak being at slightly different positions in the two luminosity functions because they are subject to different Malmquist effects. We also note that the luminosity functions are similar at the bright end. This is a result of our assumption that the component masses are uncorrelated and of the mass function rising continuously towards the minimum mass for hydrogen burning.

Constraints on the binary fraction are weak because the effects of unresolved binaries are most prominent near the hydrogen-burning mass limit. The majority of the NGP star-count data (SIP) are too blue. Nevertheless, we have found that the joint confidence, $P_{V-I} \times P_{M_V}$, which measures the success of our model in providing a valid representation of the parent distribution of the NGP star-count data as well as of the data on stars in the immediate neighbourhood of the Sun, increases with increasing f and is largest if $f=1$ and $\alpha_1=1.35$ (metallicity model 'c') or $\alpha_1=1.25$ (metallicity model 'l') for no effective metallicity gradient.

Considering the immediate solar neighbourhood sample of stars, we have seen that a power-law mass function maximizes our confidence with $P_{M_V} \approx 0.85$ that it is a valid representation of these data if $\alpha_1=1.55$. The constraints on α_1 determined from this sample are weak, though, because of the small number of stars. Decreasing the effective metallicity gradient from zero to −0.05 and −0.1 dex per 100 pc, we obtained, as solutions to the SIP data alone, $\alpha_1 \approx 1.2$, ≈ 1.35 and ≈ 1.45 respectively for $f=0.7$, with unchanged significance, $P_{V-I} \approx 0.95$. A decrease in the metallicity gradient thus has a similar effect to an increase in the binary fraction f, as can be seen by comparing Figs 16 and 18. Indeed, we find that a model which has an effective gradient of −0.08 dex per 100 pc and $f=1$ using a colour–magnitude relation corrected for $f_{\mathrm{trig}}=0.2$ (Table 2, model 'c') maximizes our confidence that it represents both data sets simultaneously with joint confidence $P_{V-I} \times P_{M_V}=0.8$ if $a_1=1.52$. The 95 per cent confidence interval for α_1 is in this case $1.1 \leq \alpha_1 \leq 1.8$. The corresponding scaleheight is $h=420$ pc, but ≈ 300 pc is acceptable with 50 per cent confidence. A plot of the model luminosity functions is very similar to that shown in Fig. 20. We can construct equally good models by choosing other combinations of f, d[Fe/H]/dz and f_{trig}. Currently available constraints on any of these parameters are not good enough to allow preference of any particular model, but we can specify the range of α_1 in which we are 95 per cent confident it is contained. For this purpose we consider the joint confidence $P_{V-I} \times P_{M_V}$, and from Figs 16 and 18 we see that α_1 does not lie outside the 0.05 joint probability interval if $0.70 < \alpha_1 < 1.85$.

8 THE MASS FUNCTION

Adopting the centre of the 95 per cent confidence interval for α_1 (Section 7.5), the mass function (equation 1) becomes

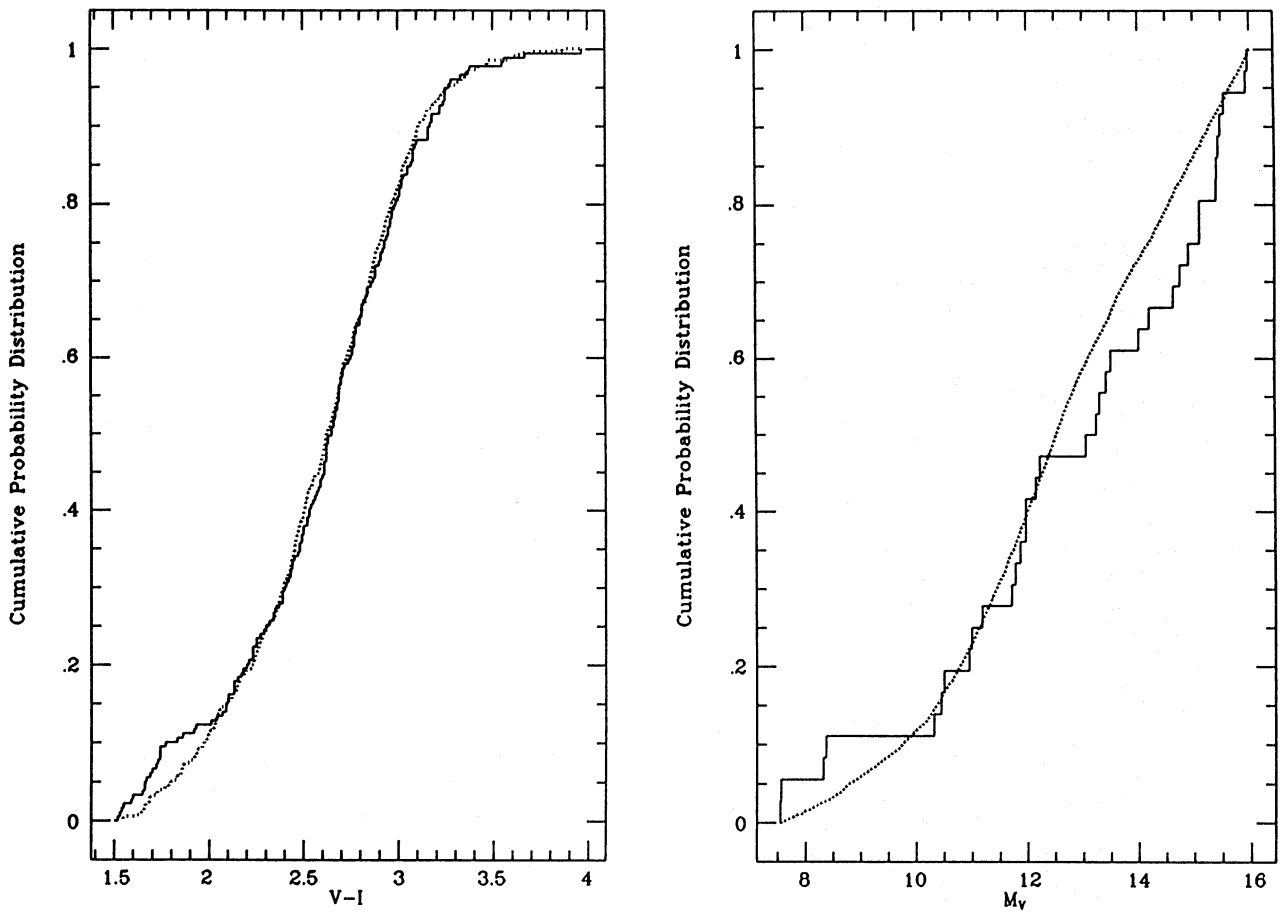

Figure 19. The model cumulative distribution is compared with the observed distribution for the solution of P_{V-I} in Table 9 with $\alpha_1 = 1.24$, $h = 270$ pc and $f = 0.7$. The right-hand panel shows the model cumulative distribution for single stars (dotted curve), where the cumulative distribution based on observed absolute magnitudes (Table B2 in Appendix B) is shown as a solid curve. The left-hand panel shows the cumulative distribution in $V-I$ colour. The best model is shown as the dotted curve, whereas the SIP data yield the solid curve. For illustrative purposes, we plot the distribution for $V-I \geq 1.5$, although our KS testing is confined to $V-I \geq 2.1$. Note the bump in the observed distribution in the range $1.5 < V-I < 2.1$. It may be due to residual giant star contamination of the SIP star-count data.

$$\xi(m) = \begin{cases} 0.035 m^{-1.3} & \text{if } 0.08 \leq m < 0.5, \\ 0.019 m^{-2.2} & \text{if } 0.5 \leq m < 1.0, \\ 0.019 m^{-2.7} & \text{if } 1.0 \leq m < \infty, \end{cases} \quad (13)$$

where m is the stellar mass in solar units. Equation (13) is the initial mass function (IMF), because evolution of low-mass stars is not significant and because we have based our extension of the power-law mass function to higher masses on Scalo's (1986) initial mass function. We plot equation (13) in Fig. 22 and compare it to Scalo's mass function. As already discussed by KTG1, the structure evident in the mass function derived by Scalo reflects the universal structure apparent in the luminosity function, because the mass–M_V relation he adopted ignored the inherent points of inflexion (Fig. 1). There is no necessity for a bimodal shape in our result, and the only structure we require is a flattening at 1 $M_\odot$ and at 0.5 $M_\odot$.

The following mass-generating function (R. Cannon, private communication),

$$M(X) = 0.08 + \frac{\gamma_1 X^{\gamma_2} + \gamma_3 X^{\gamma_4}}{(1-X)^{0.58}}, \quad (14)$$

is a convenient representation of our results, where $\mathrm{d}X/\mathrm{d}M \propto \xi(M)$, M is the mass in solar units, X is uniformly distributed in the interval $[0, 1]$ and the γ-parameters are given in Table 10 for some values of α_1. No masses less than 0.08 $M_\odot$ are generated by this formula.

Concerning the normalization of the mass function we have, for $\alpha_1 = 1.3$, $n = 0.087$ star pc^{-3} $M_\odot^{-1}$ in equation (1), implying that the mass density in stars ever to have formed in the mass range $0.08 \leq m \leq 1$ $M_\odot$ is 0.036 $M_\odot$ pc^{-3}. Extrapolation below 0.08 $M_\odot$ down to zero mass adds 8.5×10^{-3} $M_\odot$ pc^{-3}. These values are based on the number of stars within a complete sphere with radius 20 pc in the solar neighbourhood, being 759 in the magnitude range $5.5 \leq M_V \leq 10.5$ (WJK). The mass in main-sequence stars more massive than the Sun, adopting $\alpha_3 = 4.5$ in equation (1), is 7.6×10^{-3} $M_\odot$ pc^{-3}. If we take into account that the 95 per cent confidence interval for α_1 is 0.70–1.85, and the Poisson uncertainty in the number of stars observed, then we obtain as an estimate for the uncertainty in the normalization of the mass function: $n \approx 0.087 \pm 0.004$ star pc^{-3} $M_\odot^{-1}$. This is likely to be an overestimate of the uncertainty in n because we have been very conservative in considering the uncertainty in α_1. The maximum contribution to the mass

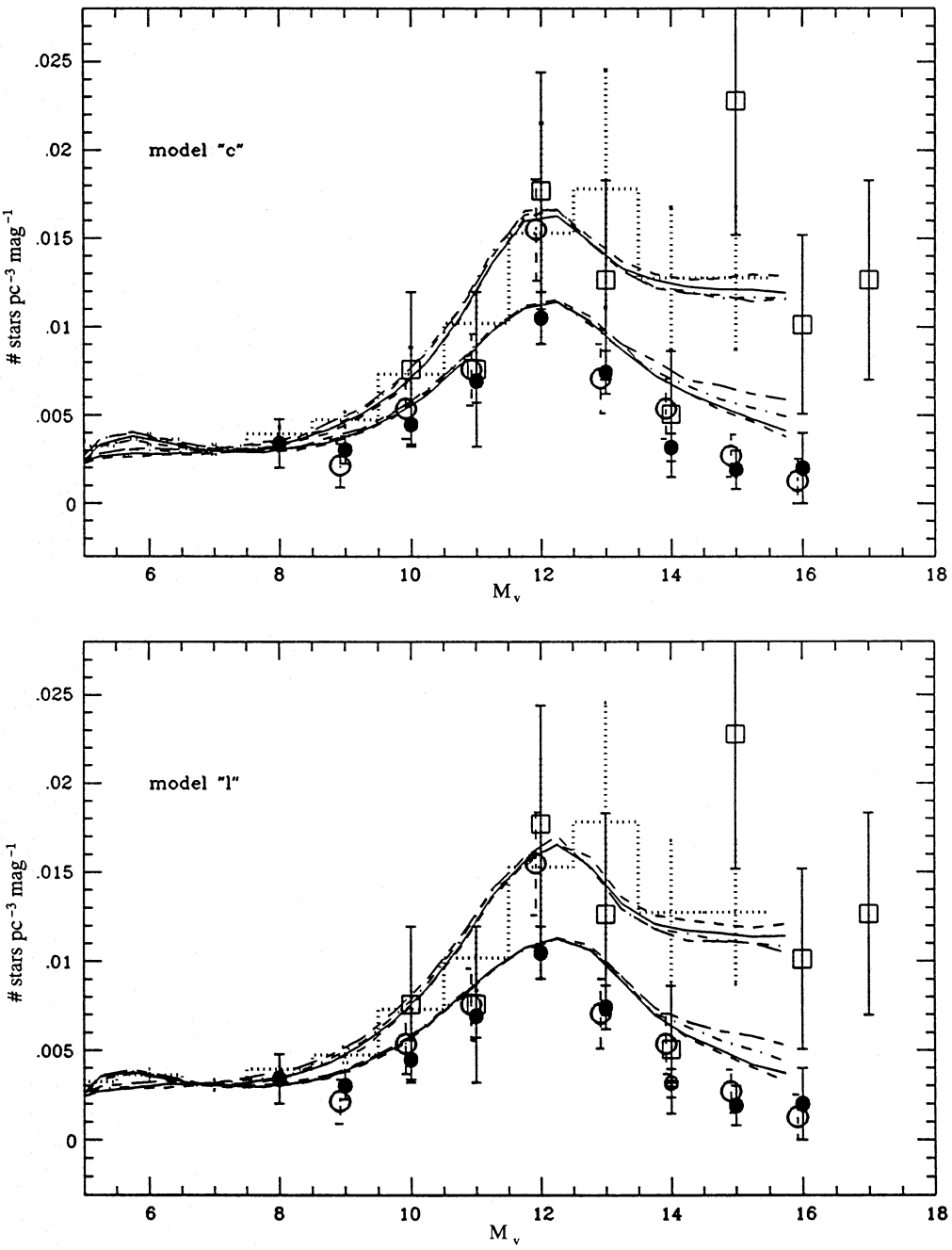

Figure 20. The observed local luminosity function based on data compiled by Wielen et al. (1983) is shown as a dotted histogram. Open squares represent the determination from the 5.2-pc sample (Section 4.2). Two examples of photographically determined luminosity functions towards the SGP and the NGP are shown as open and solid circles, respectively (Reid & Gilmore 1982 and Stobie, Ishida & Peacock 1989, respectively). Malmquist and Galactic disc scaleheight corrections have been removed. The upper curves depict our single-star Galactic field models and the lower curves the system luminosity functions for $f=0.2$ (short–long dashed line), $f=0.4$ (dot–dashed line), $f=0.7$ (solid line) and $f=1.0$ (short-dashed line). Top panel: the solutions in α_1 and h maximizing the confidence in our model for metallicity model 'c' in Table 9. Bottom panel: the solutions maximizing our confidence for metallicity model 'l'.

density in the mid-plane of the Galaxy by main-sequence stars with masses in the range 0.08–100 $M_\odot$ is 0.059 $M_\odot$ pc^{-3}, and the minimum contribution is 0.035 $M_\odot$ pc^{-3}. Stars less massive than 1 $M_\odot$ contribute about 83 per cent of this amount. Extrapolating to zero mass, substellar objects add between 1.5×10^{-3} $M_\odot$ pc^{-3} ($\alpha_1=0.7$, $n=0.083$ star pc^{-3} $M_\odot^{-1}$) and 0.12 $M_\odot$ pc^{-3} ($\alpha_1=1.85$, $n=0.091$ star pc^{-3} $M_\odot^{-1}$).

Concerning the IMF ($\alpha_1=2.7$), we note that stars with masses between 0.08 and 0.5 $M_\odot$, the M dwarfs, constitute between 66 per cent ($\alpha_1=0.7$) and 87 per cent ($\alpha_1=1.85$) of the total number of stars formed that are more massive than 0.08 $M_\odot$. Finally, we note that our IMF with $\alpha_1=1.3$ and $n=0.087$ star pc^{-3} $M_\odot$ leads to 0.13 star pc^{-3} in the mass range 0.08–1 $M_\odot$, and 0.011 star pc^{-3} in the mass range 1–60 $M_\odot$. The Scalo IMF corrected for a Galactic disc age

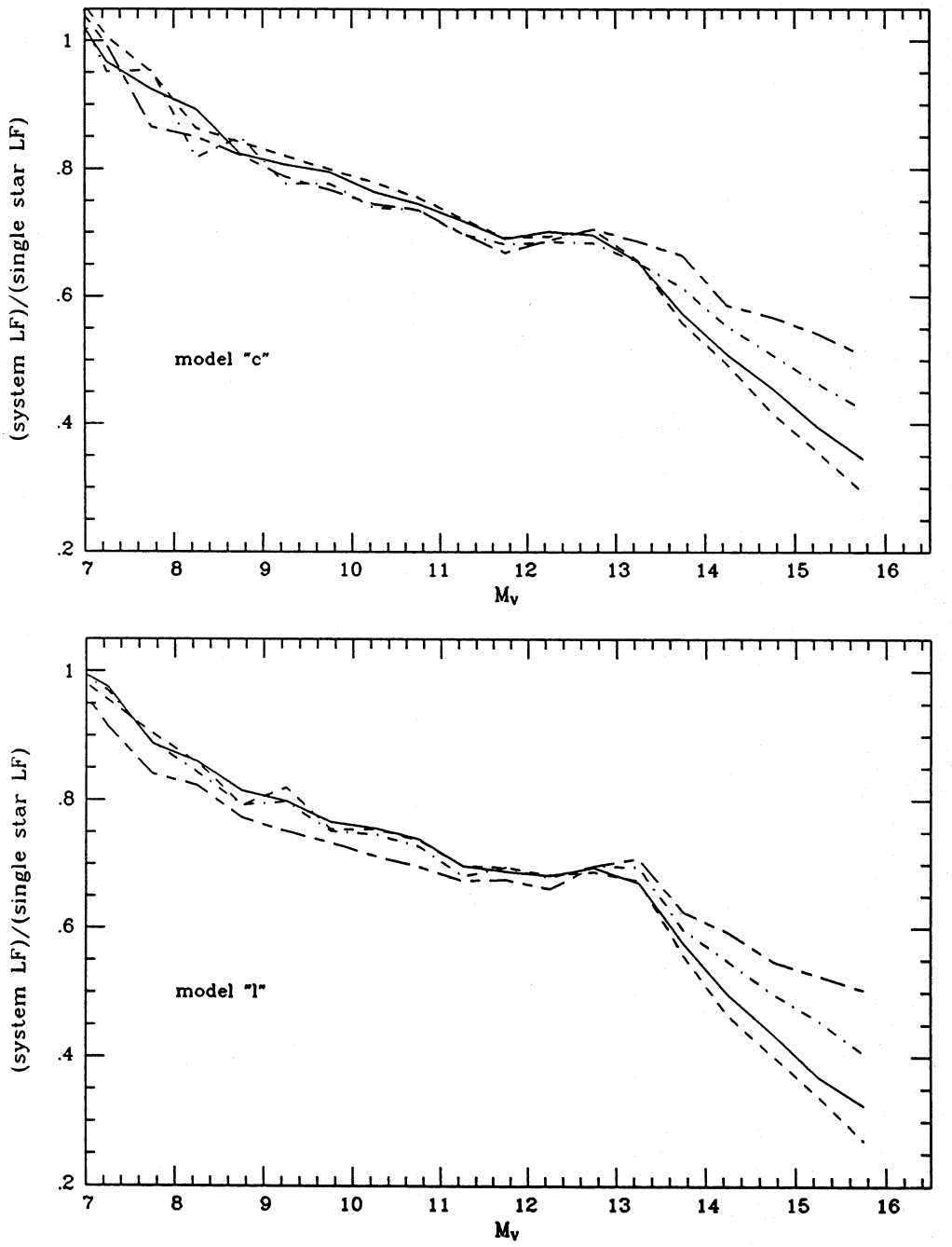

Figure 21. The ratio $\psi(M_{V,p})/\psi(M_V^*)$ (i.e. system luminosity function divided by the single-star luminosity function) is plotted as a function of absolute visual magnitude for the models shown in Fig. 20. The top panel assumes metallicity model 'c', and the lower panel model 'l'.

of $T_0 = 9$ Gyr has 0.086 and 7.7×10^{-3} star pc^{-3}, respectively. The contribution to the Oort limit by Scalo's present-day mass function is 0.031 $M_\odot$ pc^{-3} in the former mass range and 6.8×10^{-3} $M_\odot$ pc^{-3} in the latter mass range, which is comparable with our present-day mass function.

9 ALTERNATIVE MODELS

The aim of the present study is to derive a consistent model of the distribution of stars within the Galactic disc close to the Sun. Our analysis in Section 7 identifies solutions of the stellar mass function consistent with the adopted mass–M_V relation. We do not, however, claim to have scanned all of parameter space, as this would involve varying the mass–M_V relation as well as the mass function. Nevertheless, we can gain some feeling for the validity of the model we have presented by considering an alternative model which has little structure in the mass–M_V relation.

We adopt the mass–M_V relation listed in table IV of Scalo (1986) and plotted in our Fig. 1, and the mass-generating function given by

$$M(X) = \frac{0.284 X^{0.337}}{(1-X)^{0.5} - 0.015(1-X)^{0.085}}, \qquad (15)$$

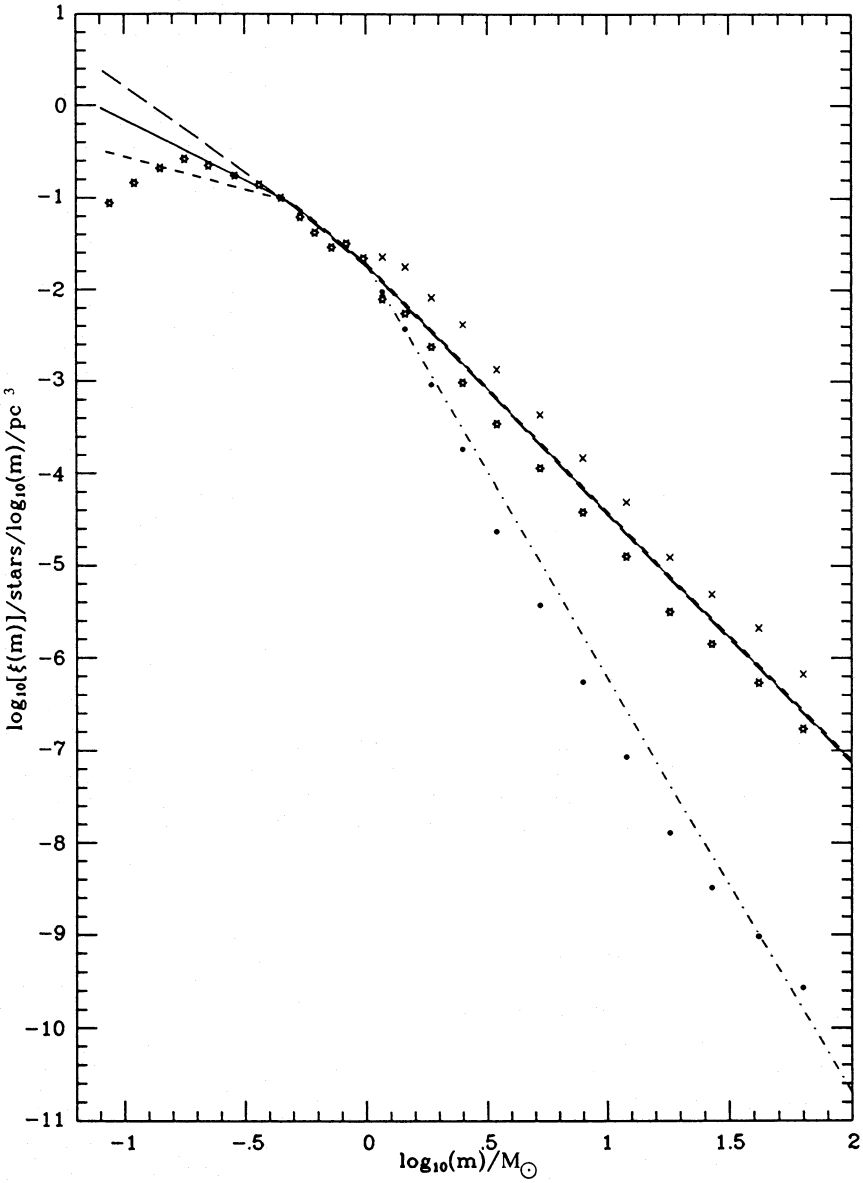

Figure 22. The stellar initial mass function (IMF) and present-day mass function (PDMF). The solid line represents the IMF given by equation (13), and the long- and short-dashed lines are for the cases $\alpha_1 = 1.85$ and 0.70, respectively. The PDMF ($\alpha_3 = 4.5$, Section 2) is indicated by the dot–dashed line. At masses below about 1 $M_\odot$ the PDMF equals the IMF. As a comparison, we show the PDMF derived by Scalo (1986) by solid dots. He corrects for stellar evolution; for a Galactic disc age of $T_0 = 9$ Gyr the IMF is indicated by stars, and for $T_0 = 12$ Gyr by crosses.

Table 10. The γ-parameters in equation (14) for some values of α_1.

α_1	γ_1	γ_2	γ_3	γ_4
1.1	0.28	1.14	0.010	0.1
1.2	0.21	1.50	0.045	0.5
1.3	0.19	1.55	0.050	0.6
1.55	0.10	1.00	0.10	2.0

which is a good representation of the mass function derived by Scalo from the then available data. We generate 1.5×10^6 systems with stellar masses in the range 0.08 to 1 $M_\odot$. We assume, conservatively, that 50 per cent of all 'stars' in the SIP sample are unresolved binaries, and adopt the colour–magnitude relation in Table 6 (model 'c') corrected for $f_{\rm trig} = 0.1$, whereby we obtain photometric parallaxes for each system from equation (6), just as described in Section 5.1.

The simulated luminosity functions, using $h = 270$ pc, are shown in Fig. 23. In Fig. 24 we show the cumulative distribution functions. Applying the KS test for both the single-star distributions (right panel) and the system distribution functions (left panel), we obtain confidence values of $P_{M_V} = 4$ per cent and $P_{V-I} = 7$ per cent, respectively. We may conclude that this model is a poorer representation of the data than those models considered above. The reason for the worse performance of this model is that it places the structure seen in the luminosity function into the mass function by adopting an essentially featureless mass–M_V

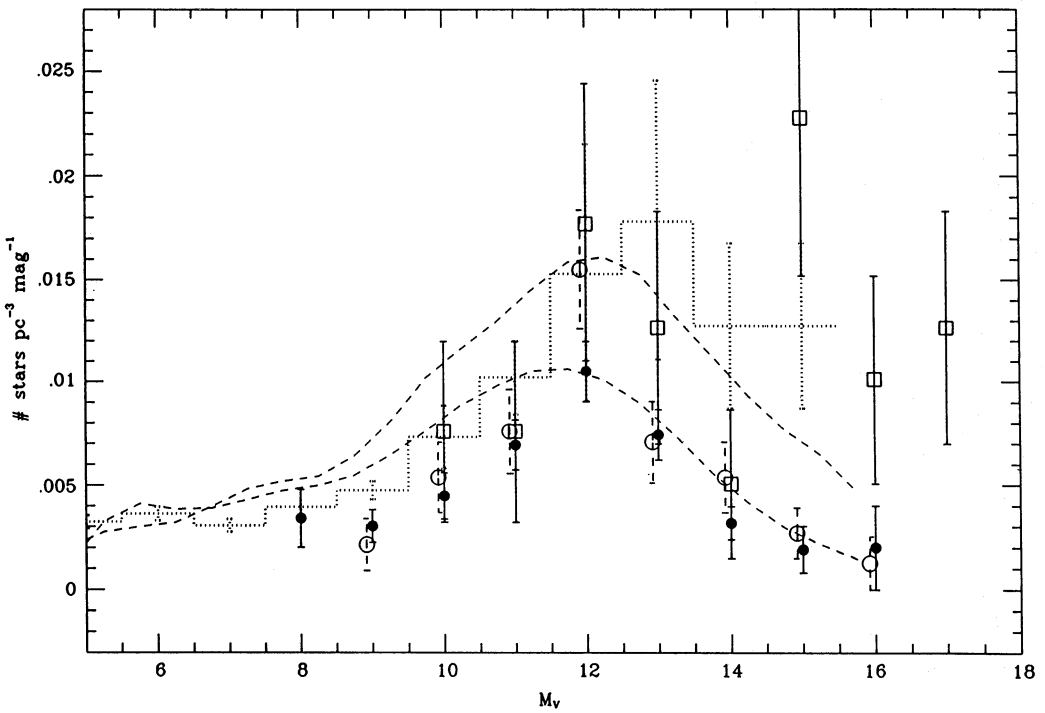

Figure 23. An alternative model. The data are as in Fig. 20. The upper curve depicts the single-star Galactic field model and the lower curve the system luminosity functions for $f=0.5$. To generate these models we have adopted the mass–M_V relation of Scalo (1986) and the mass-generating function given by equation (15). It leads to a distribution of stars by mass in good agreement with Scalo's mass function. The adopted scaleheight is $h=270$ pc, and we have used the colour–magnitude relation given in Table 6 (model 'c') corrected for $f_{\rm trig}=0.1$.

relation. This, however, is in contradiction with stellar physics (KTG1).

The analysis by Reid (1991) shows that particular models do not lead to a satisfying resolution of the discrepancy between the nearby and photographic luminosity functions. He bases his approach on an adopted luminosity function for single stars from which he chooses stars at random to generate a system luminosity function given some proportion of binaries, a fraction of which are composed of equal luminosity systems and the remainder having uncorrelated luminosities. The single-star luminosity function he assumes is based on the sample of stars within 5.2 pc and is flat for $M_V > 12$. By varying the proportion of binaries, and the fraction of these which have equal components, as well as the constant Gaussian cosmic scatter, he concludes that binaries cannot lead to the difference in shape of the luminosity functions. Reid's adopted single-star luminosity function corresponds to the case $\alpha_1 \approx 1.5$ in our analysis, for which we find solutions acceptable with confidence greater than about 20 per cent (Figs 16 and 18). Overall, our study covers a larger portion of parameter space and models cosmic scatter in much greater detail, taking into account explicitly all biases affecting the derivation of a colour–magnitude relation and stellar number densities. This latter point is particularly important, as demonstrated in Section 7. This allows us to identify solutions in acceptable agreement with the data and, while not a proof of a particular model, these do constitute an acceptable working hypothesis and show that the nearby and photographic star counts can readily be reconciled.

10 THE APPARENT DISC SCALEHEIGHT AS A FUNCTION OF ABSOLUTE MAGNITUDE

As discussed briefly in Section 7.2, we expect the apparent scaleheight, $h_{\rm app}$, to vary with $V-I$, even if the true underlying scaleheight of the Galactic disc remains constant. In Section 10.1 we discuss our simulations of $h_{\rm app}$ as a function of $V-I$, in Section 10.2 we compare the results of these with the measurements of Hawkins (1988), and in Section 10.3 we investigate Hawkins' hypothesis of a young age for the faintest stars using kinematical data of stars in the solar neighbourhood. Finally, in Section 10.4 we discuss an alternative explanation for the results of Hawkins.

10.1 Simulations

We generate $N=4\times10^6$ systems within a distance of 300 pc, exactly as in Section 7.2.2, using the colour–magnitude relation in Table 6 corrected for $f_{\rm trig}=0.1$, and we adopt $\alpha_1=1.2$ and $h=270$ pc which are in good agreement with the values in Table 9. We bin the true distance (z) distribution generated from equation (10) for all data into 10 pc wide bins, and refer to this as our true distribution. We also bin the photometric distance ($d_{\rm p}$) for 'stars' into eight $V-I$ colour bands: a [1.0, 1.4]; b [1.7, 2.0]; c [2.13, 2.45]; d [2.45, 2.7]; e [2.7, 3.07]; f [3.07, 3.45]; g [3.45, 3.82] and h [4.0, 4.5]. To each distance distribution we fit an equation of the form of equation (10), and thus deduce the apparent scaleheight $h_{\rm app}$. In Fig. 25 we compare the resulting distance distributions in three colour ranges for both metallicity models assuming

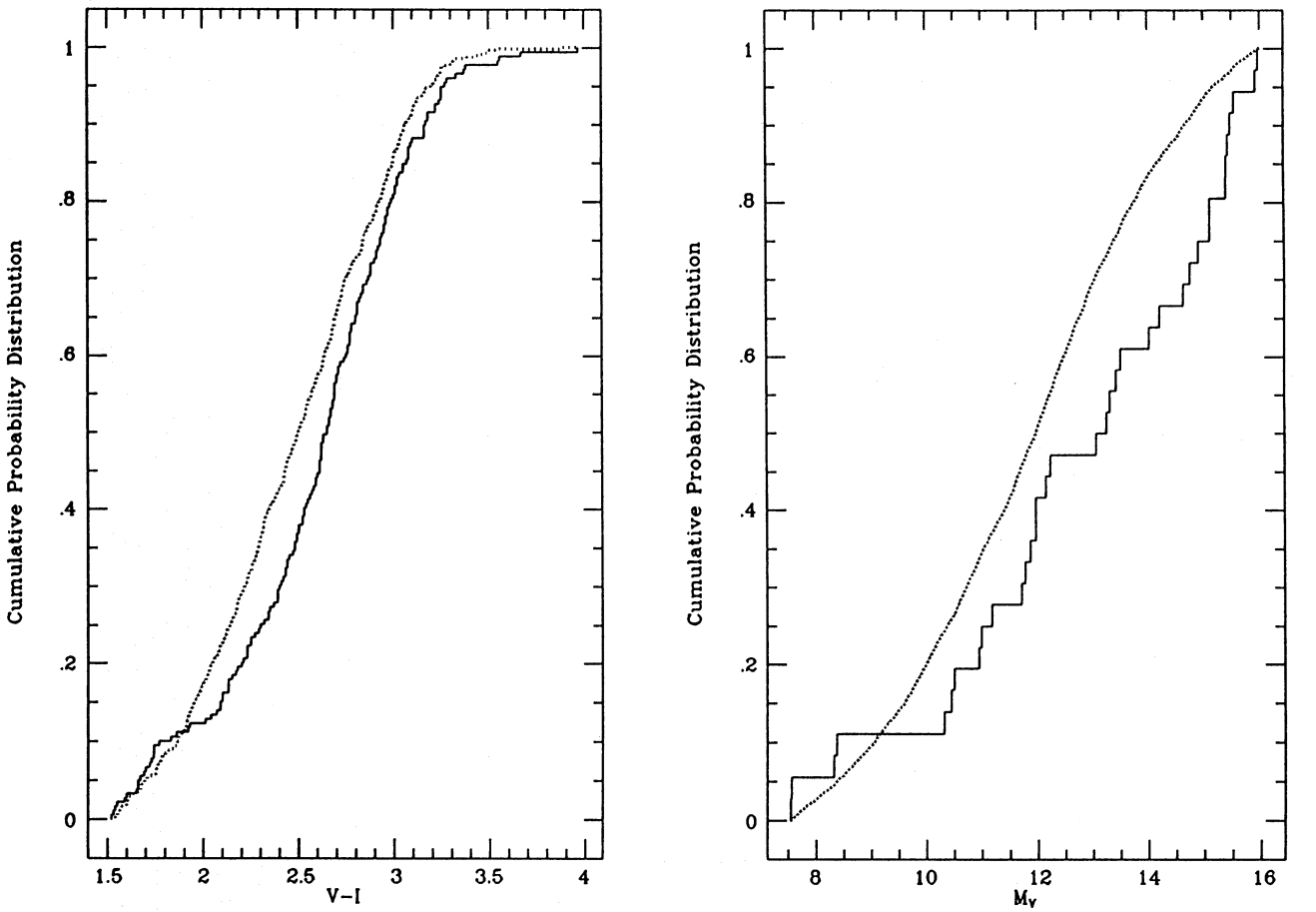

Figure 24. An alternative model. The right-hand panel shows the model cumulative distribution functions for single stars (dotted curve), where the cumulative distribution based on observed absolute magnitudes (Table B2 in Appendix B) is shown as a solid curve. The left-hand panel shows the cumulative distribution in $V-I$ colour. The model is shown as the dotted curve, whereas the SIP data yield the solid curve.

$f=1$. We note that metallicity model 'c' leads to a larger effect at the faintest magnitude bin in that incompleteness sets in at a somewhat smaller distance. The densities are largest in colour band 'd' because the peak of the luminosity function is at $V-I\approx 2.7$. The effects of binaries are most apparent in the reddest colour band, as expected. If the appropriate Malmquist corrections were applied to the raw star-count model data, then the inferred scaleheight would be $h=270$ pc in every colour band.

In Fig. 26 we plot $h_{\rm app}(V-I)$ for different values of f. We recall here our discussion in Section 4.3.3 that f_{M_V} decreases with absolute magnitude if $f<1$. The top panel assumes our metallicity model 'c', and the lower panel assumes model 'l'. The largest effect is to be seen at the reddest colours with largest f. If $f=1$ for metallicity model 'c' then, at $V-I=4.2$, $h_{\rm app}$ reaches a minimum value of 153 pc, i.e. the Galactic disc appears thinner by a factor of 1.8. The detailed behaviour of the apparent disc scaleheight with colour and the proportion of binaries is the result of the interplay of the various contributions to cosmic scatter and their variation with colour, as well as the structure of the luminosity function.

10.2 Comparison with observations

Hawkins (1988) finds a large effect beyond $M_{\rm R63F}\approx 11.5$ such that $h_{\rm app}$ decreases to ≈ 90 pc for his reddest stars. Hawkins used the RG715 filter (I_N) for his I-band plates and the RG630 filter (R_{63}) for his R-band plates to study two fields with the UK 1.2-m Schmidt Telescope, and measured $h_{\rm app}$ as a function of $M_{\rm R63}$ towards the South Galactic Pole and at Galactic latitude $b=-47°$. We transform $M_{\rm R63}$ to R_{63}-I_N colours using $M_{\rm R63}=4(R_{63}-I_N)+5$ (Hambly, private communication and fig. 2 of Hawkins 1986) and with equation (9) of Bessell (1986) to standard $R-I$ colours. Finally, we use the following relations obtained by linear regression from the data in table 2 of Bessell (1991) to transform Hawkins' measurements in the R_{63} band to our $V-I$ colours:

$$V-I=\begin{cases}1.465(R-I)+0.467 & \text{if } 0.774\le R-I\le 1.801,\\ 2.507(R-I)-1.410 & \text{if } 1.801<R-I\le 2.357.\end{cases} \quad (16)$$

We plot Hawkins' measurements in Fig. 27 and compare them with our model for $f=1$, shown as filled circles. It is apparent that our model lies in fair agreement with the measurements at $V-I<2.8$, but that it does not agree with Hawkins' data at redder colours.

Hawkins' measurements indicate a steeper dependence on absolute magnitude, which he attributes to a very young stellar population. Stars with colours in the range $3<V-I<3.5$ have $13<M_V<14.5$ and, if as young as

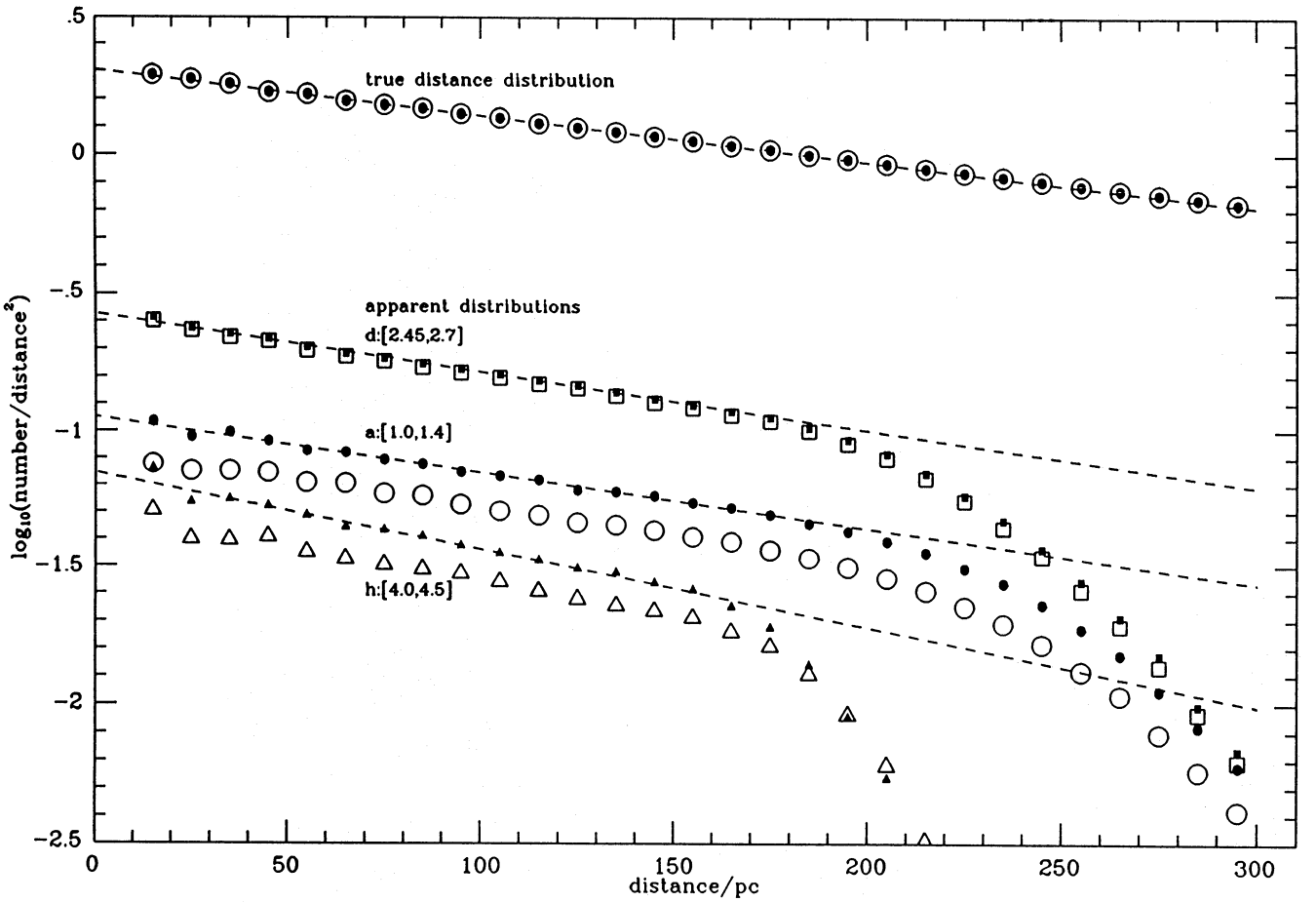

Figure 25. Simulated distance distribution assuming that 100 per cent of all 'stars' are unresolved binaries. The adopted density law is given by equation (10) with scaleheight $h_{ass}=270$ pc. The distributions assuming metallicity model 'c' are plotted using filled symbols, and those assuming model 'l' are shown by open symbols. Binning the distances z of all individual stars into 10 pc wide bins, we obtain the true distance distribution shown by the top-most distributions. Linear regression on this distribution recovers the scaleheight ($h=264\pm4$ pc), and is shown by the dashed line. Binning the apparent distances d_p for 'stars' with colours in the ranges a, d and h (Section 10.1), we obtain for each model the distributions shown. Linear regression over the distance interval $30\le d_p\le 170$ pc on these yields the following results for model 'c': $h^{(2)}_{app}=210\pm5$ pc (colour range a); $h^{(2)}_{app}=204\pm2$ pc (range d) and $h^{(2)}_{app}=153\pm4$ pc (range h). For model 'l' we obtain the following: $h^{(2)}_{app}=208\pm5$ pc (colour range a); $h^{(2)}_{app}=203\pm3$ pc (range d) and $h^{(2)}_{app}=171\pm5$ pc (range h). The linear regression lines for model 'c' are shown by dashed lines. The apparent distance distribution decays at $d_p>200$ pc because we do not generate stars at distances larger than 300 pc.

required by Hawkins, ought to show up as very young stars in other surveys (e.g. by Giampapa & Liebert 1986) and in the immediate neighbourhood of the Sun. Giampapa & Liebert found no difference in the kinematics of stars fainter than $M_V\approx12$ as compared to brighter stars, at least down to $M_V\approx17$. Within 5.2 pc, stars in the magnitude range relevant to Hawkins' observations show space motions representative of an old disc population, as we show in the next section.

10.3 Kinematic evidence and discussion

In the previous section we have shown that our model leads to a decline in the apparent disc scaleheight with absolute magnitude, but that it is not compatible with the results of Hawkins (1988). In this section we demonstrate that the interpretation that stars with $M_V>13$ are significantly younger than stars with $M_V<11$ is inconsistent with the kinematics of the stars in the vicinity of the Sun, which do not support an increasingly young age with absolute magnitude.

Giampapa & Liebert (1986) found some evidence that the stars with $M_V>17$ in their sample of LHS stars are younger than the brighter stars. However, they noted that this may simply be a selection effect in that stars that are very faint need to have a small proper motion to be detected by scanning photographic plates at two different epochs. In Table B1 (Appendix B), we list all the known stars within 5.2 pc with declination $>-20°$ and $M_V\ge7.54$. This sample contains 30 stars with $M_V\ge11.6$ and known kinematics, four of which are also contained in the sample of Giampapa & Liebert who list 24 stars. We hope that the 5.2-pc sample of stars is reasonably complete and that there are no kinematic or other biases affecting our discussion.

We convert the kinematic data of Table B1 to velocity components in Galactic coordinates, and adopt the sign convention such that $+U$ is the velocity component in the Galactic plane directed away from the Galactic centre, $+V$ is the component in the Galactic plane in the direction of Galactic rotation and $+W$ is the component perpendicular to

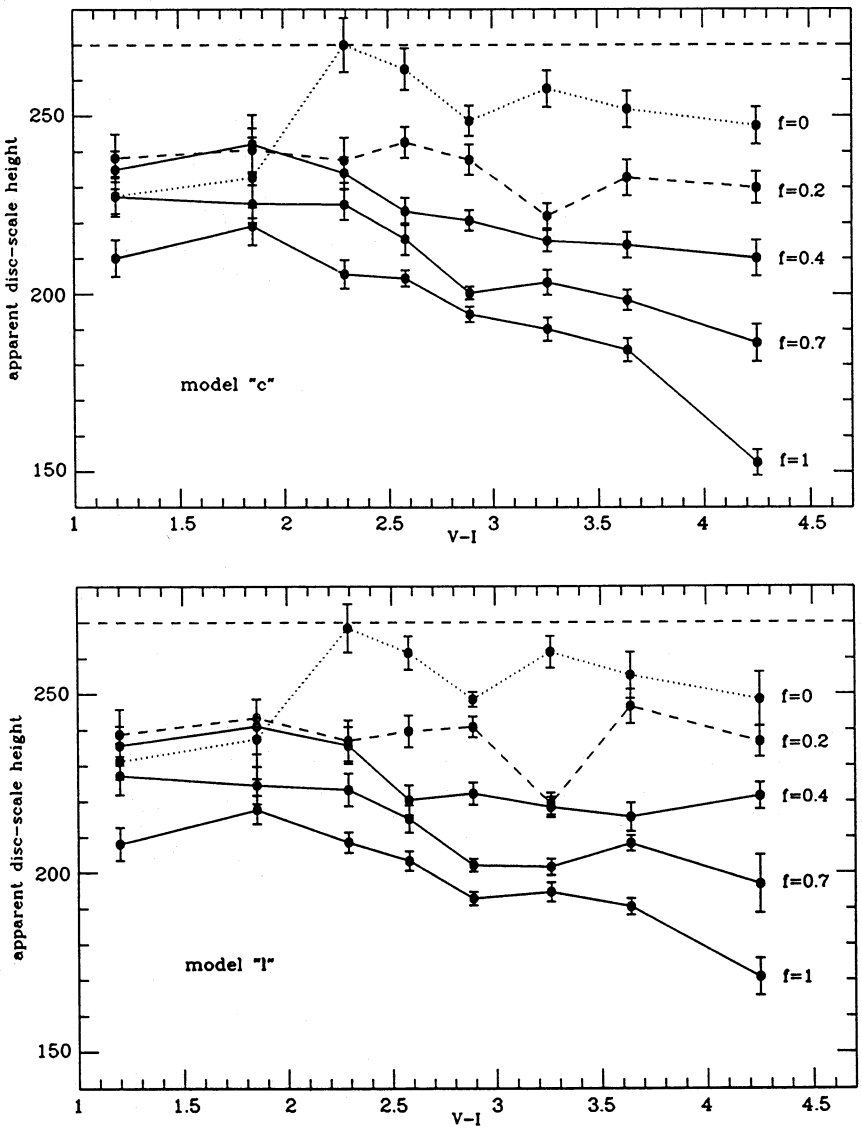

Figure 26. Apparent disc scaleheight as a function of colour for different proportions of unresolved binaries. The top panel shows the results assuming metallicity model 'c', and the lower panel assumes model 'l'. Error bars indicate the uncertainties in each colour bin, being smallest at $V-I \approx 2.7$ where the peak of the luminosity function lies. The horizontal dashed line represents our adopted disc scaleheight ($h = 270$ pc).

the Galactic plane in the direction of the NGP. In Table B3 we tabulate the U, V and W components for each star of Table B1 sorted into three magnitude ranges: $9.5 \leq M_V < 12$, $12 \leq M_V < 14.5$ and $14.5 \leq M_V$. We emphasize that we have counted every stellar component in a multiple system as a separate star. This is reasonable provided that orbital motions do not affect the space motion significantly. We plot the distribution of peculiar stellar velocities with respect to the local standard of rest (LSR), $u = U + u_\odot$ and $v = V + v_\odot$, in Fig. 28, where $(u_\odot, v_\odot, w_\odot) = (-9, 12, 7)$ km s^{-1} are the components of the peculiar velocity of the Sun relative to the LSR (Mihalas & Binney 1981). The top left panel shows the distribution for all stars in Table B3, and the other panels illustrate the distribution in each magnitude bin. There is no evidence for a significant difference between the distributions. In Table 11 we summarize the data by tabulating the mean values and velocity dispersions. The velocity dispersions are calculated by weighting each nearby star by its ω-component so that these local data can be used to represent the large volume of Hawkins' survey (equations 1–3 of Wielen 1977). The total velocity dispersion is given by $\sigma_{\rm tot} = (\sigma_u^2 + \sigma_v^2 + \sigma_w^2)^{1/2}$.

The theory of diffusion of stellar orbits with time in its simplest form (Wielen 1977) assuming a constant diffusion coefficient yields, for the behaviour of the velocity dispersion with stellar age τ,

$$\sigma_{\rm tot} = (\sigma_{\rm tot,0}^2 + C\tau)^{1/2}, \qquad (17)$$

where $\sigma_{\rm tot,0} = 10$ km s^{-1} is the velocity dispersion at birth, and $C = 6.0 \times 10^{-7}$ (km s^{-1})^2 yr^{-1} is the diffusion coefficient.

We need to compare $\sigma_{\rm tot}$ measured from the stellar sample within 5.2 pc with the velocity dispersion $\sigma_{\rm tot,exp}$ expected for a stellar sample with the scaleheight measured by Hawkins (1988). Interpolating table 2 of Wielen (1977) we obtain, for

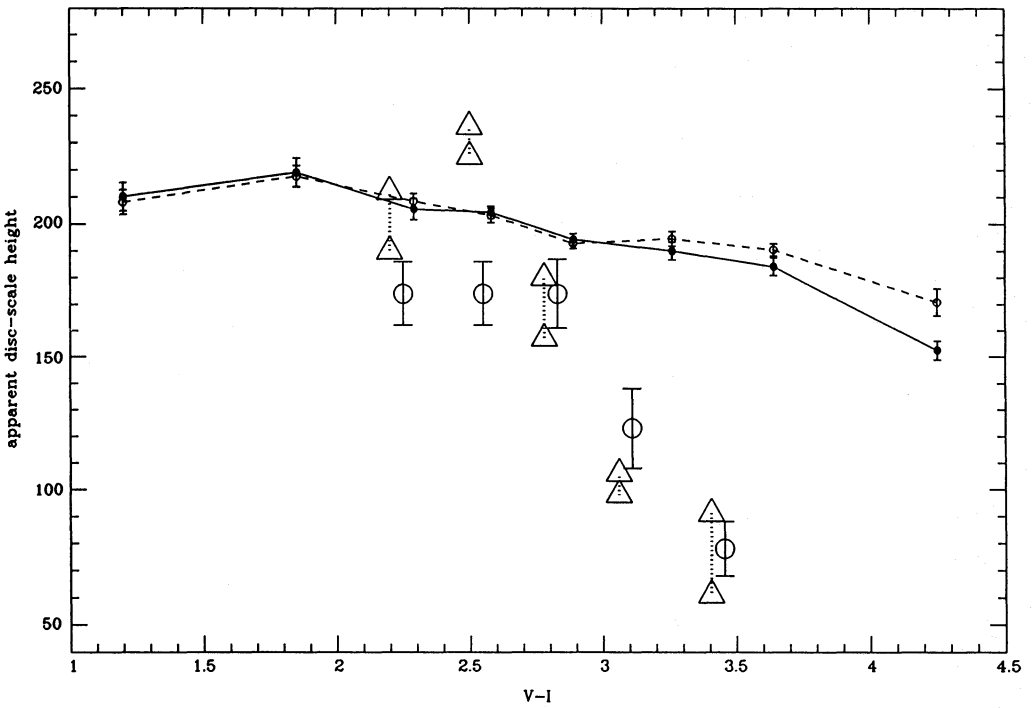

Figure 27. The triangles represent measurements of h_{app} obtained by Hawkins (1988) and transformed from his photographic R band to our $V-I$ colours in Section 10.2. For comparison, we also plot as small filled circles (metallicity model 'c') and as small open circles (model 'l') the $f=1$ simulations shown in Fig. 26. We also plot as large open circles the scaleheights we obtain in Section 10.4 from the SGP star-count data. We note the excellent agreement, especially for the two faintest bins of Hawkins, with the assumption that the decreasing apparent scaleheight is simply an artefact of a decreasing maximum sampling distance with decreasing brightness of the stars.

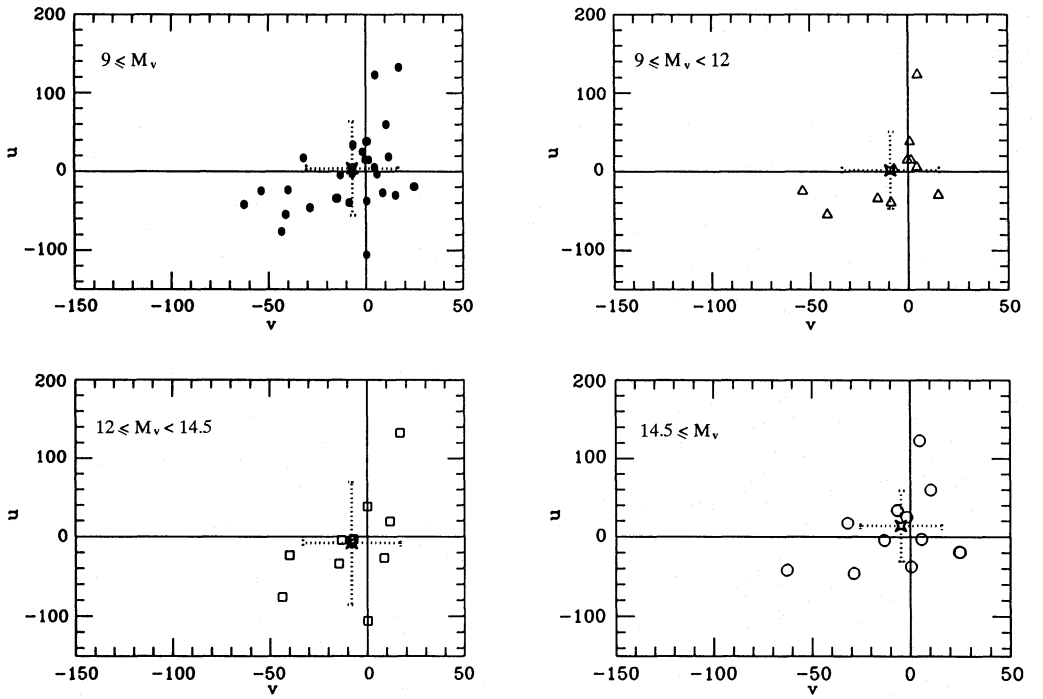

Figure 28. Velocity components in Galactic coordinates of the nearby stars (Tables B1 and B3 in Appendix B). u is negative in the direction of the Galactic Centre and v points in the direction of Galactic rotation. The upper left-hand panel shows the plot for all stars fainter than $M_V=9$, whereas the other panels show the distribution of u and v velocity components for the stars binned into three magnitude bins as indicated. The dotted error bars in all panels indicate velocity dispersions σ_u and σ_v, as defined by Wielen (1977), centred on the position of the mean values. There is no indication that the scatter of data decreases with increasing magnitude, providing no evidence for increasing youth with magnitude.

a stellar sample with $h \approx 90$ pc [the weighted average of Hawkins' faintest ($M_R = 13.5$) bin], an age $\tau \approx 6.3 \times 10^8$ yr. Equation (17) gives $\sigma_{\mathrm{tot,exp}} = 20$ km s^{-1}. We perform a χ^2 test to obtain an estimate of the confidence we can place in rejection of the hypothesis that the stars fainter than $M_V = 12$ have an age of $\approx 6 \times 10^8$ yr. The standard error in the standard deviation is $\delta\sigma = \sigma_{\mathrm{tot}}/(2N_*)^{1/2}$, where N_* is the number of stars in the sample used to evaluate σ_{tot} (Trumpler & Weaver 1953, p. 190). The test we apply is $\chi^2 = [(\sigma_{\mathrm{tot}} - \sigma_{\mathrm{tot,exp}})/\delta\sigma]^2$. For the $12 \leq M_V < 14.5$ bin and the $14.5 \leq M_V$ bin we have $\chi^2 = 12$. The probability of observing such a value or larger for χ^2, with one degree of freedom, is about 6×10^{-4}.

The hypothesis that the faint stars are young is not consistent with kinematical data. It is interesting, though, to consider the reported incidence of Hα emission (Table B3, Appendix B). A fraction of ≈ 0.3 of all stars with $0.58 \geq m > 0.29$ M$_\odot$ exhibit Hα emission, whereas a fraction of 0.5–0.6 of all stars with $0.29 \geq m > 0.14$ M$_\odot$ show Hα emission, and the fraction is 0.5–0.8 for stars with $m \leq 0.14$ M$_\odot$. However, the apparently increased incidence of chromospheric activity does not imply a decreasing age for this sample.

10.4 An alternative explanation

The decrease of the apparent scaleheight observed by Hawkins (1988) cannot be explained by a correlation between age, kinematics and stellar mass. An alternative explanation of the results obtained by Hawkins can, however, be found by noting that the sample distance limit decreases with increasing absolute magnitude. In Table 12 we tabulate the results of Hawkins and the range in photometric distance he used to derive the apparent scaleheight h_{app}. He did not constrain the number density at $d_{\mathrm{p}} = 0$ using local data.

Turning to the SGP sample of Section 7.2.1, we perform a simple experiment. In Fig. 29 we show the distance distribu-

Table 11. The mean velocities and velocity dispersions in km s^{-1} for the data presented in Table B3 (Appendix B).

M_V	$\bar{u}$	$\bar{v}$	$\bar{w}$	σ_u	σ_v	σ_w	σ_{tot}
9<	+4	−7	0	60	24	28	70
9–12	+2	−9	+3	49	25	33	64
12–14.5	−8	−8	−7	78	25	27	86
>14.5	+14	−5	+3	45	21	23	55

Table 12. Hawkins' measurements of the Galactic disc scaleheight and the distance range he used. We tabulate weighted average values for h_{app}.

M_R	h_{app} (pc)	d_{p} (pc)
9–10	203 ± 7	0–500
10–11	228 ± 11	0–500
11–12	170 ± 7	0–500
12–13	103 ± 2	0–300
13–14	90 ± 2	0–200

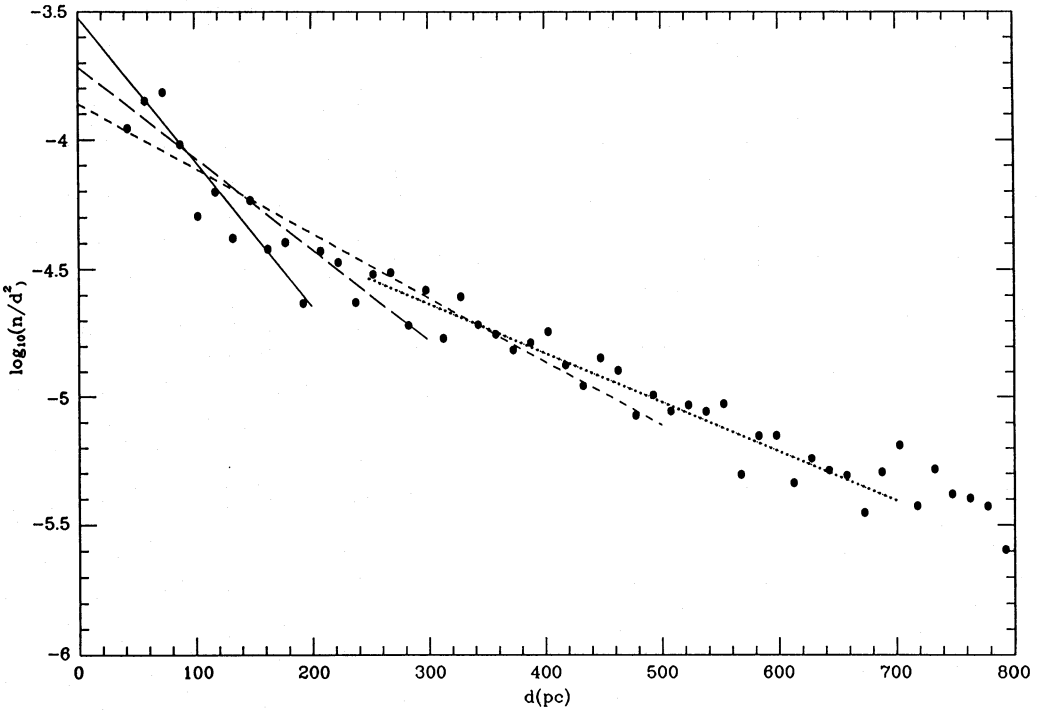

Figure 29. Alternative explanation of the results obtained by Hawkins. We show the apparent distance distribution obtained from all the stars with $V-I = 0.93$–2.0 in the South Galactic Pole sample (Section 7.2.1). Corrections for giants have not been made. Linear regression over the distance range 250–700 pc gives an apparent scaleheight of $h_{\mathrm{app}} = 225 \pm 12$ pc (dotted line). If we fit over the range 0–500 pc, however, we obtain $h_{\mathrm{app}} = 174 \pm 13$ pc, a fit over the range 0–300 pc gives $h_{\mathrm{app}} = 123 \pm 15$ pc, and a fit over the distance range 0–200 pc results in $h_{\mathrm{app}} = 78 \pm 10$ pc. The distance ranges used here are the same as those used by Hawkins. Local data give $\log_{10}(n/d_{\mathrm{p}}^2) = -3.94 \pm 0.02$ at $d_{\mathrm{p}} = 0$.

tion for 15 pc wide bins obtained from all the stars with $V-I=0.93$–2.0 in that sample. Incompleteness of this sample at distances of a few hundred parsecs becomes significant at redder colours. Linear regression over the distance range 250–700 pc gives an apparent scaleheight of $h_{\rm app}=225\pm12$ pc (dotted line). If we fit over the range 0–500 pc [without using the local ($d_{\rm p}=0$) number density] we obtain $h_{\rm app}=174\pm13$ pc, and a fit over the range 0–300 pc gives $h_{\rm app}=123\pm15$ pc, whereas linear regression over the distance range 0–200 pc results in $h_{\rm app}=78\pm10$ pc. In Fig. 27 we compare Hawkins' measurements with these results by plotting the apparent scaleheight obtained for the various distance ranges next to Hawkins' values. The similarity with our results is striking. The steepening of the density distribution away from a single exponential is evident in all magnitude bins in fig. 1 of Hawkins (1988), as well as in the data we utilize here.

Thus the simplest explanation of the result found by Hawkins (1988), that the scaleheight of low-mass stars decreases systematically for stars with $V-I>2.5$, is that Hawkins' approximation of a single exponential to represent the vertical structure of the Galactic disc is inadequate.

In Section 7.1 we have shown that the NGP star-count data, which were obtained within a photometric distance of 130 pc, are consistent with a scaleheight of $h\approx270$ pc, corresponding to an apparent scaleheight of $h_{\rm app}\approx230$ pc, for reasonable values of $f_{\rm trig}$ when compared to the number density of stars in the solar neighbourhood. A scaleheight $h\approx275$ pc ($h_{\rm app}\approx240$ pc) is also derived from the SGP star-count data (Section 7.2.1) over a distance range of 200–600 pc. However, the scaleheight derived from the SGP star-count data over a distance range more appropriate to the NGP star-count data, namely $d_{\rm p}=40$–300 pc, yields $h_{\rm app}\approx123$ pc, implying a true scaleheight smaller than 275 pc. From the solar neighbourhood data (WJK), we obtain a density $\log_{10}(n/d_{\rm p}^2)=-3.94\pm0.02$ (quoting the Poisson uncertainty) for stars in the magnitude range $6\le M_V\le9.5$ (corresponding to $0.93\le V-I\le2.0$) for a solid angle $\Omega=18.24$ deg^2 for the SGP data. If this density corresponds to a distance from the mid-plane $d_{\rm p}=0$ pc, then we obtain an apparent scaleheight $h_{\rm app}\approx180$ pc on comparison with the number density at $d_{\rm p}\approx130$ pc. This is compatible with the NGP data at the 80 per cent confidence level (Fig. 17), with $h_{\rm true}\approx230$ pc. It is interesting to note that, in the distance interval $0\le d_{\rm p}<80$ pc towards the SGP, the data are consistent with a constant stellar number density (Fig. 29).

11 CONCLUSIONS

We have resolved a long-standing controversy by showing that the discrepant shape between the stellar luminosity function observed within a distance of 5.2 pc of the Sun on the one hand, and derived from photographic surveys to much larger distances on the other hand, is a natural consequence of the different biases affecting the two different types of sample. We find that the stars within 5.2-pc distance and those counted on photographic plates within a photometric distance of 130 pc towards the NGP are distributed according to the same mass function with the same normalization in the Galactic mid-plane if the systematic effects of an age and metallicity distribution, measurement errors and, in particular, unresolved binary systems are modelled.

Unresolved binary systems affect photographic star-count data to a much larger extent than do the nearby trigonometric sample, so that the Malmquist corrections applied in the past to stars redder than $V-I\approx1.5$ have been incorrect. The changing property of cosmic scatter with colour has also never been taken into account. At $V-I\approx0.5$–1.0, stellar evolution is a major contributor, whereas at $V-I>1$ the metallicity dispersion becomes more important, while binaries dominate at $V-I>2$. Owing to the uncertainty in our knowledge of how Malmquist corrections are to be applied, we model raw star-count data. By combining all the contributions, we are able to reproduce the cosmic scatter measured from a high-quality homogeneous data set (Reid 1982), although the effects of the metallicity dispersion at colours redder than $V-I>1.5$ remain uncertain. Including Galactic disc structure in our models, we find that the overall normalization of the nearby and photographic luminosity functions can be reconciled. For an exponential disc with a scaleheight of about 270 pc, we find that a single central plane density for stars leads simultaneously to the luminosity functions within 5.2 pc and out to 130 pc if no metallicity gradient is assumed. Inclusion of an effective gradient increases the scaleheight but the uncertainties from the star-count data we use remain large.

The mass function (equation 13) can be approximated by the following function and by equation (14):

$$\xi(m)=\begin{cases}0.035m^{-1.3} & \text{if } 0.08\le m<0.5,\\ 0.019m^{-2.2} & \text{if } 0.5\le m<1.0,\\ 0.019m^{-2.7} & \text{if } 1.0\le m<\infty,\end{cases}$$

where m is the stellar mass in solar units. We are 95 per cent confident that below 0.5 $M_\odot$ the mass function power-law index lies in the range $0.70<\alpha_1<1.85$. This comprehensive range includes larger values than allowed by KTG2, because here we study in much greater depth all the effects that influence apparent stellar number densities. We find that, if the stars used to calibrate the colour–magnitude and mass–M_V relations are more metal-rich by ≈0.08 dex than are the stars at a distance of ≈100 pc from the mid-plane, then $\alpha_1=1.5$, which is also the value we obtain from the stars within a distance of 5.2 pc. Adopting the above range for α_1 and taking into account the Poisson uncertainty in the number of stars seen within 20 pc of the Sun, we find that main-sequence stars with masses between 0.08 and 100 $M_\odot$ contribute between $\rho=0.04$ and 0.06 $M_\odot$ pc^{-3} to the Oort limit, with main-sequence stars less massive than the Sun contributing about 80 per cent of this. Extrapolating the mass function to zero mass, brown dwarfs add between 1.5×10^{-3} and 0.12 $M_\odot$ pc^{-3}.

By explicitly modelling the effects of binary stars on the luminosity function at relatively bright magnitudes, we are able to probe the mass function at the smallest masses, even though the data are very sparse. In particular, this approach can be extended into the brown dwarf regime (KTG2), but the constraints set by the available data are still too poor to allow firm conclusions. As yet, the data are not good enough to quantify the binary fraction f more precisely than to say that the best results are obtained if $f\approx1$ for no effective metallicity gradient. However, $f\approx0.6$ is also consistent with the star-count data and leads naturally to the observed

decrease of f_{M_V} with increasing M_V, where f is the overall proportion of binary stars among all systems and f_{M_V} is the proportion evaluated in the magnitude interval M_V to $M_V+\Delta M_V$, and we assume that component masses are uncorrelated.

Our approach allows us to model the distribution of stars with distance from the galactic mid-plane in a way not attempted previously. We find that the apparent disc scaleheight, obtained from star-count data not corrected for Malmquist effects, is a sensitive function of the overall binary proportion among 'stars' and of the absolute magnitude of the tracer population. The behaviour of the apparent disc scaleheight with absolute magnitude is a manifestation of the variation of cosmic scatter along the main sequence, and in principle allows study of the overall properties of binary stars. The apparent scaleheight decreases with absolute magnitude. If approximately 70 per cent of all 'stars' are unresolved binaries composed of two main-sequence stars with uncorrelated masses chosen from the same mass function, then the Galactic disc appears thinner than 270 pc by a factor of about 1.4 at $V-I\approx 4.2$, and if 100 per cent of all 'stars' are unresolved binaries then the disc appears thinner by a factor of approximately 1.7 at that colour. This effect is not large enough to account for the decrease of the apparent scaleheight to 90 pc observed by Hawkins (1988) at $2.9<V-I<3.5$. The hypothesis that this indicates an age of approximately 5×10^8 yr for stars in that colour range is not consistent with kinematical data. In the immediate solar neighbourhood such stars, and for that matter much fainter ones, show every characteristic of old disc kinematics. The large decrease of the apparent disc scaleheight observed by Hawkins (1988) is a result of the inadequacy of a single exponential to describe the stellar density distribution towards the South Galactic Pole.

Summarizing, we have developed a model of the distribution of lower main-sequence stars in space and luminosity within a few hundred parsecs of the Sun that is consistent with all available constraints. These include the distribution of stars within the immediate neighbourhood of the Sun, the distribution obtained from photographic surveys in the direction of the Galactic poles, available data on binary stars, and the structure of the Galactic disc, as well as observational and theoretical mass–M_V data. Much more observational work is needed to determine which effective metallicity gradient and binary fraction are applicable before we can constrain α_1 better. The results quoted here are valid for one mass–M_V relation only. Other mass–M_V relations will be used in the near future to investigate whether consistent solutions are possible.

We have encountered the following three problems, none of which is very serious. (i) The observed cumulative $V-I$ distribution towards the NGP shows an excess in the colour range $1.5<V-I<2.0$ which we do not currently understand (Section 7.5). (ii) Our models of the system luminosity function predict stellar space densities that are too large at $M_V>13$ (Section 7.5). (iii) There appears to be a discrepancy in the scaleheights derived from the NGP and SGP star-count data in the distance range 0–300 pc (Sections 7.2.3 and 10.4).

Our model has two observational implications. First, the structure evident in the stellar luminosity function is universal and must therefore show up in *all* metal-rich stellar populations. This structure consists of a flattening of the luminosity function at $M_V\approx 7$ and a pronounced peak at $M_V\approx 12$. These features are mass function *independent* as long as the mass function is not radically different from that in the solar neighbourhood (equation 13). Equivalent structure will be present in metal-poor populations, but its amplitude and precise location depend on the low-metallicity mass–M_V relation. Secondly, the apparent Galactic disc scaleheight deduced from *raw* star-count data for stars with $M_V>6$ shows variations with absolute magnitude of the tracer 'stars' which reflect the behaviour of cosmic scatter and the structure of the luminosity function. The scaleheight decreases with increasing $V-I$ of the tracer population at a rate that increases with the proportion of binaries among 'stars'. By studying the behaviour of this apparent disc scaleheight with spectral type, we can hope to constrain the binary proportion.

ACKNOWLEDGMENTS

We thank Robert Cannon and Caroline Soubiran for useful discussions, and Neill Reid for very helpful comments. PK thanks Trinity College, Cambridge (UK), and the Nonlinear Sciences Institute of the University of California, Santa Cruz, for support, and acknowledges the facilities at the Institute of Astronomy in Cambridge where most of this work was carried out. CAT is very grateful to the UK SERC and NATO for providing a fellowship.

REFERENCES

Abt H. A., 1978, in Gehrels T., ed., Protostars and Planets. Univ. Arizona Press, Tucson, p. 323
Bessell M. S., 1986, PASP, 98, 1303
Bessell M. S., 1990, A&AS, 83, 357
Bessell M. S., 1991, AJ, 101, 662
Brosche P., 1964, Astron. Nach., 288, 33
Close L. M., Richer H. B., Crabtree D. R., 1990, AJ, 100, 1986
Combes F., 1991, ARA&A, 29, 195
Dahn C. C., Liebert J., Harrington R. S., 1986, AJ, 91, 621 (DLH)
Drukier G. A., Fahlman G. G., Richer H. B., VandenBerg D. A., 1988, AJ, 95, 1415
Duquennoy A., Mayor M., 1991, A&A, 248, 485
Eggleton P. P., 1971, MNRAS, 151, 351
Eggleton P. P., 1972, MNRAS, 156, 361
Eggleton P. P., Fitchett M. J., Tout C. A., 1989, ApJ, 347, 998
Fenkart R. P., del Rio G., 1991, A&A, 89, 217
Fisher D. A., Marcy G. W., 1992, preprint
Giampapa M. S., Liebert J., 1986, ApJ, 305, 784
Gilmore G., Wyse R. F. G., 1985, AJ, 90, 2015
Gilmore G., Wyse R. F. G., 1987, in Gilmore G., Carswell B., eds, Proc. NATO ASI, Series C, Vol. 207, The Galaxy, Reidel, Dordrecht, p. 247
Gilmore G., Reid N., Hewett P., 1985, MNRAS, 213, 257
Gliese W., 1969, Veröff. Astron. Rechen-Inst. Heidelb., No. 22, University of Heidelberg
Gliese W., 1982, Landolt–Börnstein Numerical Data and Functional Relationships in Science and Technology, Subvol. 2c. Springer-Verlag, Berlin, p. 168
Gliese W., Jahreiss H., 1979, A&AS, 38, 423
Griffin R. F., Gunn J. E., Zimmerman B. A., Griffin R. E. M., 1988, AJ, 96, 172
Halbwachs J. L., 1986, A&A, 168, 161
Halbwachs J. L., 1987, A&A, 183, 234

Hawkins M. R. S., 1986, MNRAS, 223, 845
Hawkins M. R. S., 1988, MNRAS, 234, 533
Hawkins M. R. S., Bessell M. S., 1988, MNRAS, 234, 177
Henry T. J., McCarthy D. W., 1990, ApJ, 350, 334
Kroupa P., Tout C. A., 1992, MNRAS, 259, 223
Kroupa P., Tout C. A., Gilmore G., 1990, MNRAS, 244, 76 (KTG1)
Kroupa P., Tout C. A., Gilmore G., 1991, MNRAS, 251, 293 (KTG2)
Kuijken K., Gilmore G., 1989a, MNRAS, 239, 605 (KG)
Kuijken K., Gilmore G., 1989b, MNRAS, 239, 651
Leggett S. K., Hawkins M. R. S., 1988, MNRAS, 234, 1065
Liebert J., Probst R. G., 1987, ARA&A, 25, 473
Lutz T. E., Kelker D. H., 1973, PASP, 85, 573
Mazeh T., Goldberg D., 1992, in Duquennoy A., Mayor M., eds, Binaries as Tracers of Stellar Formation. Cambridge Univ. Press, Cambridge, p. 170
Mazeh T., Goldberg D., Duquennoy A., Mayor M., 1992, ApJ, 401, 265
Mihalas D., Binney J., 1981, Galactic Astronomy. Freeman & Co., San Francisco
Monet D. G., Dahn G. C., Vrba F. J., Harris M. C., Pier J. R., Luginbuhl C. B., Ables H. D., 1992, AJ, 103, 638
Popper D. M., ARA&A, 18, 115
Press W. H., Flannery B. P., Teukolsky S. A., Vetterling W. J., 1986, Numerical Recipes. Cambridge Univ. Press, Cambridge
Reid N., 1982, MNRAS, 201, 51
Reid N., 1991, AJ, 102, 1428
Reid N., Gilmore G., 1982, MNRAS, 201, 73
Salpeter E. E., 1955, ApJ, 121, 161
Scalo J. M., 1986, Fundam. Cosmic Phys., 11, 1
Stobie R. S., Ishida K., 1987, AJ, 93, 624
Stobie R. S., Ishida K., Peacock J. A., 1989, MNRAS, 238, 709 (SIP)
Tokovinin A. A., 1992, A&A, 256, 121
Tout C. A., 1991, MNRAS, 250, 701
Trumpler R. J., Weaver H. F., 1953, Statistical Astronomy. Dover, New York
VandenBerg D. A., 1985, ApJS, 58, 711
VandenBerg D. A., Bell R. A., 1985, ApJS, 58, 561
van der Kruit P. C., 1989, in Buser R., King I., eds, Saas-Fee Adv. Course No. 19, The Milky Way as a Galaxy. Geneva Observatory, p. 331
Wielen R., 1977, A&A, 60, 263
Wielen R., Jahreiss H., Krüger R., 1983, in Davis Philip A. G., Upgren A. R., eds, Proc. IAU Colloq. 76, The Nearby Stars and Stellar Luminosity Function. Davis Press, Schenectady, New York, p. 163 (WJK)
Yamagata T., Yoshii Y., 1992, AJ, 103, 117

APPENDIX A: THE MASS–LUMINOSITY RELATION

M_V	mass/$M_\odot$	M_V	mass/$M_\odot$	M_V	mass/$M_\odot$
18.00	0.0700	8.77	0.595	4.09	1.119
16.96	0.0854	8.56	0.610	4.02	1.135
16.13	0.101	8.35	0.626	3.95	1.150
15.45	0.116	8.14	0.641	3.88	1.166
14.87	0.132	7.92	0.656	3.82	1.181
14.36	0.147	7.71	0.672	3.75	1.196
13.93	0.163	7.51	0.687	3.69	1.212
13.54	0.178	7.31	0.703	3.63	1.227
13.21	0.193	7.11	0.718	3.57	1.243
12.92	0.209	6.93	0.734	3.51	1.258
12.67	0.224	6.75	0.749	3.46	1.274
12.47	0.240	6.59	0.764	3.40	1.289
12.29	0.255	6.43	0.780	3.35	1.304
12.13	0.271	6.28	0.795	3.30	1.320
11.99	0.286	6.14	0.811	3.25	1.335
11.86	0.301	6.01	0.826	3.20	1.351
11.73	0.317	5.88	0.842	3.15	1.366
11.60	0.332	5.75	0.857	3.10	1.382
11.47	0.348	5.63	0.872	3.05	1.397
11.34	0.363	5.52	0.888	3.01	1.412
11.21	0.379	5.40	0.903	2.96	1.428
11.08	0.394	5.29	0.919	2.92	1.443
10.93	0.409	5.19	0.934	2.87	1.459
10.79	0.425	5.08	0.950	2.83	1.474
10.64	0.440	4.98	0.965	2.79	1.490
10.48	0.456	4.88	0.980	2.75	1.505
10.31	0.471	4.78	0.996	2.71	1.521
10.14	0.487	4.68	1.011	2.67	1.536
9.96	0.502	4.58	1.027	2.63	1.551
9.78	0.517	4.49	1.042	2.59	1.567
9.59	0.533	4.41	1.058	2.56	1.582
9.39	0.548	4.32	1.073	2.52	1.598
9.19	0.564	4.24	1.088	2.00	1.862
8.99	0.579	4.17	1.104	-3.00	12.020

Note: Three significant figures are provided because the derivative of this relation is important and not because any particular value is so significant. The Mass–M_V relation from Scalo (1986) is adopted for $M_V < 2.52$.

APPENDIX B: THE STARS WITHIN 5.2-pc DISTANCE WITH $\delta > -20°$ AND $M_V \geq 7.5$

Table B1: Kinematical and photometric data.

Gl/GJ	#[B]	#[A]	RA	DEC	π	μ	θ	V_R	M_V
699	3	1	17.923	+4.55	.545	10.31	356	−111	13.24
406	4	2[1]	10.902	+7.32	.421	4.70	235	+13	16.57
411	5	3	11.010	+36.30	.397	4.81	187	−84	10.49
65A	6	4[1]	1.607	−18.22	.387	3.36	80	+29	15.43
65B	6	5[1]	1.607	−18.22	.387	3.36	80	+32	15.93
905	9	6	23.657	+43.92	.316	1.62	177	−78	14.75
447	11	7[1r]	11.752	+1.10	.301	1.35	152	−13	13.50
820A	12[1]	—	21.079	+38.50	.294	5.22	52	−64	7.56
820B	12[1]	—	21.079	+38.50	.294	5.22	52	−64	8.37
15A	14	8	0.258	+43.73	.290	2.91	82	+12	10.44
15B	14	9	0.258	+43.73	.290	2.91	82	+11	13.42
866A	15	10[3]	22.595	−15.60	.294	3.25	47	−60	14.6
866B	15	10[3]	22.595	−15.60	.294	3.25	47	−60	15.4
725A	17	11	18.703	+59.55	.286	2.27	323	−0.8	11.17
725B	17	12	18.703	+59.55	.286	2.27	323	+1.2	11.96
1111	19	13	8.449	+26.95	.276	1.29	242	−5	17.01
273	21	14	7.412	+5.38	.264	3.76	171	+18	11.96
54.1	22	15	1.165	−17.27	.267	1.35	62	+28	14.20
860A	25	16	22.437	+57.45	.252	0.94	245	−33	11.86
860B	25	17	22.437	+57.45	.252	0.94	246	−32	13.3
628	26	18	16.459	−12.53	.245	1.18	183	−13	12.14
234A	27	19	6.447	−2.77	.242	1.00	135	+17	13.05
234B	27	20	6.447	−2.77	.246	1.00	135	+17	16.55
473A	29	21[1r]	12.515	+9.30	.232	1.81	277	−5	14.9
473B	29	22[1r]	12.515	+9.30	.232	1.81	277	−5	15.1
83.1	31	23	1.959	+12.83	.224	2.10	148	−31	14.01
380	32[1]	—	10.139	+49.70	.222	1.45	250	−26	8.32
(L292)	—	24	10.761	−11.05	.221	1.64	159	−7	17.28
1002	34	25	0.070	−7.80	.213	2.04	204	−42	15.39
687	37	26	17.612	+68.38	.213	1.30	195	−23	10.94
1245A	38	27	19.871	+44.30	.212	0.73	143	—	15.1
1245A	38	28	19.871	+44.30	.211	0.73	143	—	16.1
1245B	38	29	19.871	+44.29	.212	0.73	143	—	15.54
876	39	30	22.843	−14.52	.211	1.14	124	−1.5	11.77
166C	40	31	4.218	−7.73	.207	4.07	212	−46	12.81
388	41	32	10.282	+20.12	.204	0.51	264	+12	10.98
702B	43[1]	—	18.049	+2.52	.203	1.12	167	−7	7.54
873	44	33	22.745	+44.08	.197	0.90	239	−0.5	11.7
445	46	34	11.743	+78.97	.192	0.86	56	−112	12.22
1116A	47	35	8.923	+19.95	.191	0.87	268	−34	15.47
1116B	47	36	8.923	+19.95	.191	0.87	268	−34	16.33
412A	—	37[2]	11.050	+43.78	.186	4.53	282	+65	10.31
412B	—	38[2]	11.051	+43.78	.186	4.53	282	+65	15.97

Notes to Table B1.

The sample of stars presented here is, as far as we know, complete. It is based on the compilation by DLH, and most of the kinematical data have been taken from the CNS3 (Catalogue of Nearby Stars, in preparation) kindly provided by H. Jahreiss prior to publication.

[1]Source is Gliese (1982); [1r] radial velocity is from Gliese (1982).

[2]Gl 412: positional and kinematic data are from Gliese (1969). The parallax given by Gliese (1969) places this star further than 5.2 pc, but DLH include it in their list using USNO and Yale parallax data.

[3]L789−6 (Gl 866): discovered to be double by Henry & McCarthy (1990). The absolute magnitudes quoted here are derived in Section 4.2.

#[A]: the number quoted by DLH; #[B]: the number quoted by Gliese (1982); RA and DEC: equatorial coordinates in hours and degrees (1950), respectively; π: trigonometric parallax; μ: proper motion in arcsec yr^{-1}; θ: position angle of the proper motion in degrees; V_R: radial velocity in km s^{-1}; M_V from DLH.

Table B2. The stars used to construct the observational cumulative distribution function in order of increasing M_V.

#[A]	M_V	name	#[A]	M_V	name
(43)	7.54	70 Oph B[2]	23	14.01	L1159−16
(12)	7.56	61 Cyg A[2]	15	14.20	L725−32
(32)	8.32	BD+50°1725[2]	10	14.63	L789−6A
(12)	8.37	61 Cyg B[2]	6	14.75	Ross 248
37	10.31	BD +44°2051A	21	14.9	Wolf 424A
8	10.44	BD +43°44A	22	15.1	Wolf 424B
3	10.49	BD +36°2147	27	15.1	G208−44A
26	10.94	BD +68°946	25	15.39	G158−27
32	10.98	BD +20°2465	10	15.4	L789−6B
11	11.17	BD +59°1915A	4	15.43	L726−8A
33	11.7	BD +43°4305	35	15.47	G9 − 38A
30	11.77	BD −15°6290	29	15.54	G208−45
16	11.86	Kruger 60A	5	15.93	L726−8B
12	11.96	BD +59°1915A	38	15.97	BD +44°2051B
14	11.96	BD +5°1668A	28	>16.1	G208−44B
18	12.14	BD −12°4253	36	16.33	G9−38B
34	12.22	AC +79°3888	20	16.55	Ross 614B
19	13.05	Ross 614A	2	16.57	Wolf 359
1	13.24	Barnard's star	13	17.01	G51 − 15
17	13.3	Kruger 60B	24	17.28	LP 731 − 58
9	13.42	BD +43°44B			
7	13.50	Ross 128			

Notes to Table B2.
#[A]: numbers in brackets are the numbers (#[B] in Table B1) given by Gliese (1982);
[2]Source is Gliese (1982).
40 Eri C (M_V = 12.81, #[A] = 31) is not included as it is a member of a triple system with a white dwarf component.

Table B3. The U, V and W velocity components of the stars listed in Table B1, binned in three magnitude bins.

#[A]	M_V	Hα	U	V	W
$9 \le M_V < 12$ ($0.58\,M_\odot \ge m > 0.29\,M_\odot$):					
3	10.49	e_J	−46	−53	−74
8p	10.44		+48	−11	−4
11p	11.17		+24	−12	+26
12s	11.96		+24	−11	+27
14	11.96		−16	−66	−17
16p	11.86		−25	−28	+2
26	10.94		−31	−21	−3
30	11.77		+13	−19	−12
32	10.98	e	+15	−8	+3
33	11.7	e	−21	+3	−1
37p	10.31		+132	−7	+8
$12 \le M_V < 14.5$ ($0.29\,M_\odot \ge m > 0.14\,M_\odot$):					
1	13.24		+142	+5	+18
7	13.50		−18	−3	−17
9s	13.42	e	+47	−12	−3
15	14.20	e	+28	−0	−24
17s	13.3	e	−25	−27	+2
18p	12.14		+6	−19	−17
19p	13.05	e?	+5	−25	+4
23	14.01	e	−15	−52	+5
31	12.81	e	−97	−12	−36
34	12.22		−67	−56	−73
$14.5 \le M_V$ ($0.14\,M_\odot \ge m$):					
2	16.57	e	+26	−44	−19
4p	15.43	e	+43	−19	−20
5s	15.93	e	+43	−19	−22
6	14.75	e	−33	−75	+0
10p	14.6	e	+69	−2	+40
10s	15.4	e	+69	−2	+40
13	17.01	e_{GL}	+6	−6	−21
20s	16.55	e?	+5	−25	+74
21p	14.9	e?	+34	−14	−6
22s	15.1	e?	+34	−14	−6
24	17.28	e_{GL}	−29	−12	−19
25	15.39		−37	−41	+28
27p	15.1	e?	—	—	—
27s	16.1	e?	—	—	—
27t	15.54	e?	—	—	—
35p	15.47		−10	+13	−37
36s	16.33		−10	+13	−37
38s	15.97	e_B	+132	−7	+8

Notes to Table B3.
U, V and W are in km s^{-1}; U is negative in the direction of the Galactic Centre.
e: Hα emission according to Gliese (1982); e_{GL}: Hα emission according to Giampapa & Liebert (1986); e_B: Hα emission according to Bessell (1991); e_J: Hα emission according to the CNS3 (Jahreiss, private communication). e? signifies uncertainty as to which component of the binary shows the emission. p: primary; s: secondary; t: tertiary star in a system (Table B4).

Table B4. The stars in Table B1 listed according to system membership. Systems with components brighter than $M_V = 7.5$ are excluded.

system #	#A			other	$M_{V,tot}$
1	1			UC	13.24
2	2				16.57
3	3			UC	10.49
4	4	5			14.90
5	6				14.75
6	7				13.50
7	(12)	(12)		UC	7.14
8	8	9		SB	10.37
9	10	10			14.20
10	11	12			10.74
11	13				17.01
12	14			UC	11.96
13	15				14.20
14	16	17			11.60
15	18			SB	12.14
16	19	20			13.01
17	21	22			14.24
18	23				14.01
19	(32)				8.32
20	24				17.28
21	25				15.39
22	26			UC	10.94
23	27	28	29		14.31
24	30				11.77
25	32			UC	10.98
26	33			UC	11.70
27	34				12.22
28	35	36			15.06
29	37	38			10.30

Notes to Table B4.
The data presented here are based on table 7 of Gliese (1982).
#A: numbers in brackets are the numbers (#B in Table B1) given by Gliese (1982).
SB: spectroscopic companion; UC: unseen companion.
40 Eri C (#A = 31) and 70 Oph B (#B = 43) are not included as they have companions brighter than $M_V = 7.5$. $M_{V,tot}$ is the combined absolute visual magnitude of the system.
Counting only the confirmed components (including the SBs), we have $(1+f_m)N = 43$ stars in $N = 29$ systems, so that the multiplicity proportion among 'stars' (i.e. systems which are likely to be unresolved in photographic surveys) is $f_m = 0.48$. Counting all confirmed as well as suspected companions, we obtain $(1+f_m)N = 50$, which gives $f_m = 0.72$ for $N = 29$ systems. We note that f_m is a measure of the number of stars in systems, and is approximately equal to f which we use throughout the main text and which assumes that all multiple systems are binaries.

APPENDIX C: DISTANCE GENERATING FUNCTION

We need to generate a random distance z, which lies within a cone of solid angle Ω and with a maximum distance z_{max} such that the resulting density of points follows equation (10). We adopt the following procedure by decomposing equation (10) into independent parts: let A be a point in the Galactic mid-plane and B a point at distance r_1 from the mid-plane such that the line AB connecting points A and B is perpendicular to the mid-plane. We generate a distance r_1 along AB such that $0 \le r_1 \le z_{max}$ and then a distance r_2 along a direction perpendicular to AB such that $0 \le r_2 \le \theta r_1$, where $\Omega = \pi\theta^2$. These combine to yield $z = \sqrt{r_1^2 + r_2^2}$.

For the distance r_1 we have, assuming that the number density along a perpendicular to the Galactic mid-plane falls off as an exponential with scaleheight h, $dX/dr_1 \propto \exp(-r_1/h)$, from which we obtain, on integration and appropriate normalization,

$$r_1(X) = -h \ln\{1 - X[1 - \exp(-z_{max}/h)]\}, \qquad \text{(C1)}$$

where X is distributed uniformly between 0 and 1.

For r_2 we have $dY/dr_2 \propto 2\pi r_2$, which is the number of points in an annulus of thickness dr_1 centred on the line AB. We obtain

$$r_2(Y) = Y^{1/2}\theta z_{max}, \qquad \text{(C2)}$$

where Y is distributed uniformly between 0 and 1.

We proceed by choosing X and independently Y, and from equations (C1) and (C2) we obtain $r_1(X)$ and $r_2(Y)$, respectively. If $0 \le r_2(Y) \le \theta r_1(X)$ then we accept $z = \sqrt{r_1^2 + r_2^2}$ as our distance, otherwise we choose new X and Y.